Search for Standard Model Higgs Boson in $H \to WW^* \to l\nu l\nu$ Decay Mode with ATLAS Detector at $\sqrt{s} = 7$ TeV

Haifeng Li

A dissertation submitted to the faculty of
Shandong University
in partial fulfillment of the requirements for the degree of

Doctor of Philosophy

Zuo-Tang Liang, Sau Lan Wu, Supervisor

School of Physics

Shandong University

04 2012

ABSTRACT

Search for Standard Model Higgs Boson in $H \rightarrow WW^* \rightarrow l\nu l\nu$
Decay Mode with ATLAS Detector at $\sqrt{s} = 7$ TeV

Haifeng Li
School of Physics
Doctor of Philosophy

Standard Model is already very successful to explain many experimental results in High Energy Physics (HEP). One of the missing parts of Standard Model is the origin of particle mass. Higgs mechanism was proposed to explain the particle mass and predicts another boson called Higgs boson. So finding Higgs boson is a way to prove the Higgs mechanism. If Higgs boson exists, the origin of mass in Standard Model can be understood. That is one of the main motivations to build Large Hadron Collider at CERN.

A search for the Standard Model Higgs boson decaying into two W bosons with di-lepton final states is performed using proton-proton collision data at center-of-mass energy of 7 TeV at the Large Hadron Collider. The data is collected by ATLAS detector during 2011 and corresponding to an integrated luminosity $4.7\,\text{fb}^{-1}$. The transverse mass of WW system is used to discriminate signal and background. No significant excess is observed with current data. A Standard Model Higgs boson with a mass in the range between 133 GeV and 258 GeV is excluded at 95% confidence level. The expected exclusion range is from 127 GeV to 233 GeV.

Keywords: LHC, ATLAS, Higgs, WW

ACKNOWLEDGMENTS

I would like to thank my supervisors Prof. Zuo-Tang Liang and Prof. Sau Lan Wu for their constant support on my work and thesis writing. Without their selfless support and help, I could not enter particle physics and finish my thesis in Higgs boson search.

I would also thank Prof. Qu-Bing Xie, Prof. Zong-Guo Si and Prof. Shi-Yuan Li for their encouragement and help on my particle physics phenomenology work in Shandong University.

Dr. Ximo Poveda has been working with me on inclusive jet cross section measurement and W+jets estimation in $H \rightarrow WW^{(*)} \rightarrow \ell\nu\ell\nu$. I have learned a lot from him both in physics analysis and how to cooperate with other people in big collaboration. I would also thank Dr. Lianliang Ma and Dr. Lashkar Kashif for their advice and help in $H \rightarrow WW^{(*)} \rightarrow \ell\nu\ell\nu$ analysis. Thanks also go to Luis R. Flores Castillo, Bill Quayle, Yaquan Fang, Tapas Sarangi, Haichen Wang, G. Carrillo Montoya, Haoshuang Ji, Neng Xu, Wen Guan in Wisconsin ATLAS group.

I would like to thank my parents Jin-Hua Li and Hong-Lan Wang for their support on everything.

I would also thank my wife Yong Liu for her love and support in my life.

Contents

List of Tables

List of Figures

Chapter 1

The Standard Model and the Higgs Mechanism

This chapter provides theoretical background and motivation for this thesis. It will give a brief introduction to Standard Model and Higgs Mechanism based on Ref. [18, 19, 5, 6]. The Higgs production and decay in hadron collider will be mentioned at Section 1.3.1 and Section 1.3.2. A short introduction to phenomenology at pp collisions is given at Section 1.3.3.

1.1 The Standard Model of Particle Physics

The Standard Model (SM) is a theoretical framework to formulate the current understanding of basic constituents of matter and their interactions. It is a gauge theory based on symmetry group $SU(3)_C \times SU(2)_L \times U(1)_Y$, which describes strong, weak and electromagnetic interactions. Those interaction are propagated by spin-1 gauge bosons : eight gluons for strong interaction, W, Z bosons for weak interaction and photon for electromagnetic interaction. Fig. 1.1 shows the elementary particles in Standard Model.

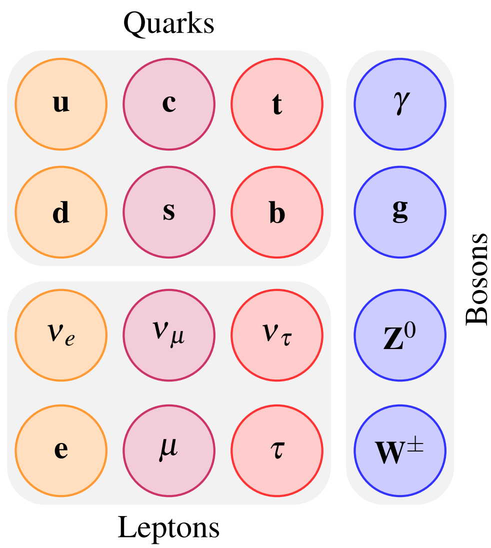

Figure 1.1 The elementary particles of Standard Model.

1.1.1 Lagrangian and Field Theory

The principle of least action states that the evolution of a physical system between two states is determined by requiring the action to be minimal. The action in a quantum filed theory is given as a functional S :

$$S = \int \mathscr{L}\, d^4x = \int \mathscr{L}(\phi, \partial_\mu \phi)\, d^4x, \tag{1.1}$$

where $\mathscr{L}$ is the Lagrangian density, ϕ is a generic field variable. The principle of least action leads to Euler-Lagrange equation :

$$\partial_\mu \left(\frac{\partial \mathscr{L}}{\partial(\partial_\mu \phi)}\right) - \frac{\partial \mathscr{L}}{\partial \phi} = 0 \tag{1.2}$$

which determines the dynamics of a physical system.

1.1.2 Quantum Electrodynamics

The Quantum Electrodynamics (QED), is used to describe electromagnetic interaction. QED is based on $U(1)$ symmetry group. The Lagrangian $\mathscr{L}$ of a free relativistic spin 1/2 particle with mass m is given by :

$$\mathscr{L}_0 = \bar{\psi}(i\gamma^\mu \partial_\mu - m)\psi. \tag{1.3}$$

$\mathscr{L}$ is invariant under global gauge transformations

$$\psi(x) \xrightarrow{\text{U(1)}} \psi'(x) \equiv \exp\{i\alpha\}\, \psi(x)\,, \tag{1.4}$$
$$\mathscr{L}' = \mathscr{L}$$

where α is an arbitrary constant phase. After the transformation, the Lagrangian does not change.

The global gauge transformation also can be extended to local gauge transformation. Under local gauge transformation, the phase $\alpha(x)$ will depend on the space-time coordinates :

$$\partial_\mu \psi(x) \xrightarrow{\text{U(1)}} \exp\{i\alpha(x)\}(\partial_\mu + i\partial_\mu \alpha(x))\, \psi(x)\,, \tag{1.5}$$
$$\mathscr{L}' \neq \mathscr{L}$$

The Lagrangian is no longer invariant under local gauge transformation unless one can add an additional term to cancel the second term of Eq. 1.5. A new spin 1 field $A_\mu(x)$ which transforms like

$$A_\mu(x) \xrightarrow{\text{U(1)}} A'_\mu(x) \equiv A_\mu(x) - \frac{1}{e}\partial_\mu \alpha(x), \tag{1.6}$$

and the new covariant derivative

$$\partial_\mu \rightarrow D_\mu = \partial_\mu - ieA_\mu. \tag{1.7}$$

The transformation will be

$$D_\mu \psi(x) \xrightarrow{\text{U(1)}} (D_\mu \psi)'(x) \equiv \exp\{i\alpha(x)\}D_\mu\, \psi(x). \tag{1.8}$$

The invariant Lagrangian under local gauge transformations is

$$\mathscr{L} = \bar{\psi}(i\gamma^{\mu}D_{\mu} - m)\psi = \mathscr{L}_0 + e\bar{\psi}\gamma^{\mu}\psi A_{\mu} = \mathscr{L}_0 + \mathscr{L}_{int}. \tag{1.9}$$

Term $\mathscr{L}_{int}$ can describe the interaction between field A_{μ} and Dirac spinor (spin 1/2 particle). To make vector field A_{μ} be a dynamical field, a kinetic term can be added to the Lagrangian

$$\mathscr{L}_{kinetic} = -\frac{1}{4}F_{\mu\nu}F^{\mu\nu} \tag{1.10}$$

where $F_{\mu\nu} \equiv \partial_{\mu}A_{\nu} - \partial_{\nu}A_{\mu}$. A mass term, like $\mathscr{L}_m = \frac{1}{2}m^2A^{\mu}A_{\mu}$, is forbidden by the gauge invariance. This Lagrangian cannot describe massive bosons without violating local gauge invariance.

1.1.3 Quantum Chromodynamics

Quarks and Color

Experiments observe lots of *baryons* and *mesons*, which indicate there are deeper level elementary constituents of matter : *quarks*. $q\bar{q}$ can represent mesons and qqq can represent baryons. One runs into trouble with the uuu configuration of doubly charged Δ^{++}. In order not to violate the Fermi-Dirac statistics, quarks must have another quantum number, which is called *color*.

The color quantum number can be measured directly in experiment. The ratio, R, is defined as

$$R_{e^+e^-} = \frac{\sigma(e^+e^- \to hadrons)}{\sigma(e^+e^- \to \mu^+\mu^-)}. \tag{1.11}$$

The process with hadronic final states is $e^+e^- \to \gamma^*, Z^* \to q\bar{q} \to hadrons$ and the electroweak process is $e^+e^- \to \gamma^*, Z^* \to \mu^+\mu^-$. The value of $R_{e^+e^-}$ below Z peak is $R_{e^+e^-} \approx N_C \sum_{f=1}^{N_f} Q_f^2$. The experimental results for $R_{e^+e^-}$ is shown in Fig. 1.2. Without taking the strong interaction into account, $N_C = 3$ can give good prediction.

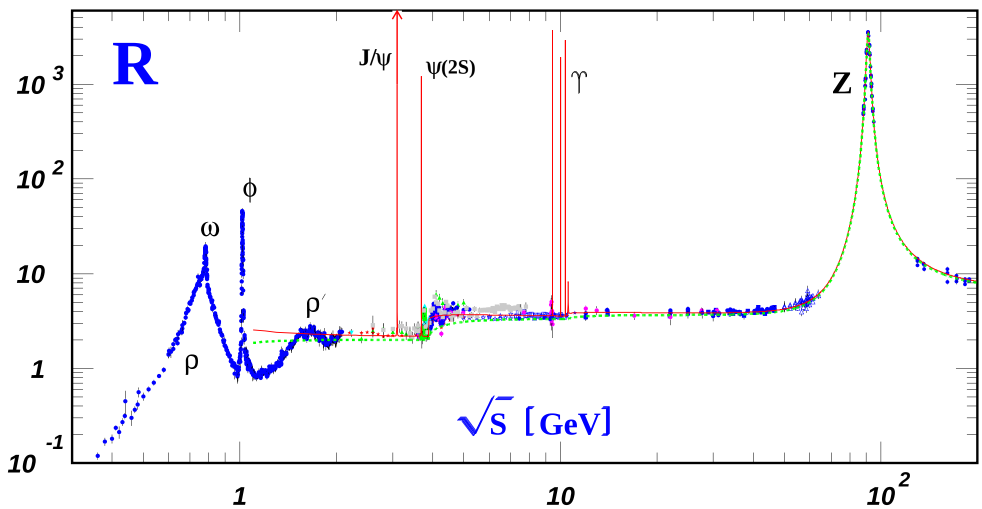

Figure 1.2 World data on the ratio $R_{e^+e^-}$ [4].

Non-Abelian Gauge Theory

In color space, $\psi \equiv (\psi_1, \psi_2, \psi_3)$ can be used to denote a multiplet fermion fields. The free Lagrangian

$$\mathscr{L}_0 = \bar{\psi}(i\gamma^\mu \partial_\mu - m)\psi. \tag{1.12}$$

which is invariant under global $SU(3)_C$ transformation. The $SU(3)_C$ matrices can be written as

$$U = \exp\{i\frac{\lambda^a}{2}\theta_a\}, \tag{1.13}$$

where $\frac{1}{2}\lambda^a(a = 1, 2, ..., 8)$ are the generators of the fundmental representation of $SU(3)_C$ algebra. Matrices λ^a are traceless and satisfy the communication relations

$$\left[\frac{\lambda^a}{2}, \frac{\lambda^b}{2}\right] = i f^{abc}\frac{\lambda^c}{2} \tag{1.14}$$

f^{abc} are the $SU(3)_C$ structure constants. They are real and antisymmetric. The global symmetry can now be extended to local symmetry by changing the constant θ_a to $\theta_a(x)$. At the same time, a

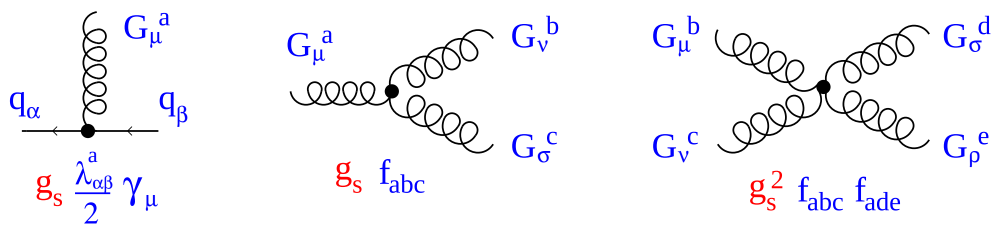

Figure 1.3 QCD interaction vertices [5].

covariant derivative is introduced,

$$\partial_\mu \to D_\mu = \partial_\mu - igG_\mu(x). \tag{1.15}$$

where the matrix G_μ can be expanded

$$G_\mu(x) = (\frac{\lambda^a}{2})G_a^\mu(x). \tag{1.16}$$

The non-Abelian gauge transformation is more complex than QED case. The final $SU(3)_c$ invariant Lagrangian for QCD is

$$\mathscr{L}_{QCD} = \bar{\psi}(i\gamma^\mu D_\mu - m)\psi - \frac{1}{4}G^a_{\mu\nu}G^{a,\mu\nu}, \tag{1.17}$$

which indicates there will be gluon field. The interaction vertices are shown in Fig. 1.3. One important feature of QCD is that the gluons have self interactions.

1.1.4 Electoweak Interaction

Lots of low energy experiments indicate that only left handed fermion and right handed anti-fermion participate the weak interaction. The intermediate vector bosons, $W^\pm$ and Z were predicted by theory and discovered by experiments.

The fermions can be grouped with left-handed doublets and right-handed singlets. They are the fundamental representations of group $SU(2)\times U(1)$,

$$\begin{pmatrix}\nu_e\\ e\end{pmatrix}_L,\ \begin{pmatrix}\nu_\mu\\ \mu\end{pmatrix}_L,\ \begin{pmatrix}\nu_\tau\\ \tau\end{pmatrix}_L,\ e_R,\ \nu_R,\ \tau_R$$

$$\begin{pmatrix}u\\ d\end{pmatrix}_L,\ \begin{pmatrix}c\\ s\end{pmatrix}_L,\ \begin{pmatrix}t\\ b\end{pmatrix}_L,\ u_R,\ d_R,\ c_R,\ s_R,\ t_R,\ b_R \tag{1.18}$$

The Lagrangian of electroweak interaction can be written,

$$\mathscr{L}_{EW} = \mathscr{L}_F + \mathscr{L}_G, \tag{1.19}$$

where $\mathscr{L}_F$ is the term for fermions, $\mathscr{L}_G$ is the gauge field term.

$$\mathscr{L}_F = i\bar{\psi}_L\gamma^\mu D_{\mu L}\psi_L + i\bar{\psi}_R\gamma^\mu D_{\mu R}\psi_R, \tag{1.20}$$

The covariant derivatives are ,

$$D_{\mu L}\psi_L = (\partial_\mu + ig\frac{\sigma_i}{2}W^i_\mu + ig'\frac{Y_L}{2}B_\mu)\psi_L \tag{1.21}$$

$$D_{\mu R}\psi_R = (\partial_\mu + ig'\frac{Y_R}{2}B_\mu)\psi_R, \tag{1.22}$$

where σ_i are Pauli spin matrices and Y is the weak hyper-charge. The Lagrangian for gauge field is,

$$\mathscr{L}_G = -\frac{1}{4}W^i_{\mu\nu}W_i^{\mu\nu} - \frac{1}{4}B_{\mu\nu}B^{\mu\nu}, \tag{1.23}$$

where the fields are,

$$W^i_{\mu\nu} = \partial_\mu W^i_\nu - \partial_\nu W^i_\mu + g\varepsilon^{ijk}W^j_\mu W^k_\nu \quad \text{and} \tag{1.24}$$

$$B_{\mu\nu} = \partial_\mu B_\nu - \partial_\nu B_\mu, \tag{1.25}$$

where g is the weak coupling constant. The observable weak gauge bosons $W^\pm$, Z and γ can be the linear combinations of the four gauge fields B_μ and W^i_μ,

$$W^\pm_\mu = \frac{1}{\sqrt{2}}(W^1_\mu \mp iW^2_\mu) \tag{1.26}$$

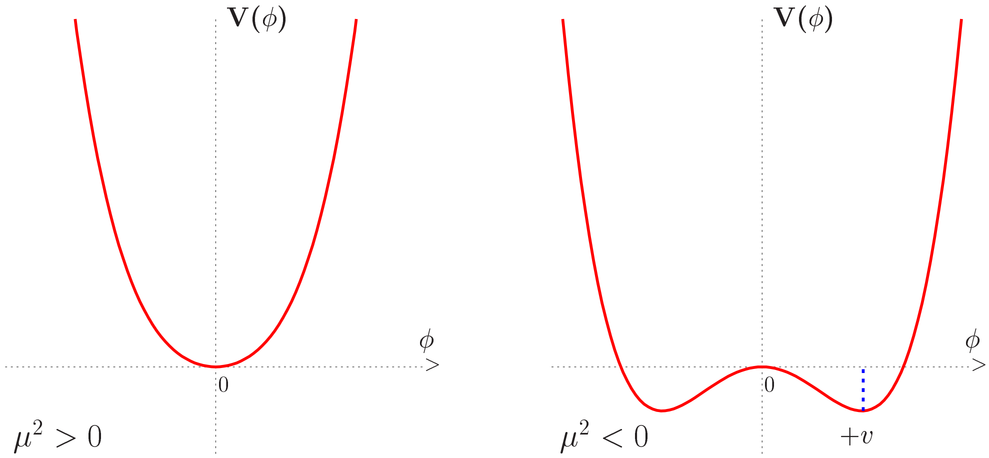

Figure 1.4 The potential V for the scalar filed [6].

and

$$\begin{pmatrix} Z_\mu \\ A_\mu \end{pmatrix} = \begin{pmatrix} \cos\theta_W & \sin\theta_W \\ -\sin\theta_W & \cos\theta_W \end{pmatrix} \begin{pmatrix} W_\mu^3 \\ B_\mu \end{pmatrix}. \tag{1.27}$$

The $cos\theta_W$ can be determined by $g/\sqrt{g^2+g'^2}$. Right now the gauge field are massless fields.

1.2 The Higgs Mechanism

1.2.1 The Goldstone Theorem

One can first consider a scalar real field ϕ in this Lagrangian

$$\mathscr{L} = \frac{1}{2}\partial_\mu\phi\partial^\mu\phi - V(\phi), \tag{1.28}$$

where $V(\phi) = \frac{1}{2}\mu^2\phi^2 + \frac{1}{4}\lambda\phi^4$. Since there are no cubic terms, the Lagrangian will not change if one does a $\phi \to -\phi$ operation. The self-coupling λ is positive. If μ^2 is positive, the potential $V(\phi)$

will also be positive, like the left plot of Fig. 1.4. If $\mu^2 < 0$, the minimum value of $V(\phi)$ is at $\phi_0^2 = -\frac{\mu^2}{\lambda} \equiv v^2$.

One can consider a complex scalar field. The Lagrangian

$$\mathscr{L} = \partial_\mu \phi^\dagger \partial^\mu \phi - V(\phi) \tag{1.29}$$

where $V(\phi) = \mu^2 \phi^\dagger \phi + h\left(\phi^\dagger \phi\right)^2$. The Lagrangian is invariant under global transformation.

$$\phi(x) \to \phi'(x) = \exp\{i\alpha\}\phi(x). \tag{1.30}$$

For $\mu^2 < 0$, the potential has a minimum at

$$|\phi(x)_0| = \sqrt{\frac{-\mu^2}{2h}} \equiv \frac{v}{\sqrt{2}}, \tag{1.31}$$

which has solutions for different phase states $\phi(x)_0 = \frac{v}{2}\exp\{i\alpha\}$. One can choose arbitrary value of α, for example $\alpha = 0$. Then the global phase symmetry is spontaneously broken. This is called Spontaneous Symmetry Breaking (SSB). One can try to use real fields to parametrize the complex fields over the ground states.

$$\phi(x) = \frac{1}{\sqrt{2}}\left[v + \varphi_1(x) + i\,\varphi_2(x)\right], \tag{1.32}$$

where φ_1 and φ_2 are real fields. The new potential will be

$$V(\phi) = V(\phi_0) - \mu^2 \varphi_1^2 + h\,v\,\varphi_1\left(\varphi_1^2 + \varphi_2^2\right) + \frac{h}{4}\left(\varphi_1^2 + \varphi_2^2\right)^2 \tag{1.33}$$

The φ_1 can describe a field with mass $-2\mu^2$. φ_2 is still massless. Generally, SSB is associated with massless excitations. This is Goldstone theorem.

1.2.2 The Higgs-Kibble Mechanism

Goldstone theorem doesn't solve the problem. It introduces more massless fields. One can apply this theorem to local gauge symmetry [20, 21] by introducing an $SU(2)_L$ doublet of complex scalar fields.

$$\phi(x) \equiv \begin{pmatrix} \phi^{\dagger}(x) \\ \phi^{0}(x) \end{pmatrix}. \tag{1.34}$$

The Lagrangian in 1.28 can be gauge invariant

$$\mathscr{L}_S = \left(D_\mu \phi\right)^{\dagger} D^{\mu}\phi - \mu^2 \phi^{\dagger}\phi - h\left(\phi^{\dagger}\phi\right)^2, \tag{1.35}$$

where $h > 0$ and $\mu^2 < 0$. Now the covariant derivative is

$$D^{\mu}\phi = \left[\partial^{\mu} + i g \widetilde{W}^{\mu} + i g' y_{\phi} B^{\mu}\right]\phi \tag{1.36}$$

with $y_{\phi} = 1/2$. The vacuum expectation value will be

$$< 0|\phi|0 >= \sqrt{\frac{-\mu^2}{2h}} \equiv \frac{v}{2}. \tag{1.37}$$

The scalar doublet fields can be parametrized

$$\phi(x) = \exp\{i\frac{\sigma_i}{2}\alpha^i(x)\}\frac{1}{\sqrt{2}}\begin{pmatrix} 0 \\ v + H(x) \end{pmatrix}, \tag{1.38}$$

where α^i are three massless Goldstone bosons associated with SSB. The covariant derivative 1.36 can be expanded using the Eq. 1.38 :

$$\left(D_\mu \phi\right)^{\dagger} D^{\mu}\phi \to \frac{1}{2}\partial_\mu H \partial^\mu H + (v+H)^2\left\{\frac{g^2}{4}W_\mu^{\dagger}W^{\mu} + \frac{g^2}{8\cos^2\theta_W}Z_\mu Z^\mu\right\}, \tag{1.39}$$

with the physical gauge $\theta^i = 0$. It 1.39 contains the mass terms for W and Z,

$$m_W = cos\theta_W m_Z = \frac{gv}{2}. \tag{1.40}$$

After SSB, the three Goldstone bosons are absorbed by the weak gauge boson. And the gauge bosons become massive which needs longitudinal polarization. So the total degrees of freedom don't change before and after SSB.

The vacuum expectation value v can be measured via the muon decay, which is $\mu^- \to e^- \bar{\nu}_e \nu_\mu$. Since the W boson is so heavy, the W propagator shrinks to a point. The whole process can be approximated as a four-fermion interaction.

$$\frac{g^2}{M_W^2 - q^2} \approx \frac{g^2}{M_W^2} \equiv 4\sqrt{2} G_F. \tag{1.41}$$

By measuring the muon lifetime, one can get the value of G_F and the scalar vaccum expectation value $v = 246\, GeV$.

1.2.3 Experimental Limits

Since the Higgs contributes to the high order correction to the electroweak interaction, the mass of Higgs can be constrainted by the high-precision electroweak measurement indirectly. The measurement of Z boson mass and decay width, the measurement of W boson mass and decay width and the mass of top quark give the mass of Higgs an upper limit of $m_H < 185$ GeV at 95% CL.

The mass of Higgs can also be measured directly by the Large Electron Positron Collider (LEP). The Higgs boson can be produced via $e^+e^- \to Z^* \to HZ$ channel at LEP. A lower limit on the Higgs mass, $m_H > 114.4$ GeV at 95% CL was obtained. At Tevatron, the exclusion of Higgs mass is between 160 GeV and 170 GeV at 95% [22].

1.3 The Higgs Boson Search at LHC

LHC provides proton-proton collisions at a center-of-mass energy of $\sqrt{s} = 7$ TeV. The Higgs boson can be produced at different channels and the mass of Higgs can be searched at a large range.

1.3.1 The Production of Higgs Boson

The Higgs can be produced via several channels at hadron collider. Fig. 1.7 shows the dominant Higgs production processes, gluon gluon fusion (ggF), vector boson fusion (VBF), Higgs-strahlung

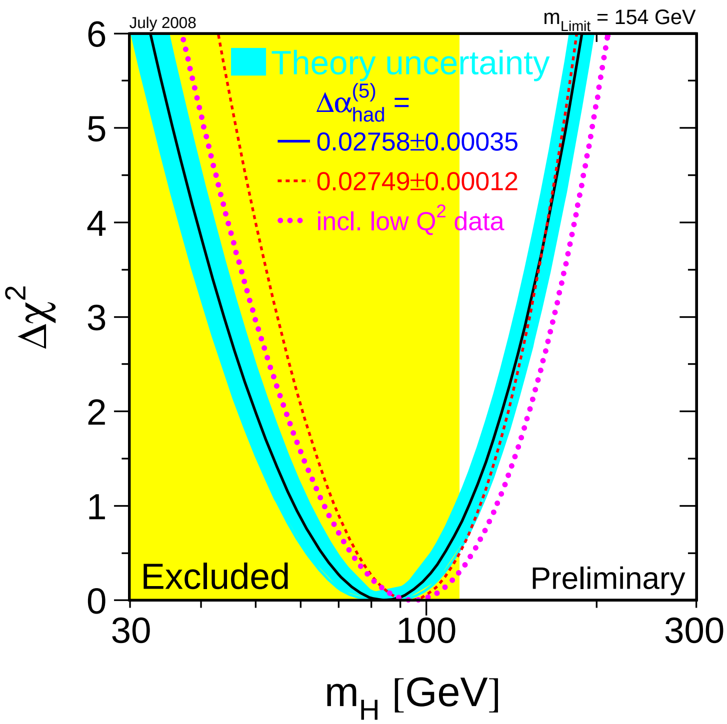

Figure 1.5 The $\Delta\chi^2$ of the fit to the electroweak precision data. The blue/shaded band indicates the theoretical uncertainties due to unknown higher order corrections. The vertical band indicates the 95% exclusion limit from direct searches [7].

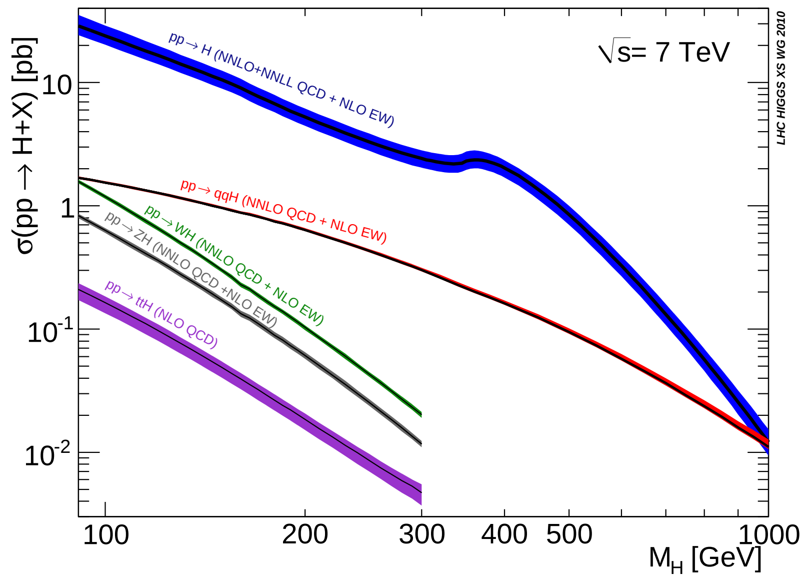

Figure 1.6 Cross section of the Standard Model Higgs for LHC at $\sqrt{s} = 7$ TeV [8].

and the associated production with top-quark pair. The cross section of these processes can be found at Fig. 1.6. The gluon gluon fusion is the dominant production process. The cross section of vector boson fusion is smaller than gluon gluon fusion. The kinematic feature of vector boson fusion is that it has two forward jets, which provides a method to suppress the large background.

1.3.2 The Decay of Higgs Boson

The Higgs can decay to several channels (Fig. 1.8). The Higgs coupling to vector bosons and fermions are proportional to the masses of the particles. It can decay to gg and $\gamma\gamma$ via a top loop. It also can directly decay to $q\bar{q}$, like $t\bar{t}$ (high Higgs mass region), $b\bar{b}$ (low Higgs mass region). The Higgs to WW and ZZ channels are very important for the Higgs search at intermediate and high Higgs mass region 1.9.

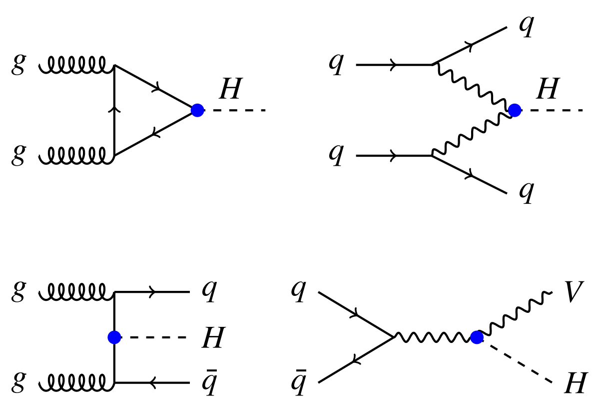

Figure 1.7 The dominant SM Higgs production in pp collisions at LHC.

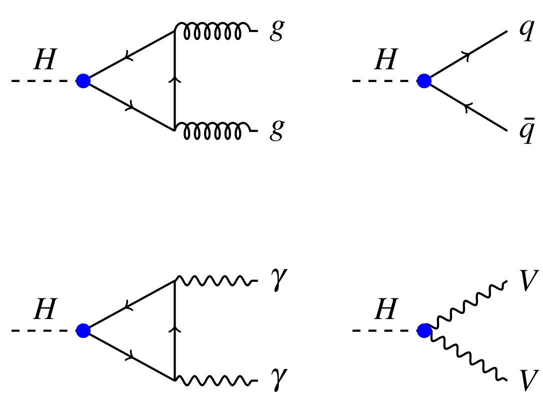

Figure 1.8 The dominant SM Higgs decay channels.

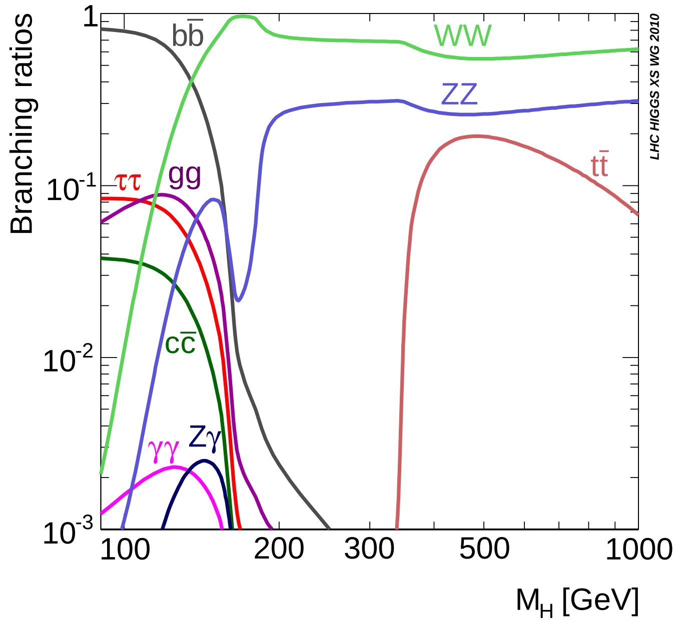

Figure 1.9 Branching ratio of the Standard Model Higgs [8].

1.3.3 Phenomenology of pp Collisions

The initial states of all the Higgs production processes in hadron collider are quarks or gluons. In order to calculate the cross section of physics processes in pp collision, one need *parton model* to give prediction because no partons can be observed in the experiment. The point of *parton model* is to connect the σ_{Hadron} with σ_{Parton}. That certainly makes the Standard Model so useful that it can predict the kinematics of your Higgs production, but also describe the kinematics of your background processes, which may be more useful sometimes. The cross section in hadron level can be written as

$$\sigma_{Hadron} = \int dx_1 \int dx_2\, f_1(x1, Q^2)\, f_2(x2, Q^2)\, \hat{\sigma}(x1p, x2p, Q^2), \tag{1.42}$$

where f_1 and f_2 are the parton distribution functions (PDF) at scale Q^2, x_1 and x_2 are the momentum fractions of partons within the hadron, p is the momentum of hadron. This is so called *factorization theorem*. The $\hat{\sigma}$ is the cross section of parton level which can be calculated by perturbation theory due to the short distance property. Because PDFs are soft-interactions, they can not be calculated. But they can be measured in data at scale Q_0 and can be applied to another process with scale Q_1 [23].

Theoretical calculation based on *parton model* can only go to several final partons with Leading Order (LO). But in experiment, the final jet multiplicity can be very large due to final state radiation (FSR). And one also has to take into account initial state radiation (ISR). A model called *parton shower* will help solve this problem at some level. The advantage of this model is it can be implemented as computer algorithm using Monte Carlo (MC) technique. Fig. 1.10 shows the model of pp collisions. After *parton shower*, the partons will become to color-singlet hadrons with *hadronization*, which can be modeled by phenomenological models like Lund string model [9]. Another non-perturbative effects in pp collisions is *underling event*, which is the interaction between the soft-partons in addition to the hard process in hadron collider. The *underling event* can

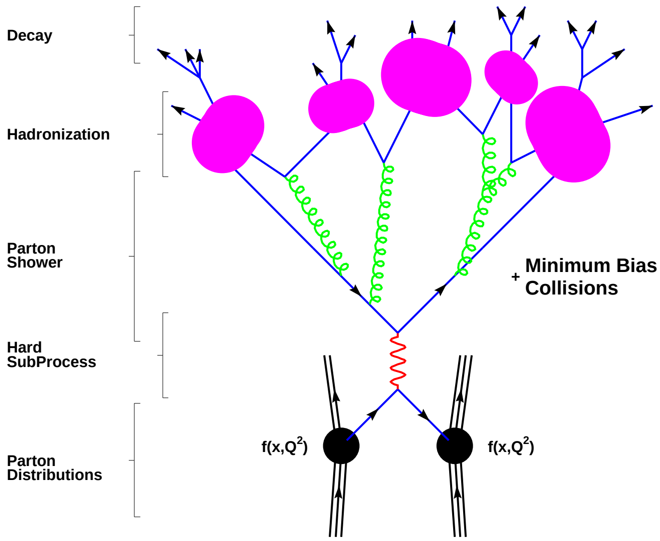

Figure 1.10 The model of *pp* collision [9].

be modeled by MC generators and can be turned to the data.

Chapter 2

The LHC and ATLAS Detector

2.1 The Large Hadron Collider

The Large Hadron Collider (LHC) is a proton-proton (also lead-lead) collider machine which locates at the border between Switzerland and France [24]. The machine was built in LEP 27 km tunnel which is 50-100 m underground. The LHC started to be operational at fall 2009 with 900 GeV center-of-mass energy. From March 30th 2010, LHC is running with center-of-mass energy 7 TeV. The center-of-mass energy of LHC is already about 3.7 times larger than the Tevatron, which was closed on October 5, 2011.

The reason to build a proton-proton collider is that the anti-protons are difficulty to create. Anti-protons can be produced by lots of protons colliding with fixed targets. In order to get high luminosity, lots of anti-protons have to be made in short time. The advantage of $p\bar{p}$ collider is that it can use the same magnetic channel.

In LHC, two protons beams run in opposite directions which needs two opposite sign magnetic fields to bend them. The beams can be brought to several crossing points as shown in Fig. 2.1. To bend the two beams in the circle, 1232 dipole magnets (14.3 m for each) with a field strength 8.3 T

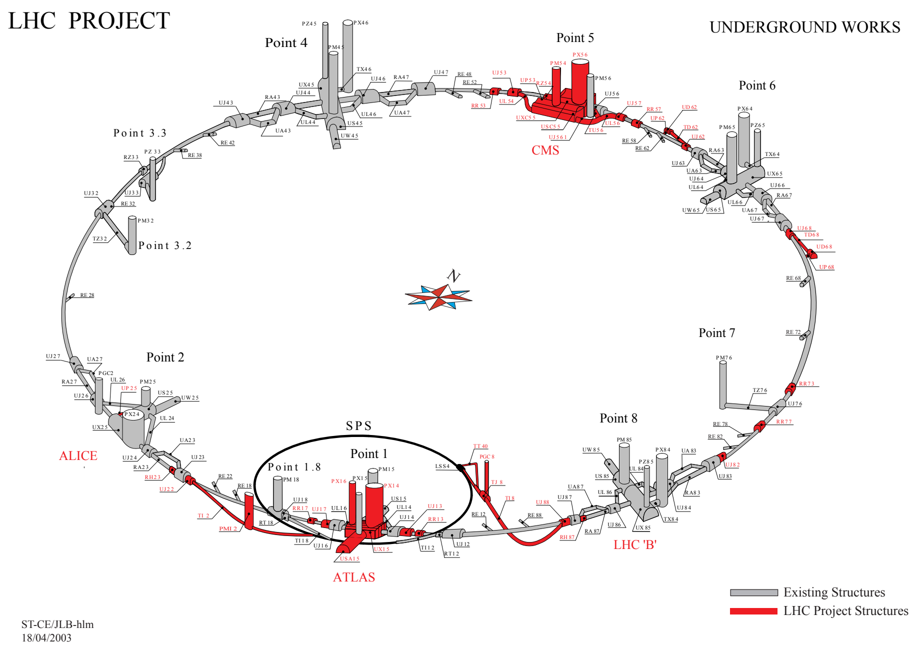

Figure 2.1 The LHC layout.

are used. The magnets are cooled to 1.9 K to reach super conductivity. Because there is no enough space for two cryostat systems in the tunnel, one cryostat system is used.

The beams start form ionized hydrogen. The protons and electrons can be separated by electromagnetic fields. Then the protons are accelerated to 50 MeV in the *liner particle accelerator*. The next accelerators are *Booster* for 1.4 GeV, *Proton Synchrotron* for 26 GeV, *Super Proton Synchrotron* for 450 GeV. After that, the protons will be injected into LHC. The protons are grouped into bunches with a bunch spacing 25 ns. The LHC is designed to fill 2880 bunches with 1.1×10^{11} protons in each bunch. The instantaneous luminosity can be calculated from machine parameters.

$$\mathscr{L} = \frac{N_b^2 \cdot n_b \cdot f \cdot \gamma \cdot F}{4\pi \cdot \varepsilon \cdot \beta^*}, \tag{2.1}$$

where N_b is then number of particles in one bunch, n_b is the number of bunches, f is the revolution frequency, γ is the relativistic gamma factor, ε is the normalized transverse beam emittance, β^* is

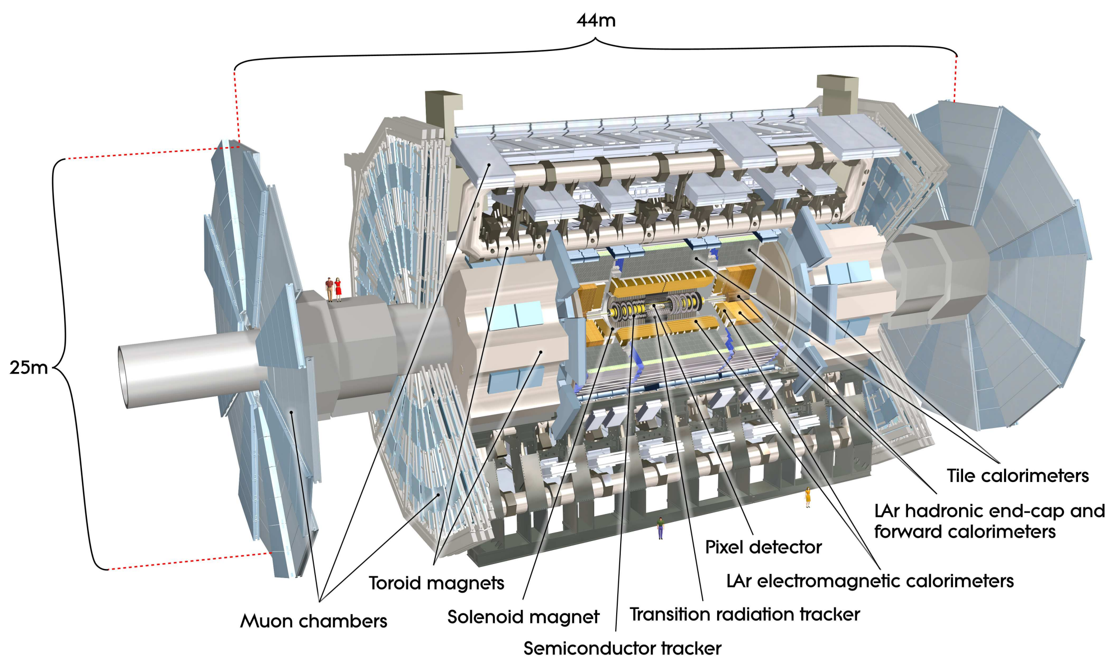

Figure 2.2 The ATLAS detector.

the beta function at the collision point and F is the geometric luminosity reduction factor. More information about luminosity parameters can be found in Ref. [25].

2.2 The ATLAS Detector

The high energy and luminosity of the LHC provides good opportunities for almost all the physics channels from Standard Model precise measurement to new physics search like Higgs, SUSY searches. The design of the ATLAS (**A** **T**oroidal **LHC** **A**pparatu**S**) detector [26, 27] has been driven by the physics need, especially the understanding of the electroweak theory in Standard Model.

Higgs can decay to various channels, like $\gamma\gamma$, WW, ZZ, $\tau\tau$ and $b\bar{b}$. In order to cover all the channels and mass points, ATLAS detector has to reach high resolution for electrons, muons, photons, excellent secondary primary vertex reconstruction for b-jet tagging, good reconstruction for τ leptons and high resolution for missing transverse energy and jets. All the objects can be used for other measurements and searches, like SUSY searches and SM measurements.

A robust trigger system has to be designed to be able to select rare interesting physics events within 25 ns. And each bunch crossing has about 23 interactions.

2.2.1 Coordinate System

ALTAS is using a right-handed x, y and z coordinate system. The origin of the coordinate is the interaction point. The direction of x is defined as starting from the interaction to the center of the LHC ring. The positive y is pointing upwards. The z-axis is defined by the beam direction. The azimuthal angle ϕ is measured around the beam axis. The polar angle θ is the angle from the beam axis. The *rapidity* variable is very important in HEP,

$$y = \frac{1}{2}\ln\frac{E-p_z}{E+p_z}, \tag{2.2}$$

For the low mass particle, it can be simplified as *pseudo-rapidity*,

$$\eta = -\ln\tan\frac{\theta}{2}. \tag{2.3}$$

In order to describe the distance between two objects in η-ϕ space, ΔR is defined as,

$$\Delta R = \sqrt{(\Delta\eta)^2 + (\Delta\phi)^2}. \tag{2.4}$$

Another important variable in hadron collider is missing transverse energy ($E_{\mathrm{T}}^{\mathrm{miss}}$) which is defined as,

$$\begin{aligned} E_{\mathrm{x}}^{\mathrm{miss}} &= -\sum_{particles} E_x, \\ E_{\mathrm{y}}^{\mathrm{miss}} &= -\sum_{particles} E_y, \\ E_{\mathrm{T}}^{\mathrm{miss}} &\equiv \sqrt{(E_{\mathrm{x}}^{\mathrm{miss}})^2 + (E_{\mathrm{y}}^{\mathrm{miss}})^2}. \end{aligned} \tag{2.5}$$

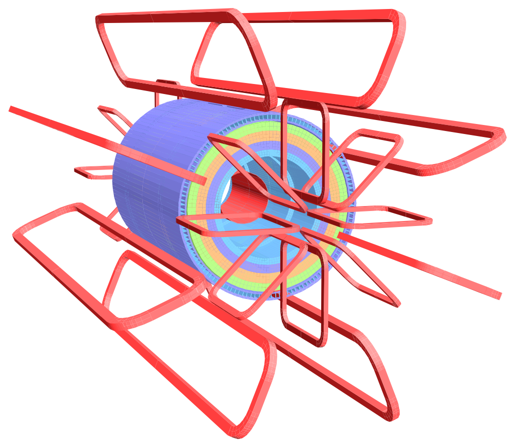

Figure 2.3 Geometry of magnet system.

2.2.2 Magnet System

ATLAS needs magnetic field to bend the charge particles to measure their momenta. In order to increase the resolution of high p_T particles, a strong magnet field is essential. The magnetic system of ATLAS is a superconducing magnet system which is 22 m in diameter and 26 m long with a stored energy of 1.6 GJ. The geometry of the magnet system is displayed in Fig. 2.3 with a central solenoid and toroid coils.

The central solenoid is designed to provide a 2 T axial field for the inner detector along the beam axis direction. It is operated at 7.7 kA nominal operational current with a temperature of 4.5 K. Since the solenoid is between the inner detector and LAr calorimeter, the thickness of the solenoid material should be kept as low as possible to allow a precise energy measurement of particles in calorimeter. Therefore, the solenoid windings and LAr calorimeter share a common vaccum vessel which will eliminate two vacuum walls. The inner and outer diameters of the solenoid are 2.46 m and 2.56 m and the axial length is 5.8 m. The mass of coil is 5.4 tons with stored energy 40 MJ. In the case of quench, the amount of energy can be absorbed by the enthalpy of the cold mass by increasing the temperature to a safe value of 120 K.

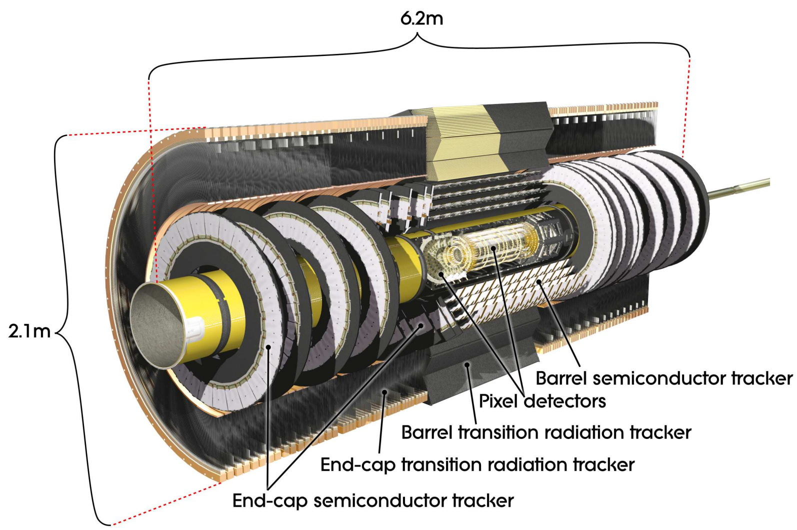

Figure 2.4 Cut-away view of the ATLAS Inner Detector.

The magnetic field for the muon spectrometer is provided by a barrel toroid and two end-cap toriods Fig. 2.3. They will produce a toroidal magnetic field of 0.5 T and 1 T for the muon detectors in the central and end-cap regions. All the toriods consist of eight coils with a nominal operational current of 20.5 kA. The normal temperature is 4.6 K. The barrel toroid is 25.3 m in length with inner and outer diameters of 9.4 m and 20.1 m. The quench detection system can absorb the 1.1 GJ stored energy which leads to a very safe global cold mass temperature of about 58 K.

2.2.3 The Inner Detector

At the LHC design luminosity of $10^{34}\,\mathrm{cm}^{-1}\mathrm{s}^{-1}$, about 1000 tracks will emerge from the collision point every 25 ns within $|\eta| < 2.5$. To provide precise momentum measurement and accurate secondary vertices reconstruction, fast and high granular detectors are used. This is achieved by pixel and silicons (SCT) trackers which are surrounded by the Transition Radiation Tracker (TRT) as shown in Fig. 2.4.

The Inner Detector (ID) is immersed in a 2 T magnetic field provided by central solenoid. The silicon pixel detectors, the innermost part, provide the highest granularity around the vertex region. The pixel layers are segmented in $R-\phi$ and z. The intrinsic accuracies are 10 μm ($R-\phi$) and 115 μm (z) both in barrel region and in disks . The total number of readout channels in pixel detector is 80.4 million. The SCT has eight strip layers for each track. In each layer, one set of strips are parallel to the beam direction and another set of strips have a small angle (40 mrad) with the first set of strips to measure both coordinates. The intrinsic accuracies are 17 mum ($R-\phi$) and 580 μm (z) in barrel region and in disks. The SCT has about 6.3 million readout channels. The TRT consists of 4 mm diameter straw tubes which only provides $R-\phi$ information within $|\eta| < 2.0$. The straws in the barrel region are parallel to the beam axis and 114 cm long. In the end-cap region, the straws are 37 cm long and arranged radially in the wheels. The total number of TRT readout channels is about 351,000.

The R coverage of precision trackers (pixel and SCT) is $45.5 < R < 560$ mm. The TRT covers region $554 < R < 1082$ mm. Although TRT has low precision compared with pixel and SCT, it is compensated by the large R coverage and longer measured track length. The xenon-based gas mixture of the straw tubes can enhance the electron identification capabilities by measuring the transition-radiation photons.

2.2.4 Calorimeter

The calorimeter detector has electromagnetic (EM) calorimeter inside and hadron calorimeter outside. It can cover the range $|\eta| < 4.9$ with different techniques. The samplings of calorimeter are shown in Fig. 2.5. Calorimeters have to provide good measurement for electromagnetic and hadronic showers, and have to limit the punch-through into the muon system. Therefore, the total thickness has to be sufficient to reduce the punch-through. The EM calorimeter provides 9.7 interaction lengths (λ) in barrel, and outer support provides 1.3 λ.

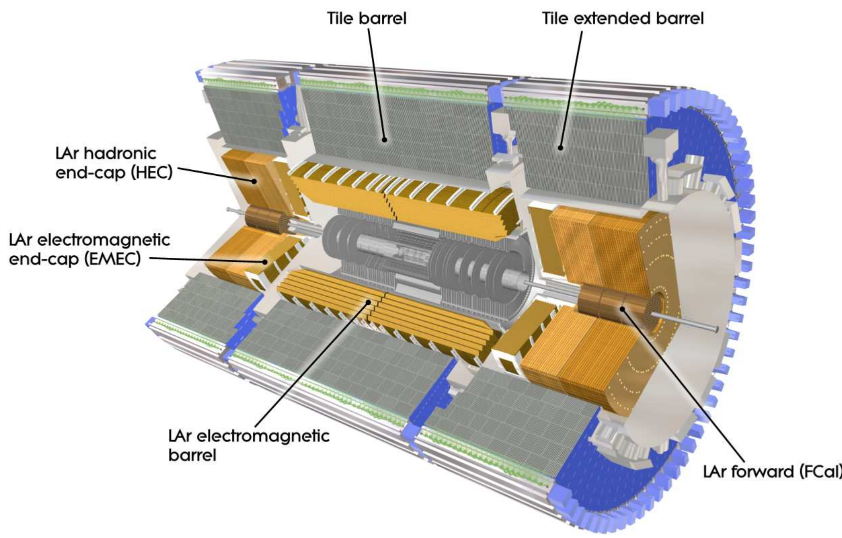

Figure 2.5 Cut-away view of the ATLAS calorimeter system.

LAr EM Calorimeter

The EM calorimeter is the first detector where particles enter after exit from inner detector. The EM calorimeter has barrel part ($|\eta| < 1.475$) and end-cap part ($1.375 < |\eta| < 3.2$). Both of them are using lead-liquid-argon layers for detection. In the longitudinal direction, the EM calorimeter has four layers which are presampler, η-strip, EM-Middle and EM-Back layers. The presampler can be used to recover the energy lost in the material upstreams. The η-strip has fine granularity in η direction which is very sensitive to the eletromagnetic shower shape. It not only can separate electrons and photons from hadronic showers but also resolve the two close-by photons from π^0 decay. The EM-Middle layer provides good granularity both in η and ϕ. It is the thickest part of EM calorimeter which has about 16 radiation length (X_0). The outmost part of EM calorimeter is EM-Back which completes the EM system.

The EM calorimeter has an accordion geometry for absorbers and the electrodes in barrel and end-cap. This structure offers a naturally full ϕ coverage without any cracks. Fig. 2.6 shows the

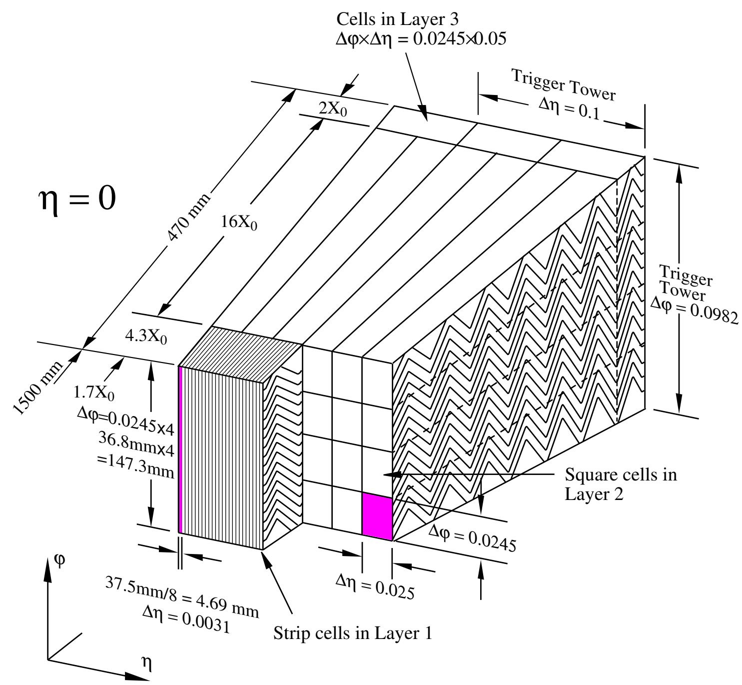

Figure 2.6 Sketch of a barrel module where the different layers are clearly visible with the ganging of electrodes in ϕ. The granularity in η and ϕ of the cells of each of the three layers and of the trigger towers is also shown.

geometry of barrel module.

LAr Readout

The electrodes of LAr calorimeter are grouped to readout cells. The cell signals are read out through 1524 Front-End Boards (FEBs) with 128 channels each. The FEBs perform analog processing including amplification and shaping except for HEC. Then it stores the signal and is waiting for the L1 trigger decision. FEBs are using optical fibers to transmit digitized signals to Readout Drivers (RODs). Fig. 2.7 shows the ADC counts in the function of time.

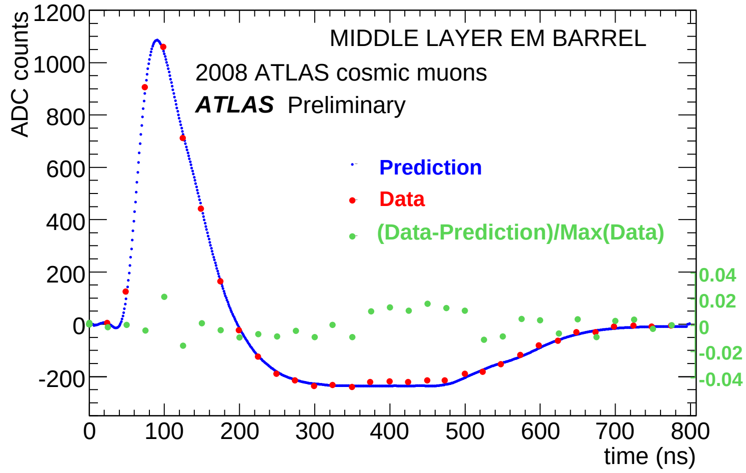

Figure 2.7 Ionization pulse shape in EM-Middle layer.

Hadronic Calorimeter

The hadronic calorimeter is placed outside the EM calorimeter. At the barrel region, tile calorimeter is used with barrel ($|\eta| < 1.0$) region and two extended barrels ($0.8 < |\eta| < 1.7$). It is a sampling calorimeter using steel as the absorber and scintillating tiles as the active material. The LAr hadronic end-cap calorimeter (HEC) locates behind the end-cap EM calorimeter directly with η range $1.5 < |\eta| < 3.2$. It is using LAr as the active medium. Forward calorimeter (FCAL) covers the range $3.1 < |\eta| < 4.9$. The fine segmentation of FCAl allows for forward jets reconstruction.

2.2.5 Muon Detector

The layout of muon detector, which is the outermost detector, is show in Fig. 2.8. The muon detectors provide muon momentum measurement by the magnetic deflection of muon tracks. Monitored Drift Tube (MDT) chambers and Cathode Strip Chambers (CSC) are the used to measure muon momenta in barrel and end-cap region. Resistive Plate Chambers (RPC) in the barrel region and Thin Gap Chambers (TGC) in the end-cap region are the dedicated trigger chambers. The cross-

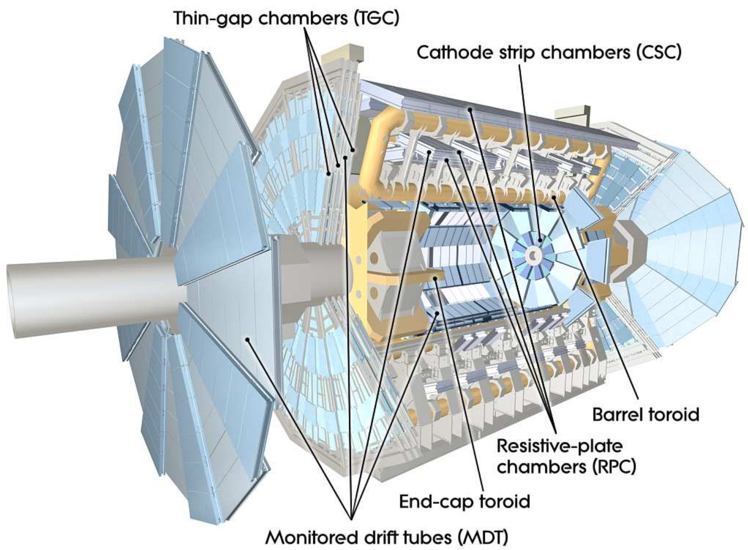

Figure 2.8 Cut-away view of the ATLAS muon system.

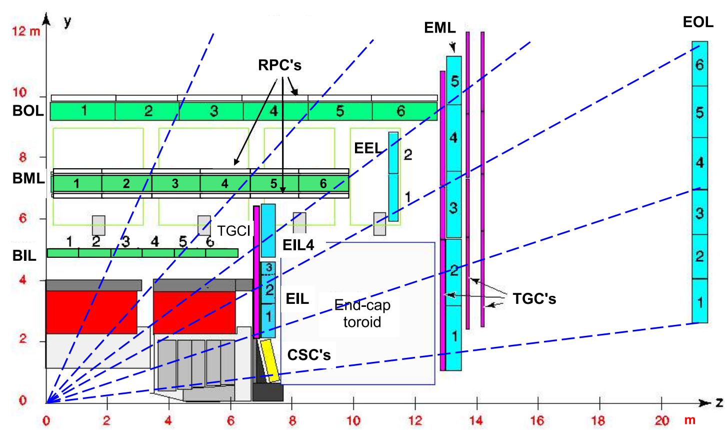

Figure 2.9 Cross-section of the muon system in a plane containing the beam axis (bending plane).

section of the muon system is shown in Fig. 2.9.

Tracking Chambers

The muon momentum can be measured by MDT and CSC chambers. The MDT chambers cover the the region $|\eta| < 2.7$, except for the innermost layer where the CSC covers $2 < |\eta| < 2.7$. The CSCs are multi-wire proportional chambers with a cathode strip readout. The 1088 MDT chambers with a total area of 5500 m^2 provide the main muon tracking momentum measurement. The first letter (B and E) of the MDT chamber name refers to barrel and end-cap. The second and third letters refer to layer (inner, middle and outer) and sector (large and small) types (see Fig. 2.9).

Trigger Chambers

The trigger chambers of muon system provide fast information on muon tracks to allow L1 trigger logic within $|\eta| < 2.4$. They also identify different bunch-crossing and bend the muon tracks which cannot be provided by MDT chambers. The muon momentum as a given p_T is increasing at high η, which poses a challenge to the design of the trigger system. Furthermore, the end-cap region has a 10 times higher radiation level than central region. RPCs are used in barrel region ($|\eta| < 1.05$) and TGCs are used in end-cap regions ($1.05 < |\eta| < 2.4$). TGCs are multi-wire proportional chambers which can provide good time resolution and high rate capability. In previous experiments, TGCs demonstrated a high level of reliability.

2.2.6 Trigger System

The designed bunch-crossing rate of LHC is 40 MHz. Every bunch-crossing will have about 25 interactions which will lead the total interaction rate to about 1 GHz. Not all the events can be recorded. The cross sectons for various channels are shown in Fig. 2.10. The interaction rate for interesting events (like Higgs) is very small compared with QCD processes. A trigger system has to be designed to reduce the rate. ATLAS trigger system has three levels: L1, L2 and event filter. The L1 trigger is based on hardware including the information from calorimeter and muon

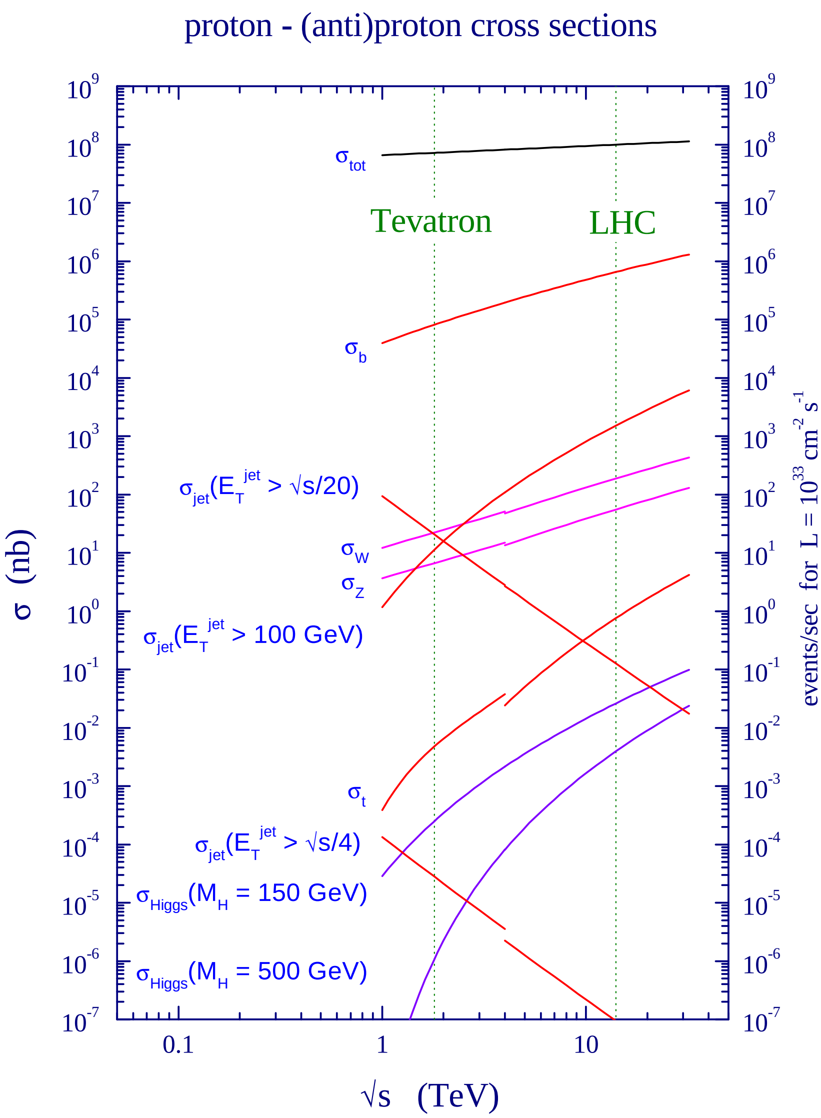

Figure 2.10 QCD predictions for hard-scattering cross sections [10].

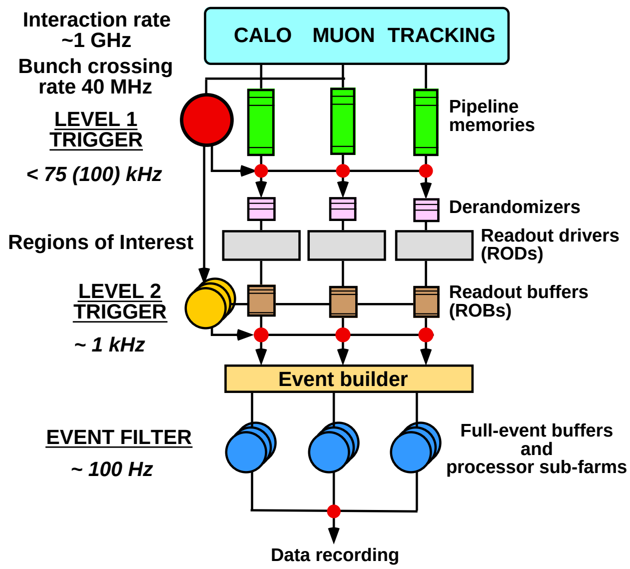

Figure 2.11 Schematic diagram of the ATLAS trigger system.

detector with a latency less than 2 μs. The calorimeter provides the L1 trigger information by trigger towers with a reduced granularity of $\Delta\eta \times \Delta\phi = 0.1 \times 0.1$. The muon detector gives muon trigger information. The L1 trigger reduces the event rate to 75 kHz. The area of these objects are called a region of interest (ROI) which will be passed to L2 trigger. The L2 trigger is only looking at the ROIs provided by L1 trigger. It can use full calorimeter and muon detector granularity. The track information from inner detector becomes available in this level. The event rate is reduced to about 1 kHz by L2. The event filter trigger will fully reconstruct the events accepted by L2 trigger (not only ROIs). The reconstruction in this stage is very similar with offline reconstruction with a final event rate about 100 Hz. All the events accepted by the three trigger systems will be save into storage system as raw data. Fig. 2.11 shows the schematic overview for trigger system.

Chapter 3

Jet Performance and Measurement

The jet reconstruction performance is very important for almost all the physics analyses in ATLAS. Jets plays an important role in the $t\bar{t}$ cross section measurement, SUSY and Higgs boson searches. Jet measurements can also be used as a calibration method for the detector especially at early stages of LHC running. Jet algorithm and reconstruction method will be discussed at Section 3.1. Section 3.2 will be used to describe jet calibration and η intercalibration will be discussed at Section 3.3. Section 3.4 will show the results of inclusive jet cross section measurement. Finally, di-jet resonance search will be shown in Section 3.5.

3.1 Jet Algorithms

The jet finder algorithms in hadron collider should provide a fast and reliable jet reconstruction for different physics objects, like calorimeter towers, topological clusters, tracks and generator level particles.

3.1.1 Guidelines for Jet Algorithms

The jet algorithms have to satisfy several guidelines.

Theoretical guidelines :

- **Infrared safety:** The additional soft particles should not affect the jets reconstruction.
- **Collinear safety:** If a particle is split to two particles in almost the same direction, the jet reconstruction should not change.

If the guidelines are violated, the QCD NLO calculation would diverge.

Experimental guidelines :

- **Detector resolution:** The finite detector spatial and energy resolution should not affect the jet reconstruction significantly.
- **Detector environment:** The electronics noise, dead detector channels and cracks should not change jet reconstruction significantly.
- **Speed:** The jet algorithm has to be fast enough in terms of CPU consumption. The number of jets in a event will be typically 10 to 20 due to the high pile-up environment in LHC.

3.1.2 Anti-k_t Algorithm

In ATLAS, jets are typically reconstructed using anti-k_t algorithm [28] with distance parameters $R = 0.4$ or 0.6. The input objects to the algorithm can be generator level objects or detector level objects. The relative transverse momentum squared are defined as:

$$d_{ij} = min(\frac{1}{k_{ti}^2}, \frac{1}{k_{tj}^2})\frac{\Delta R_{ij}^2}{R^2}, \quad d_{iB} = \frac{1}{k_{ti}^2}, \tag{3.1}$$

where $\Delta R_{ij}^2 = \Delta\eta_{ij}^2 + \Delta\phi_{ij}^2$. R is a distance parameter.

The algorithm is,

- Calculating all the d_{ij} and d_{iB} for all the input objects.
- If the smallest value is d_{ij}, combining the object i and j to new object k. The objects i and j are removed from the list of objects.
- If the smallest value is d_{iB}, the object i is considered to be a jet and has to be removed from the list.

If the parameter R is larger, the value of d_{ij} is smaller. Then more merging is done in a jet. That is why R can be used to control the size of jet.

3.2 Jet Calibration and Topocluster Jets

Jet calibration and jet energy scale (JES) measurement are described in [29].

3.2.1 Topocluster

The input to the jet reconstruction is topological clusters in calorimeters. A topocluster is three-dimensional energy deposition which comes from a particle entering the calorimeter. The clustering will start if the signal significance of the seed cells, $\Gamma \equiv E_{cell}/\sigma_{\mathrm{noise,cell}}$, is bigger than 4. The clustering will include neighboring cells if the $\Gamma > 2$. Finally it will include a last layer of cells if the $\Gamma > 0$ (Fig. 3.1). The topoclustering algorithm also includes a splitting step. It will search for local maximum in all cells in a topocluster. If a local maximum is found, it will be used as seed for a new iteration and the original cluster will be split into more topoclusters. The total energy of a topocluster will be the energy sum of the all the cells in that cluster. The mass of the topocluster is zero. The direction of the topocluster is a unit vector originating from the center of the ATLAS coordinate system pointing to the energy-weighted topocluster barycenter.

3.2.2 Jet Calibration

The particles in the calorimeter will produce electromagnetic showers which can be measured at electromagnetic energy scale (EM scale). The EM scale calibration is obtained from test-beam electron measurement. Muons are used to validate calorimeter response to the electromagnetic energy deposition in hadronic calorimeters. Invariant mass of $Z \rightarrow ee$ events in collision data are used to correct the electromagnetic energy scale in the calorimeters.

The jet energy scale calibration is supposed to restore the hadronic energy of the jet. The calibration constants are derived from the comparison between reconstructed level jets and truth level jets using Monte Carlo. The jet calibration takes into account several detector effects in the jet energy scale :

1. Calorimeter non-compensation (calorimeter can only measure part of the energy deposited by hadrons) due to the energy needed to break the absorber nuclei and the presence of muons and neutrinos in the shower.

2. Dead material effects (non-operational parts of the detector).

3. The energy of jet escaping the calorimeter (leakage).

4. Signal losses in the jet reconstruction.

5. Some particles from truth jets are not included in jet reconstruction.

Hadronic jet energy scale is obtained using the "EM+JES" calibration method. This method derives the calibration factors in bins of p_T and η using a inclusive jet Monte Carlo sample generated with PYTHIA [30]. The detector simulation in ATLAS is done by GEANT4 software [31]. The signal simulated by GEANT4 will be reconstructed by the ATLAS reconstruction software, which is also used to reconstruct real data events.

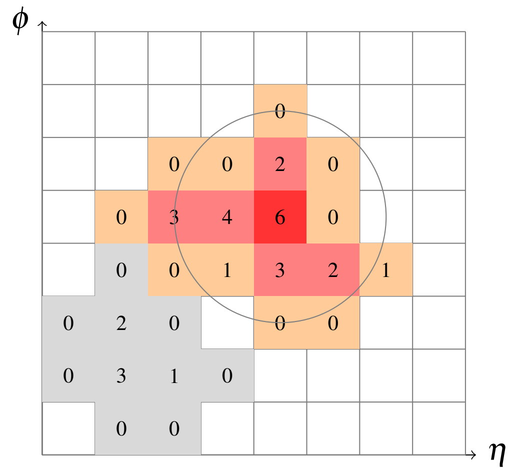

Figure 3.1 Illustration of the topocluster reconstruction. Note that only two dimensions (η,ϕ) are used. The numbers denote of Γ for cells in the (η,ϕ) space.

Fig. 3.2 shows the jet kinematics distributions in data and MC. Both of them are normalized to unit area. The data/MC agreement for the jet p_T distribution is fine although data is harder than MC. One event containing a jet with p_T bigger than 1 TeV is already observed with integrated luminosity 296 nb^{-1}. The data/MC agreement for jet multiplicity is good even PYTHIA is used.

3.2.3 Pile-up Correction

One feature of the LHC is its high instantaneous luminosity which will lead to multiple proton-proton collisions per bunch crossing. That is called pile-up effect. The energy of jet can include the contribution from another proton-proton collisions which are not the event of interest. The pile-up correction in ATLAS is in function of number of reconstructed primary vertices (N_{PV}) and the jet pseudo-rapidity (η). It takes into account the additional energy deposited in a grid of 0.1×0.1 in the (η, ϕ) plane and the average number of towers in a jet. In the first step of calibration, the pile-up correction will be applied.

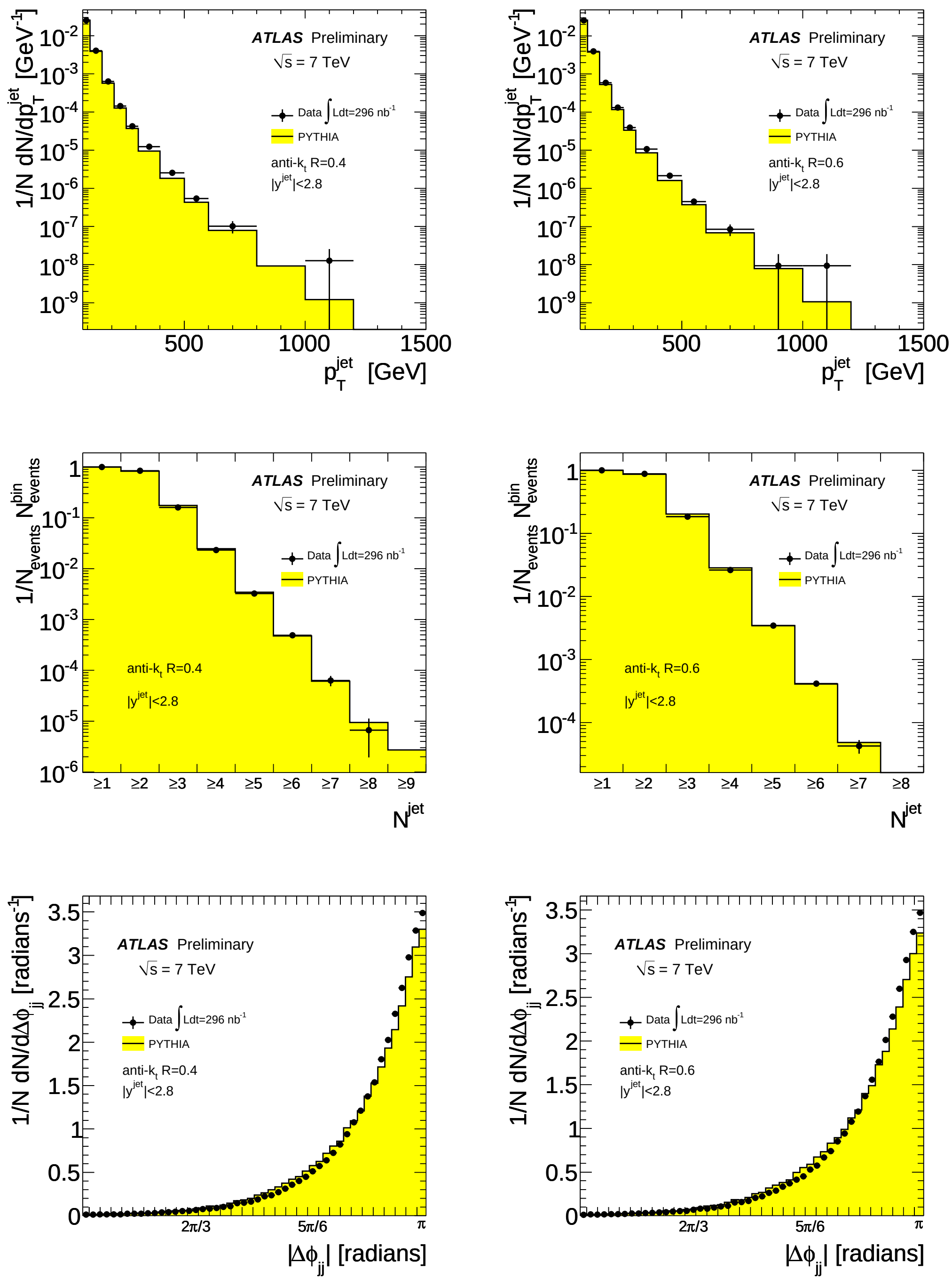

Figure 3.2 Jet kinematics distributions in data and Monte Carlo. Left column is from anti-k_t R=0.4 jet. Right column is from anti-k_t R=0.6 jet. Data and Monte Carlo are normalized to unit area.

3.2.4 Jet Origin Correction

As mentioned above, the default direction of topoclusters is obtained using geometrical center of ATLAS detector as reference point. The jet origin correction will correct each topocluster so that it points back to the primary vertex with the highest associated sum of tracks transverse momenta squared in the event. The new direction of topocluster is obtained using the direction from primary vertex to the topocluster centroid. The new jet four momentum is the vector sum of topocluster four momentum. The angular resolution is improved by this correction.

3.2.5 Final Jet Energy Correction

The last step of the EM+JES calibration is to correct the detector level jet to the truth level jet. The calibration constants are derived from isolated calorimeter jets. The definition of isolated jet is that a jet has no other calorimeter (truth) jet with EM-scale (truth) p_T bigger than 7 GeV within ΔR=2.5R, where R is the distance parameter of jet algorithm. Afterwards, the matching between calorimeter jet and truth jet is done by requiring $\Delta R < 0.3$. The EM-scale jet energy response $\mathscr{R} = E^{EM}_{calo}/E_{truth}$ for each calorimeter-truth jet pair is measured in bins of the truth jet energy E_{truth} and calorimeter η_{det}, which is the original reconstructed jet before jet origin correction. For each (E_{truth}, η_{det}) bin, the measured EM-scale energy response $< \mathscr{R} >$ is defined as the peak position of a Gaussian fit to the E^{EM}_{calo}/E_{truth} distribution and the average calorimeter jet energy $< E^{EM}_{calo} >$ is determined. Jet response function, $\mathscr{F}_{calib,k}(E^{EM}_{calo})$, is obtained by a fit of $< E^{EM}_{calo} >_j$ and $< \mathscr{R} >_j$ for each E_{truth} bin j. The fitting function is defined as,

$$\mathscr{F}_{calib,k}(E^{EM}_{calo}) = \sum_{i=0}^{N_{max}} a_i (\ln E^{EM}_{calo})^i, \tag{3.2}$$

where a_i are free parameters and N_{max} is chosen between 1 and 6 depending on the goodness of the fit. The final jet energy scale correction is,

$$E^{EM+JES}_{calo} = \frac{E^{EM}_{calo}}{\mathscr{F}_{calib,k}(E^{EM}_{calo})|_{\eta_{det}}}. \tag{3.3}$$

After all these corrections, a final jet η correction is done which is supposed to fix biases in the jet direction due to the poorly instrumented regions of calorimeters. That is because the energy response in those regions are lower. The direction of jet is biased towards the better calorimeter regions. The correction will be large in transition regions. But for most regions, it is very small ($\Delta\eta < 0.01$).

3.3 In-situ η Intercalibration

The response of ATLAS detector varies in different η regions due to the different calorimeter materials and technologies used. Fig. 3.3 shows the jet response in different η regions in jet p_T bins. The jet response in transition region ($1.37 < |\eta| < 1.52$) is very low compared with other regions. The di-jet p_T balance can be used to calibrate the detector response in forward region.

3.3.1 Intercalibration Method

The relative calorimeter response can be quantified using the p_T balance of the reference jet and probe jet. The asymmetry A is defined as,

$$A = \frac{p_T^{\mathrm{probe}} - p_T^{\mathrm{ref}}}{p_T^{\mathrm{avg}}}, \tag{3.4}$$

where $p_T^{\mathrm{avg}} = (p_T^{\mathrm{probe}} + p_T^{\mathrm{ref}})/2$. The reference region is defined as $0.1 < |\eta| < 0.6$.The region at $|\eta| < 0.1$ is excluded due to small inhomogeneity of the joint point of the two sides of barrel. The probe region is defined as $|\eta| > 0.6$. As shown in Fig. 3.4, the asymmetry A can be used to derive the calibration factor c of the probe jet using the relation,

$$\frac{p_T^{\mathrm{probe}}}{p_T^{\mathrm{ref}}} = \frac{2+A}{2-A} = 1/c. \tag{3.5}$$

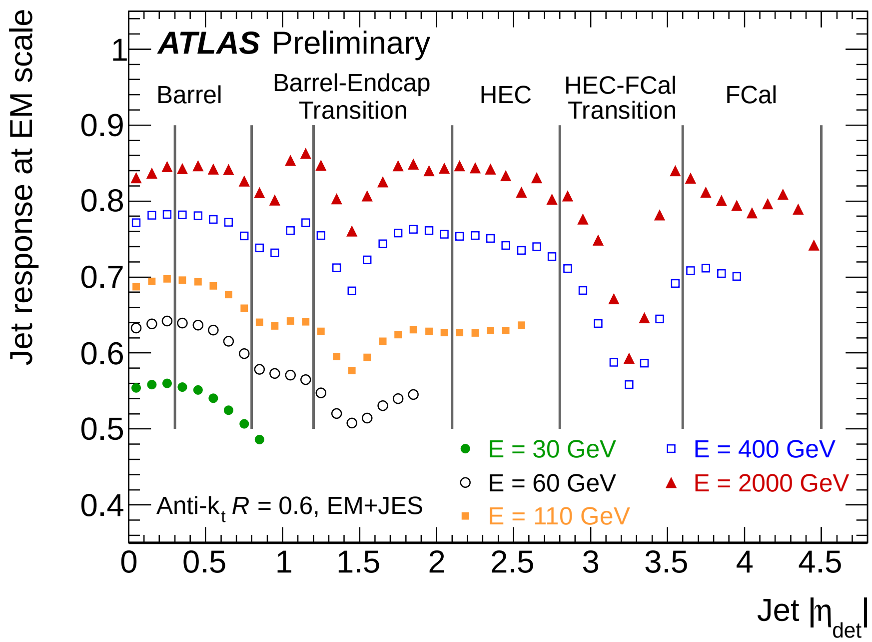

Figure 3.3 Jet response in different calorimeter regions for jet p_T between 30 GeV and 2 TeV [11].

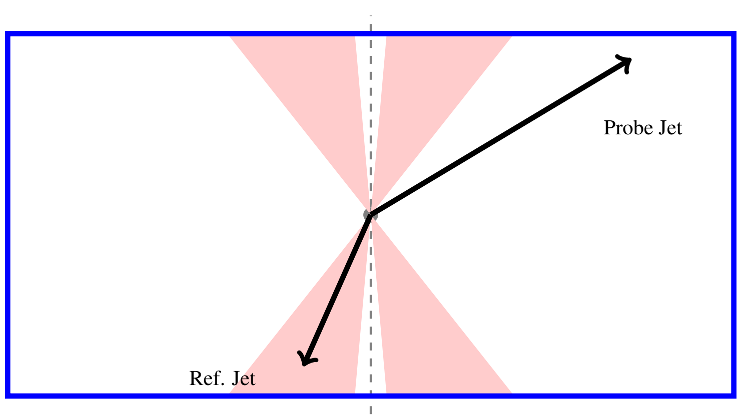

Figure 3.4 Scratch η intercalibration method. The reference jet at low $|\eta|$ region is used to calibrate the probe jet at higher $|\eta|$ region.

The analysis is done in bins of jet η and p_T^{avg}. A_{ik} is the asymmetry for probe jet η bin i and p_T^{avg} bin k. The calibration factor in bin ik can be obtained by,

$$c_{ik} = \frac{2- < A_{ik} >}{2+ < A_{ik} >}, \tag{3.6}$$

where $< A_{ik} >$ is the mean value of A in each bin.

3.3.2 Selection and Results

The following selection cuts are used in the analysis :

- Trigger : For jet with $50 < p_T < 80$ GeV, level one central jet trigger with $p_T > 5$ GeV at electromagnetic scale or level one forward jet trigger with $p_T > 5$ GeV at electromagnetic scale is fired. For jet with $p_T > 80$ GeV, the p_T threshold for central jet trigger and forward trigger is 15 GeV at electromagnetic scale.

- Exactly one good primary vertex in the event. A vertex is defined as good vertex if it has at least 5 associated tracks and the absolute value of z-coordinate of that vertex is less than 150 mm. The cut is used to reject cosmic and non-collision background.

- $\Delta\phi(\text{jet}^{\text{probe}}, \text{jet}^{\text{ref}}) > 2.6$. If there are more than two jets in the event, $p_T^{\text{third jet}} < 0.25 \times p_T^{avg}$.

The cuts have to minimize the effects of third jet radiation which will break the di-jet balance. The last cut is used to select good di-jet events.

The relative jet response can be biased by the dead optical transmitters (OTx) module regions as shown in Table 3.1. Those regions have to be removed from the analysis. Fig. 3.5 shows the di-jet relative response without optical transmitters removal and Fig. 3.6 shows the di-jet relative response after removing dead optical transmitters regions. From the plots, one can see the dead optical transmitters do have some effects on the relative response. In the central region, the relative response is almost flat. But in forward region, the relative response has a large uncertainty.

EtaMin	EtaMax	PhiMin	PhiMax
-2.7	-2.3	-2.55	-1.4
-2.4	-2.2	-1.2	-0.6
-2.3	-2.1	-0.2	0.05
-2.2	-1.6	1.3	2.2
-1.5	-1.3	-1.8	-1.2
-0.9	-0.3	2.3	3.0
-0.4	0.2	0.5	0.9
-0.2	0.1	-1.8	-1.2
-0.2	0.1	2.5	3.1
0.2	0.4	1.0	1.5
1.1	1.4	2.1	2.9
1.3	1.5	0.3	0.6
1.9	2.3	-1.4	-0.6
2.2	2.4	-2.5	-1.8
2.0	2.6	2.5	3.2
2.0	2.6	-3.2	-2.7

Table 3.1 Dead optical transmitters regions in calorimeter.

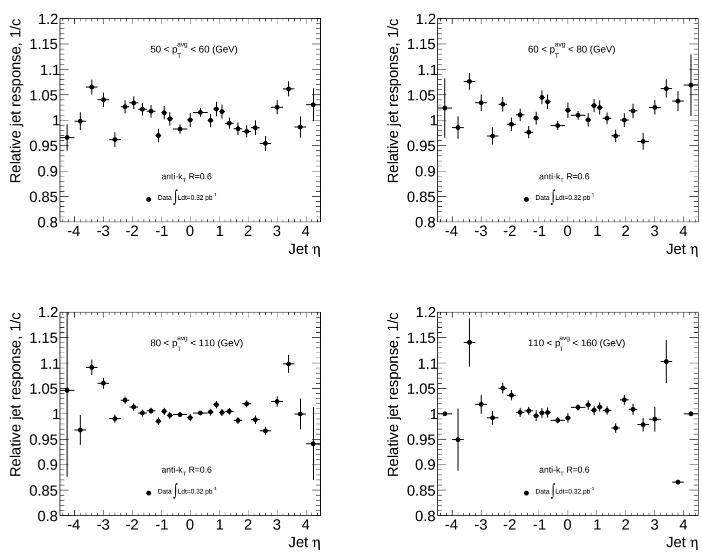

Figure 3.5 Relative response before optical transmitters correction for anti-k_t R=0.6 topocluster jets.

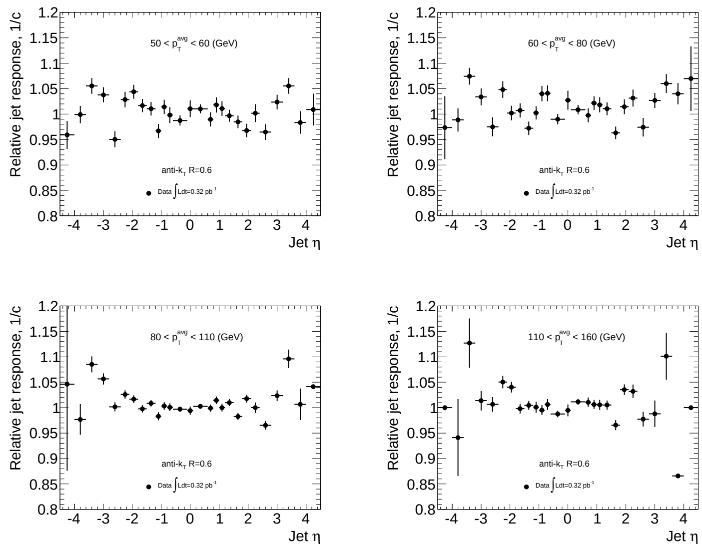

Figure 3.6 Relative response after optical transmitters correction (Table 3.1) for anti-k_t R=0.6 topocluster jets.

3.4 Measurement of Inclusive Jet Cross Section

The inclusive jet cross section is measured with proton-proton collisions at a center-of-mass energy $\sqrt{s} = 7$ TeV at a function of jet p_T and η. The data corresponds an intergrated luminosity of 17 nb^{-1}. The jet p_T spectrum is unfolded to physics jet level to compare with theoretical predictions. The theoretical predictions used in this analysis are given by NLOJET++ [32]. The unfolding is done using a bin-by-bin unfolding method. The unfolding factors are evaluated using Monte Carlo sample as show in Fig. 3.7. The systematic uncertainty on the unfolding factors includes jet energy scale and jet energy resolution. The final results on the jet cross section are shown in Fig. 3.8.

The measured jet cross sections are compared to NLO perturbative QCD calculations. The uncertainties from the NLO calculation are including PDF uncertainties, factorization and normalization scales and strong coupling constant α_S. The NLO calculations can only give parton level cross sections. In order to have particle level jet cross section predictions, the ratio of the cross sections with and without hadronization and underlying events given by a leading-logarithmic parton shower generator, can be used to correct these effects.

The systematics for this measurement include luminosity uncertainty, unfolding uncertainty and jet energy scale uncertainty. The luminosity uncertainty is about 11%. The uncertainly due to jet energy scale is the dominant systematics (about 30% to 40%). The unfolding uncertainty comes mostly from the jet energy resolution and the unfolding method.

A Singular Value Decomposition (SVD) unfolding method is described in Appendix A.

3.5 Di-Jet Resonance Search

There are several extentions beyond the Standard Model which predicts new particles with heavy mass. The heavy new particles may decay to two high p_T jets. The background to this new signal is only QCD di-jet events which can be predicted by Standard Model. The observation of any enhancement in the di-jet invariant mass spectrum would be a hint to the new physics.

ATLAS has already published an excited quark q^* analysis [33, 34]. Many colored resonance models have been overviewed by [35], in which both q^* resonance and color-octet scalars are introduced. Color-octet scalars were not included by ATLAS Monte Carlo production before. That is one of the reasons why it is interesting to implement the color-octet scalars analysis in ATLAS. The first step is to implement the color-octet Monte Carlo in ATLAS computing framework.

The procedure to include color-octet model is illustrated in Fig. 3.9. The Les Houches Events file (LHE) files are provided by the authors [35]. MADGRAPH 5 [36] is used to generate the parton level events at leading-order approximation. PYTHIA with CTEQ6L1 PDF is used in the event generation using ATLAS MC09 [37] tune. The events are processed by detector simulation with GEANT4 [31].

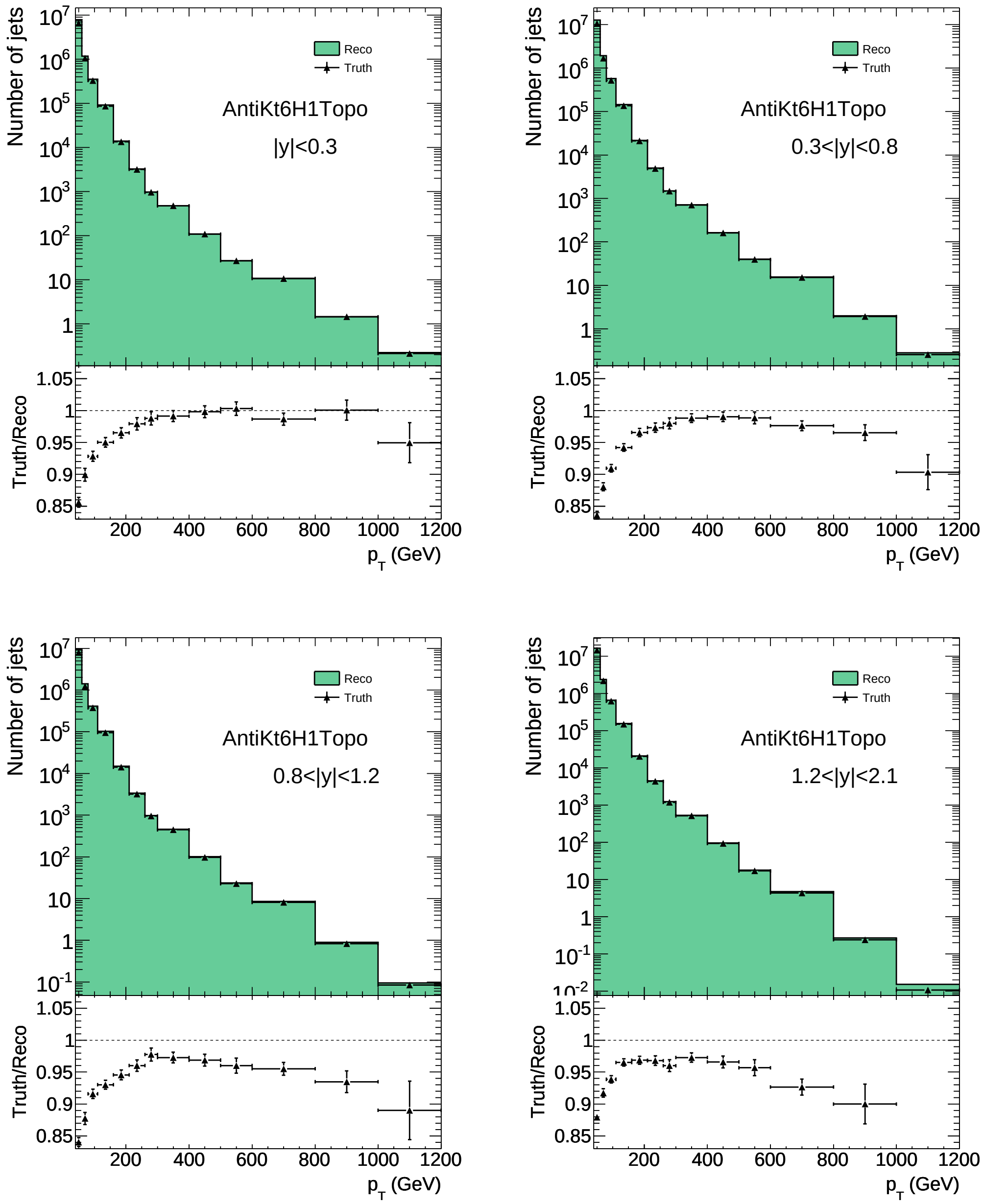

Figure 3.7 Distributions of the jet p_T in detector level and generator level in Monte Carlo sample for different rapidity bins. The ratio shown at the bottom of each plot represents the bin-by-bin unfolding factors.

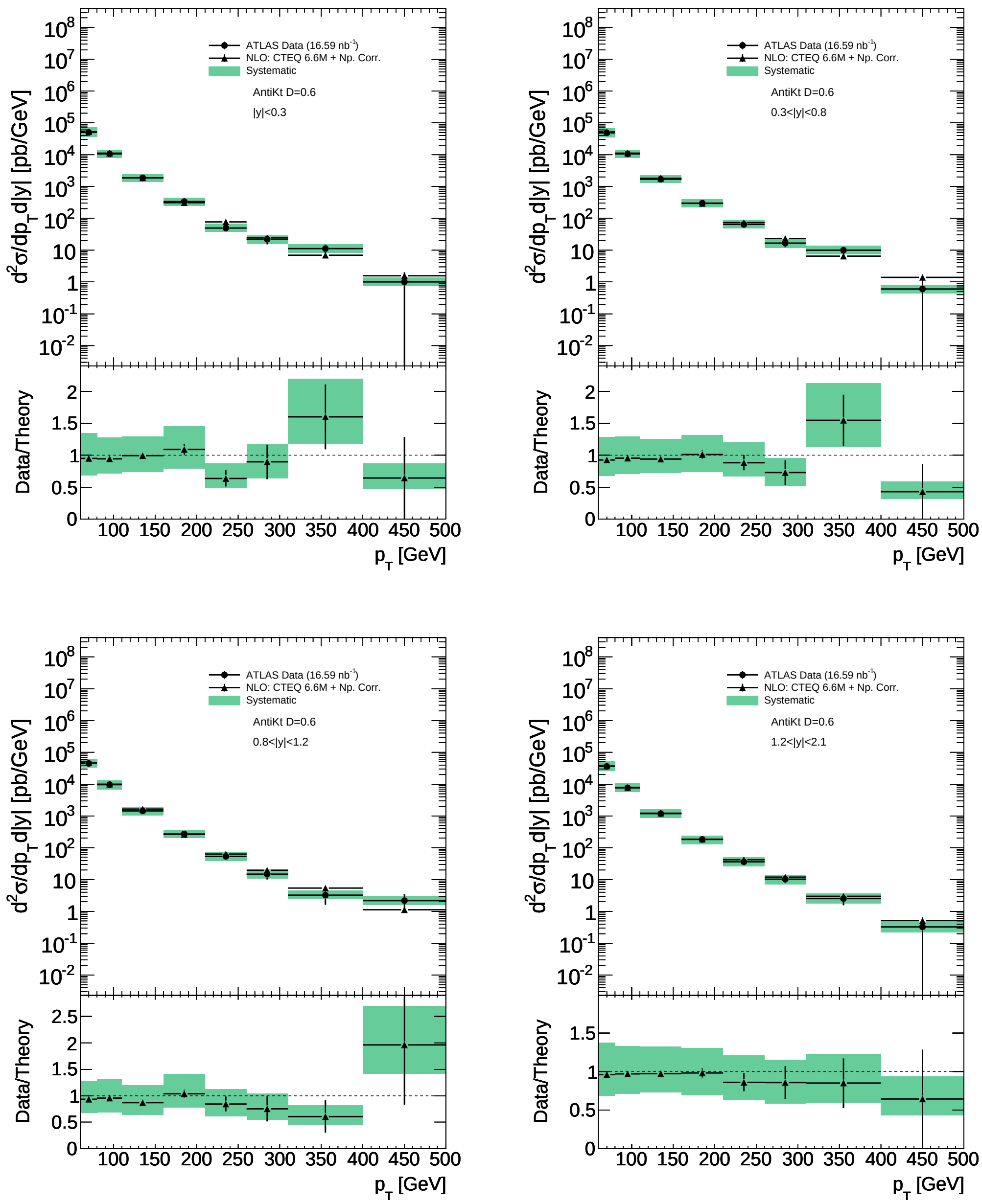

Figure 3.8 Final results for inclusive jet cross section measurement as a function jet p_T and η using integrated luminosity 16.59 nb^{-1} in $\sqrt{s} = 7$ TeV proton-proton collisions.

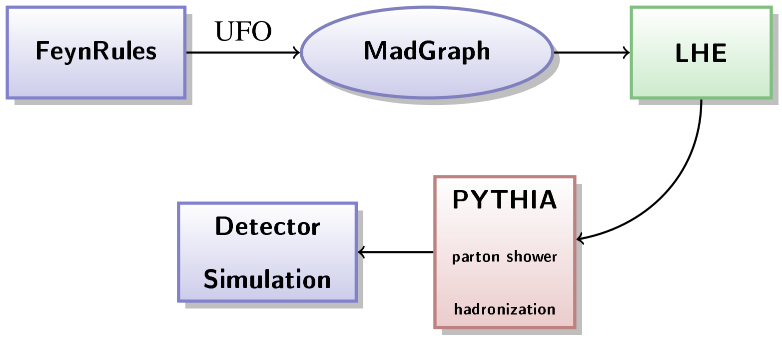

Figure 3.9 Generation of octet scalar Monte Carlo. Note that **UFO** stands for Universal FeynRules Output and **LHE** stands for Les Houches Events file.

q^*	$M_{q^*} = 1TeV$	$\Lambda_{q^*} = 2TeV$	0.156 nb	`MC10 PYTHIA`
New q^*	$M_{q^*} = 1TeV$	$\Lambda_{q^*} = 2TeV$	0.153 nb	`MadGraph 5`
q^*	$M_{q^*} = 1.5TeV$	$\Lambda_{q^*} = 3TeV$	0.0118 nb	`MC10 PYTHIA`
New q^*	$M_{q^*} = 1.5TeV$	$\Lambda_{q^*} = 3TeV$	0.0120 nb	`MadGraph 5`
q^*	$M_{q^*} = 2TeV$	$\Lambda_{q^*} = 4TeV$	0.00127 nb	`MC10 PYTHIA`
New q^*	$M_{q^*} = 2TeV$	$\Lambda_{q^*} = 4TeV$	0.00136 nb	`MadGraph 5`

Table 3.2 Cross section comparison for the two q^* approaches.

3.5.1 Validation

The procedure described in Fig. 3.9 is technically complicated and a very detailed and robust validation procedure is of extreme importance. Since the q^* model is already implemented in ATLAS computing framework, one way to perform validation is to produce q^* Monte Carlo samples using the procedure in Fig. 3.9. The Lagrangian for q^* is,

$$\mathscr{L}_{qgF} = \frac{g_s}{\Lambda} F^{A,\mu\nu} \left[\bar{u}\bar{K}_{N_D,A}(\lambda_L^U P_L + \lambda_R^U P_R)\sigma_{\mu\nu}u^*_{N_D} + \bar{d}\bar{K}_{N_D,A}(\lambda_L^D P_L + \lambda_R^D P_R)\sigma_{\mu\nu}d^*_{N_D}\right] + \text{h.c.}, \quad (3.7)$$

where Λ is the new physics scale, g_s is the strong coupling, $F^{A,\mu\nu}$ is the gluon field strength tensor with the adjoint color index $A = 1,...,8$, $\bar{K}_A$ are $3 \times N_D$ matrices of Clebsch-Gordan coefficients connecting the color indices of the different representations. The new physics scale Λ is at least $M_{q_j^*}$ or higher. In a strongly interacting theory, we expect that the strength of the couplings $\lambda^U_{L,R}$ and $\lambda^D_{L,R}$ should be typically of the order of unity. The cross sections for different mass points are list in Table 3.2. There is a small difference due to the different PDFs used in the generator because ATLAS q^* is using PYTHIA with MRST PDF while MADGRAPH is using CTEQ6L1 PDF. The Table 3.2 provides good validation for the Monte Carlo generation procedure.

In order to validate the kinematics of new Monte Carlo generation, the kinematics distributions from ATLAS q^* MC samples and new generation are overlaid in Fig. 3.10 with very good agreement.

3.5.2 Color-octet Scalars

A color-octet scalar can be produced via gluon-gluon initial states. Since the parton luminosity for gluon is very large at LHC, the color-octet scalar can have a very high cross section. One possible interaction is

$$\mathscr{L}_{gg8} = g_s d^{ABC} \frac{\kappa_S}{\Lambda_S} S_8^A F^B_{\mu\nu} F^{C,\mu\nu}, \tag{3.8}$$

where S_8 is a scalar octet. The couplings κ_S is assumed to be of the order of unity. Λ_S is defined as the mass of resonance. The Feynman diagrams of s_8 production are shown in Fig. 3.11. The cross sections for different mass points are shown in Table 3.3. Compared with the q^* cross section, the cross section of octet scalar is only a factor of 2 smaller.

The generator level kinematics distributions from q^* and color-octet scalar are overlaid in Fig. 3.12. The di-jet invariant mass (M_{jj}) distributions are quite different between q^* and color-octet scalar which has a wider M_{jj} distribution. The p_T distribution for color-octet scalar is more smooth compared with q^*. The jet multiplicity distribution is also very interesting because the

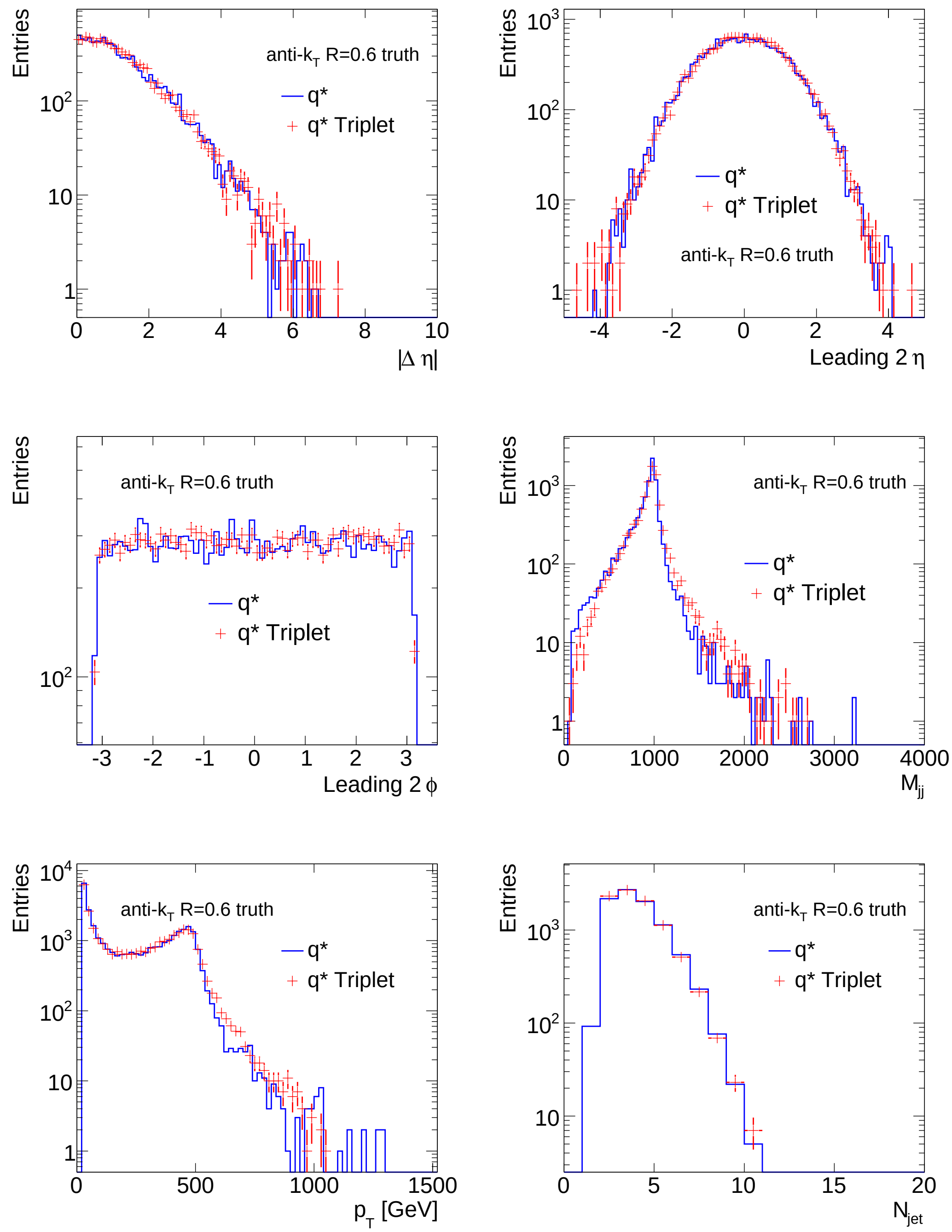

Figure 3.10 Validation plots for excited quark q^* samples with MADGRAPH and with PYTHIA.

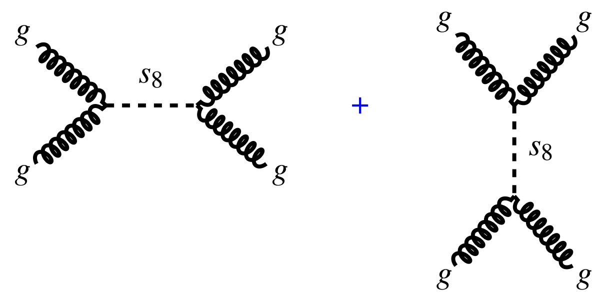

Figure 3.11 Feynman disgrams for color-octet scalars.

Mass [TeV]	Width [GeV]	$\sigma(s_8)$ [pb]	$\sigma\ (q^*)$ [pb]
1.0	157.0	83.796	156.0
1.3	197.9	12.28	-
1.5	224.8	3.918	11.8
1.7	251.3	1.35	-
2.0	290.5	0.306	1.27
2.5	354.8	0.032446	-
3.0	417.8	0.44656E-02	-
3.5	479.9	0.82653E-03	-
4.0	541.2	0.20851E-03	-

Table 3.3 Cross section of color-octet scalars and excited quark in $\sqrt{s} = 7$ TeV proton-proton collisions.

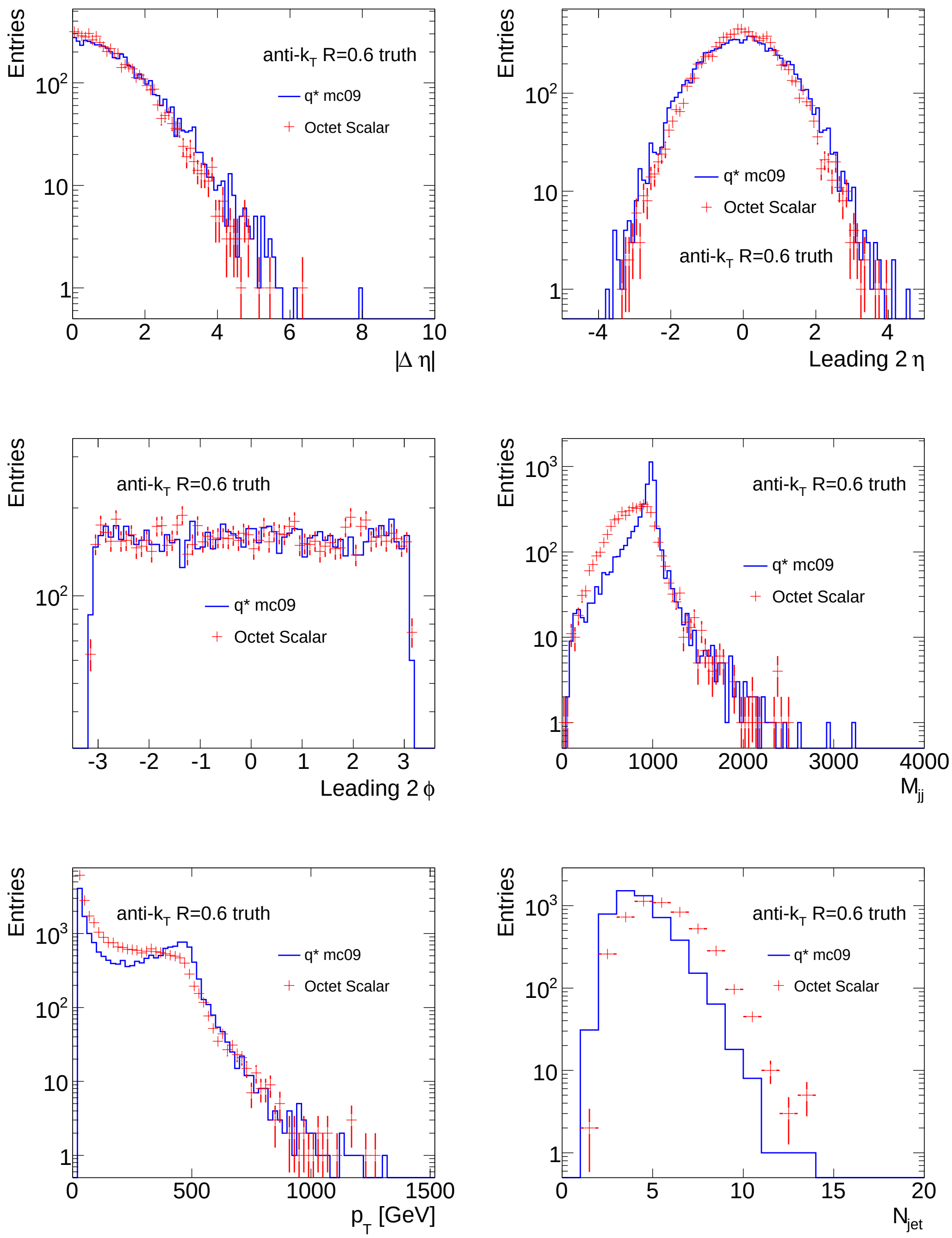

Figure 3.12 Generator level kinematics distributions for color-octet scalars.

color-octet scalar will decay to two gluons. Therefore, the final jet multiplicity is typically larger than q^*. That means the color-octet scalar event will tend to have more jets in the final states.

3.5.3 Results for Color-octet Scalar Resonance

The color-octet scalar resonance search in ATLAS has been published recently [12]. The exclusion limits on color-octet scalar have been established for the first time in ATLAS. The observed limit for color-octet scalar is 1.92 TeV with 1 fb^{-1} data (Fig. 3.5.3).

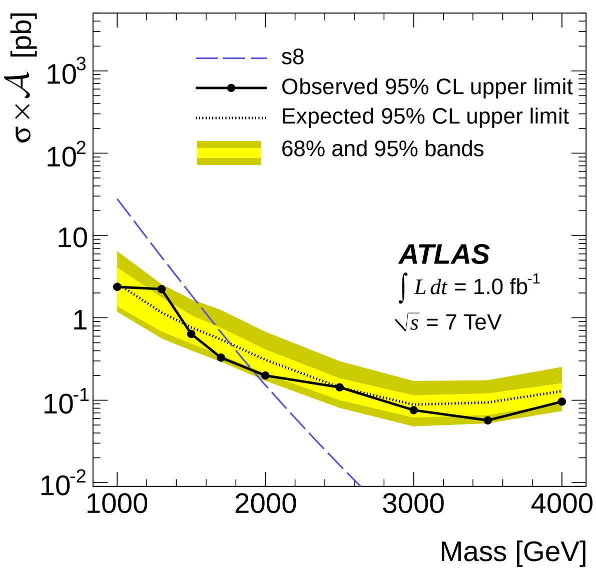

Figure 3.13 The 95% CL upper limits on $\sigma \times \mathscr{A}$ as a function of particle mass (black filled circles). The black dotted curve shows the 95% CL upper limit expected from Monte Carlo and the light and dark yellow shaded bands represent the 68% and 95% contours of the expected limit, respectively. Theoretical predictions for $\sigma \times \mathscr{A}$ for colour octet scalar resonances is in blue dashed line. For a given new physics model, the observed (expected) limit occurs at the crossing of its $\sigma \times \mathscr{A}$ curve with the observed (expected) 95% CL upper limit curve [12].

Chapter 4

Reconstruction of Objects

Reconstruction of physics objects is critical for all the analyses performed in ATLAS. The particles will only leave a limited amount of information in the detectors. The offline reconstruction software will take the raw data from detector and give physics objects information in a short time scale with high reconstruction efficiency and low fake rate. In this chapter, electrons, muons, missing transverse energy (MET) and *b*-jet reconstruction are reviewed. More information can be found in Ref. [17].

4.1 Electrons

The branching ratio of W boson to electron is about 11% [38]. It is crucial for this analysis to have a electron reconstruction with good performance in the full detector coverage. The electron reconstruction in ATLAS is using the combination of inner detector and calorimeter information [39]. The description of the ATLAS inner detector and calorimeter can be found in Sections 2.2.3 and 2.2.4. The electromagnetic (EM) calorimeter has four layers in the longitudinal direction which are called presample, η-strip, EM-Middle and EM-Back layers. Most of the EM shower energy will be deposited in the EM-Middle layer. The outmost layer, EM-Back, will be used to correct for very high energy EM showers. The transition region between the barrel and end-cap EM calorimeters, which is located at $1.37 < |\eta| < 1.52$, has worse performance compared with other regions. That is because there are more upstream materials in front of the EM calorimeter in this region. The inner detector covers the range $|\eta| < 2.5$, which provides high precision track measurement for electron reconstruction.

4.1.1 Electron Reconstruction Algorithm

The electron reconstruction starts with a set of seed clusters in the EM calorimeter. A sliding window algorithm is used to reconstruct the seed clusters using 3×5 cells in the EM-Middle layer (the size of cell is 0.025×0.025 in η, ϕ plane). Seed clusters will be matched to one or more tracks in inner detector within $|\eta| < 2.5$. In order to match the tracks to seed cluster, tracks are extrapolated from the last measurement point in the inner detector to the EM-Middle layer of calorimeter.

The matching is done by comparing the distance between tracks impact point and seed clusters using $\Delta R = \sqrt{\Delta\eta^2 + \Delta\phi^2}$. If the ΔR of track is below a certain threshold, the track will be considered. It is possible that more than one track is matched with the seed cluster. In that case, the track with smallest ΔR is considered as the best match. Due to the photon conversion contamination, tracks with silicon hits have high priority compared with tracks without silicon hits. Both converted photons and electrons will be kept in the electron container since both of them have tracks matching with clusters. But the converted photons can be removed by identification quality cuts.

The electromagnetic clusters will be recalculated using a 3×7 sliding window in EM-Middle layer in barrel region. In end-cap region, a 5×5 sliding window is used. The energy of electron is computed as a weighted average between the cluster energy and track momentum. The η, ϕ coordinates of the electron are computed using the information from tracks unless tracks have no silicon hits, in which case the η of the cluster is used.

4.1.2 Electron Identification and Efficiency

The electron identification can provide good separation between isolated electrons and fake electrons candidates using different identification (ID) variables which includes both calorimeter and tracker information. Three different sets of cuts are defined as shown in Table 4.1.

- The *loose* selection uses only calorimeter information. Shower shape variables from the second layer of EM calorimeter and the energy leakage into hadronic calorimeter are used in the selection.
- The *medium* selection uses a tighter track cluster matching, track quality and additional constraints on the shower shape information in the strip layer.
- The *tight* selection adds E/p, TRT information and b-layer hit requirements. The last cut is meant to reject converted photons.

The efficiency of electron ID is measured with the tag-and-probe method with W, Z and J/ψ as shown in Fig. 4.1. More detail about tag-and-probe method can be found in Ref. [1]. The difference in efficiency between data and Monte Carlo has to be corrected to obtain a properly description of data in physics analysis.

4.2 Muons

4.2.1 Muon Reconstruction

Muons are measured using the Inner Detector (ID) and in the Muon Spectrometer (MS) independently [13]. In this analysis, a `combined` `STACO` muon reconstruction algorithm is used.

For `Stand-alone` muon, the muon track is only from MS. For `combined` (CB) muon, track reconstruction is performed independently in the ID and MS. The algorithm combines the ID track

Type	Description	Name
Loose selection		
Acceptance	$\|\eta\| < 2.47$	
Hadronic leakage	Ratio of E_T in the first layer of the hadronic calorimeter to E_T of the EM cluster (used over the range $\|\eta\| < 0.8$ and $\|\eta\| > 1.37$)	R_{had1}
	Ratio of E_T in the hadronic calorimeter to E_T of the EM cluster (used over the range $\|\eta\| > 0.8$ and $\|\eta\| < 1.37$)	R_{had}
Middle layer of EM calorimeter	Ratio of the energy in 3×7 cells over the energy in 7×7 cells centred at the electron cluster position	R_η
	Lateral width of the shower	$w_{\eta 2}$
Medium selection (includes loose)		
Strip layer of EM calorimeter	Total shower width	w_{stot}
	Ratio of the energy difference between the largest and second largest energy deposits in the cluster over the sum of these energies	E_{ratio}
Track quality	Number of hits in the pixel detector (≥ 1)	n_{pixel}
	Number of total hits in the pixel and SCT detectors (≥ 7)	n_{Si}
	Transverse impact parameter ($\|d_0\|$ <5 mm)	d_0
Track–cluster matching	$\Delta\eta$ between the cluster position in the strip layer and the extrapolated track ($\|\Delta\eta\| < 0.01$)	$\Delta\eta$
Tight selection (includes medium)		
Track–cluster matching	$\Delta\phi$ between the cluster position in the middle layer and the extrapolated track ($\|\Delta\phi\| < 0.02$)	$\Delta\phi$
	Ratio of the cluster energy to the track momentum	E/p
	Tighter $\Delta\eta$ requirement ($\|\Delta\eta\| < 0.005$)	$\Delta\eta$
Track quality	Tighter transverse impact parameter requirement ($\|d_0\|$ <1 mm)	d_0
TRT	Total number of hits in the TRT	n_{TRT}
	Ratio of the number of high-threshold hits to the total number of hits in the TRT	f_{HT}
Conversions	Number of hits in the b-layer (≥ 1)	n_{BL}
	Veto electron candidates matched to reconstructed photon conversions	

Table 4.1 Definition of variables used for *loose*, *medium* and *tight* electron identification cuts for the central region of the detector with $|\eta| < 2.47$ [1].

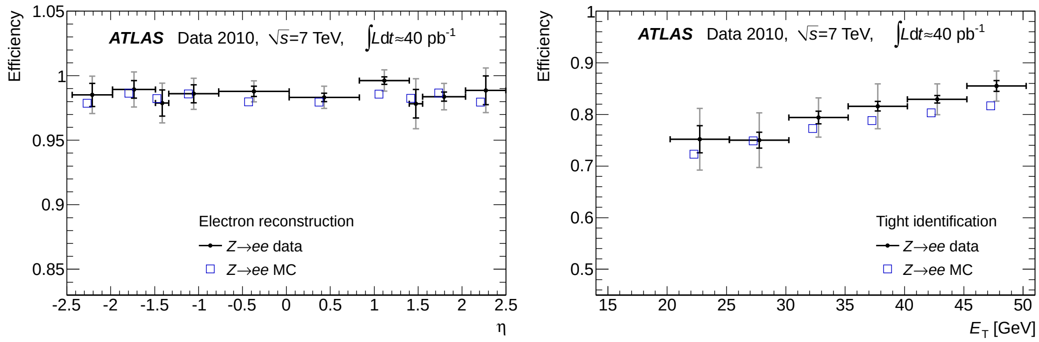

Figure 4.1 Left : Electron reconstruction efficiency in data and Monte Carlo as a function of η. Right : Electron *tight* ID efficiency in data and Monte Carlo as a function of η [1].

and MS track to get a final muon track. The CB muons have high purity. But only the track reconstruction in MS affects the muon reconstruction efficiency. That reconstruction efficiency varies at different η region. The efficiency in the $\eta \sim 0$ region is lower because that region is only partially covered by muon chambers. The efficiency also drops at the transition region between barrel and end-caps at $|\eta| \sim 1.2$ due to the limited detector coverage. The final CB muon momentum is calculated as the weighted average of the ID and MS stand-alone momentum measurements.

4.2.2 Muon Reconstruction Efficiency

The efficiency of the muon reconstruction is measured with the tag-and-probe method. This method is using $Z \to \mu\mu$ sample which can be selected by requiring two opposite charged isolated tracks with a dimuon invariant mass near the mass of Z boson. The CB `STACO` reconstruction efficiency is shown in Fig. 4.2.

The measurement of muon momentum resolution in data and MC is presented in Ref. [40]. The difference between data and MC has to be corrected at the analysis level.

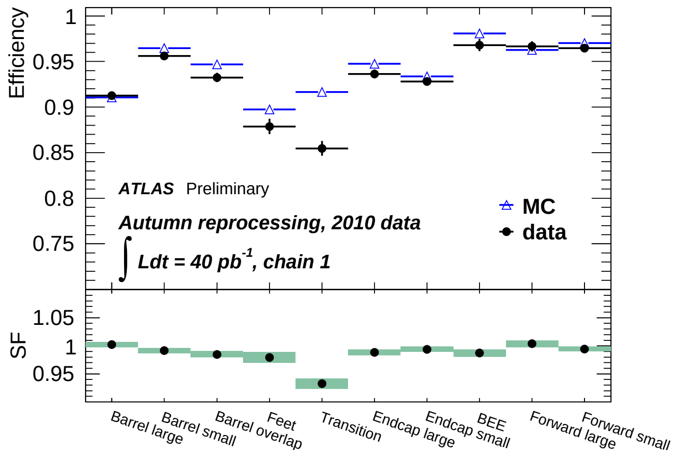

Figure 4.2 Reconstruction efficiencies and scale factors for CB `STACO` muons for different muon spectrometer regions [13].

4.3 Missing Transverse Momentum

The measurement of missing transverse momentum ($E_{\mathrm{T}}^{\mathrm{miss}}$) is very crucial for many analyses, like $H \to WW$ and $H \to \tau\tau$ in Higgs searches. The missing transverse momentum is the momentum imbalance in the transverse plane with respect to the beam axis. The $E_{\mathrm{T}}^{\mathrm{miss}}$ can come from the missing momentum from undetected particles, like $W \to l\nu$ events. The fake $E_{\mathrm{T}}^{\mathrm{miss}}$ comes from detector noise, dead material or mis-reconstruction of leptons or jets.

4.3.1 $E_{\mathrm{T}}^{\mathrm{miss}}$ Reconstruction

According to the different types of $E_{\mathrm{T}}^{\mathrm{miss}}$ definition, the $E_{\mathrm{T}}^{\mathrm{miss}}$ reconstruction [14] can use different detectors, like the calorimeter, muon detector and inner detectors. The $H \to WW$ analysis is using `MET RefFinal` which combines different physics objects. The x and y components of `MET RefFinal` is calculated like this:

$$E_{x(y)}^{miss} = E_{x(y)}^{miss,calo} + E_{x(y)}^{miss,\mu}, \tag{4.1}$$

where $E_{x(y)}^{miss,calo}$ is calorimeter term, $E_{x(y)}^{miss,\mu}$ is muon term. The magnitude of for $E_{\mathrm{T}}^{\mathrm{miss}}$ is calculated by:

$$E_T^{miss} = \sqrt{(E_x^{miss})^2 + (E_y^{miss})^2}. \tag{4.2}$$

The $E_{\mathrm{T}}^{\mathrm{miss}}$ calorimeter terms are calculated from the cells which are associated with any of the reconstructed physics objects in order of electrons, photons, hadronic τ, jets and muons. The cells which don't belong to any of these objects, contribute to the cell out term. Since the cell out term is very sensitive to the soft interactions in the calorimeter, it's very important to the $E_{\mathrm{T}}^{\mathrm{miss}}$ resolution.

The $E_{\mathrm{T}}^{\mathrm{miss}}$ calo term is calculated like,

$$E_{x(y)}^{miss,calo} = E_{x(y)}^{miss,e} + E_{x(y)}^{miss,\gamma} + E_{x(y)}^{miss,\tau} + E_{x(y)}^{miss,jets} + E_{x(y)}^{miss,softjets} + E_{x(y)}^{miss,calo,\mu} + E_{x(y)}^{miss,CellOut}, \tag{4.3}$$

The $E_{\mathrm{T}}^{\mathrm{miss}}$ muon term is calculated from muon objects. For the $|\eta| < 2.5$, combined muon is used to calculate the $E_{\mathrm{T}}^{\mathrm{miss}}$. In order not to double count the muon energy deposition in calorimeter, the term $E_{x(y)}^{miss,calo,\mu}$ is not added to the $E_{\mathrm{T}}^{\mathrm{miss}}$ calo term if the muon is an isolated muon. For the region $2.5 < |\eta| < 2.7$, only MS muon p_T is used.

4.3.2 $E_{\mathrm{T}}^{\mathrm{miss}}$ Objects Selection and Calibration

The selections and calibrations for different terms are following:

- $E_T^{miss,e}$ is calculated from *medium* default reconstruction electrons with $p_T > 10$ GeV.
- $E_T^{miss,\gamma}$ is calculated from EM scale *tight* γ with $p_T > 10$ GeV.
- $E_T^{miss,\tau}$ is calculated from *tight* local hadronic calibrated [41] (LCW) τ with a requirement $p_T > 10$ GeV.
- $E_T^{miss,softjets}$ is calculated from LCW anti-k_t jets (R=0.6) with $7 < p_T < 20$ GeV.
- $E_T^{miss,jets}$ is calculated from LCW anti-k_t jets (R=0.6) with $p_T > 20$ GeV.

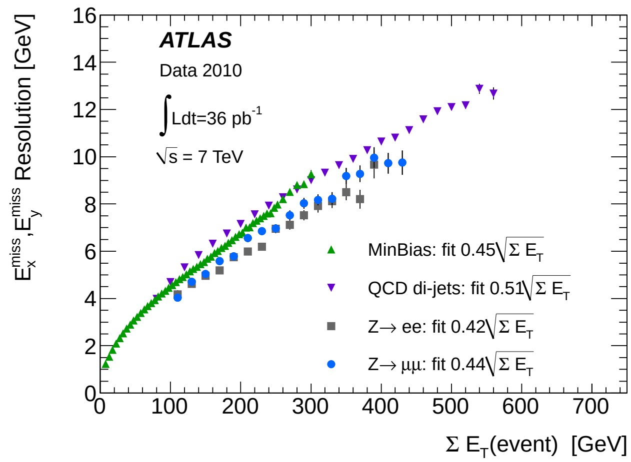

Figure 4.3 $E_{\mathrm{T}}^{\mathrm{miss}}$ resolution as a function of the total transverse energy in the event which is calculated by summing the p_T of muons and the total calorimeter transverse energy from $\sqrt{s} = 7$ TeV data [14].

- $E_T^{miss,CellOut}$ is calculated from topocluster which are not in any physics object. Topoclusters used in the calculation is using LCW calibration.

4.3.3 $E_{\mathrm{T}}^{\mathrm{miss}}$ Resolution

The $E_{\mathrm{T}}^{\mathrm{miss}}$ resolution can be obtained from $Z \to ll$ events in which no real $E_{\mathrm{T}}^{\mathrm{miss}}$ is expected. So the peak of (E_x^{miss}, E_y^{miss}) distributions should be at zero. The distributions are fitted by a Gaussian function. The width of the fitted function, σ, will give the value of $E_{\mathrm{T}}^{\mathrm{miss}}$ solution. Fig. 4.3 shows the $E_{\mathrm{T}}^{\mathrm{miss}}$ resolution for different samples.

4.4 *b*-jet Tagging

Jets which contains a B meson are known as *b*-jet. *b*-jet tagging is very important to the $H \to WW$ analysis because the $t\bar{t}$ events have to be rejected by tagging *b*-jets in the top quark decay. The most important feature to identify a B meson is the long lifetime of the hadrons containing a *b* quark. The average traveling distance in the transverse plane for a 50 GeV *b*-jet is about 3 mm. The background processes affecting the the *b*-tagging can come from long-live particles (K_s, Λ) decays and material interactions (photon conversions or hadronic interactions).

4.4.1 Track Selection

The track selection of the *b*-tagging algorithm is designed to reject fake tracks and tracks from other background processes. The p_T of tracks have to be larger than 1 GeV. The track transverse impact parameter d_0 is required to be less than 1 mm. The longitudinal impact parameter $z_0 \sin\theta$ has to be less than 1.5 mm. d_0 is the distance of closest approach of the track to the primary vertex point in the (r,ϕ) projection. z_0 is the z coordinate of the track at the point of closest approach in (r,ϕ) projection. Only the tracks with at least seven inner detector hits are selected. At least two hits are required to be on pixel detector with one of them on the innermost pixel layer.

All the tracks will be associated to jets. The association is done by a ΔR matching between the jet (η,ϕ) and track (η,ϕ). The ΔR requirement varies for different p_T of jet: for $p_T^{jet} = 20$ GeV, the ΔR is 0.45; for $p_T^{jet} = 150$ GeV, the ΔR is 0.25.

4.4.2 *b*-jet Tagging Algorithms

The `IP3D` algorithm is a kind of impact parameter-based *b*-tagging algorithm, which is combing the impact parameter significances of all the tracks in a jet. It is using the signed transverse impact parameter significance $d_0/\sigma(d_0)$ and the longitudinal impact parameter significance $z_0/\sigma(z_0)$ of track and taking into account the correlations between them. The $\sigma(d_0)$ ($\sigma(z_0)$) is width of fitted Gaussian distributions for d_0 (z_0).

The `JetFitter` is a inclusive secondary vertex reconstruction algorithm [42]. It exploits the topology of weak *b*- and *c*-hadron decays inside a jet. Fig. 4.4 shows the tagging weight for

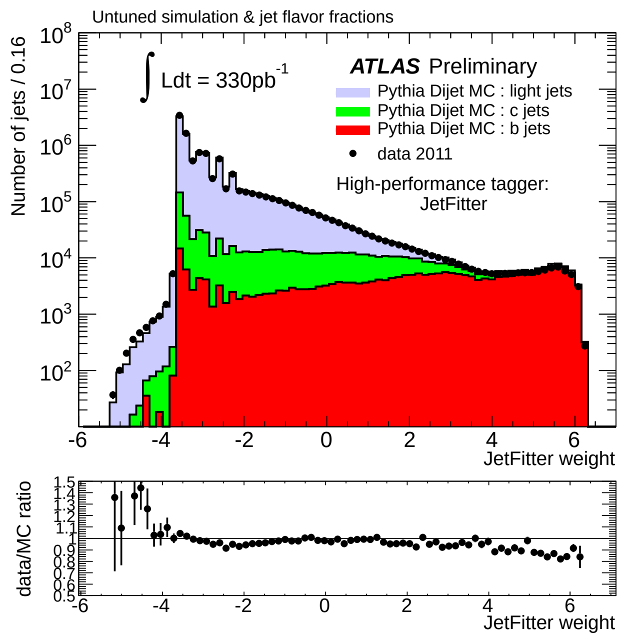

Figure 4.4 Distribution of the tagging rate for the JetFitter tagging algorithm at an operating point leading to 60% b-jet efficiency [15].

`JetFitter`.

Since both methods are using a likelihood ratio method, it is very easy to merge the two methods by summing their weights. The `JetFitter+IP3Ds` algorithm are combined by using a neural network technique. More information about high performance *b*-tagging algorithms in ATLAS can be found in Ref. [15]. In this analysis, `JetFitter+IP3D` is used.

Chapter 5

Higgs Boson Search

The search for the Standard Model (SM) Higgs is a major goal of LHC. The Higgs boson is predicted by Standard Model (SM) to give masses to gauge bosons and fermions. The Higgs production in hadron collider and decay are reviewed in Chapter. 1. In experiment, the analyses are usually categorized by the final states. From the branching ratio of SM Higgs in Fig. 1.9, Higgs to WW process has a large branching ratio in a wide Higgs mass range. The $H \to WW \to l\nu l\nu$ channel is particularly sensitive in the mass range of $120 < m_H < 240$ GeV which covers most of the range preferred by the global electroweak fit.

5.1 Signal Signature

All the SM Higgs production cross sections and branching ratios are taken from Ref. [8]. As shown in Fig. 1.7, there are ggF (top right), VBF (top left) and Higgs-strahlung (bottom right) processes.

- ggF (gluon gluon fusion, $gg \to H$) process has the highest cross section because the large gluon parton luminosity in proton-proton collisions. Next-to-next-to-leading order (NNLO) QCD calculation has been done for ggF process. The NNLO calculation increases the cross section by 25% [43]. This process is modeled by POWHEG [44, 45, 46]. The cross section of ggF process for $m_H = 125$ GeV is 0.35 pb at $\sqrt{s} = 7$ TeV.

- VBF (vector boson fusion, $qq' \to qq'H$) production process produces two quarks which will fragment into two jets in the final states. Most of the jets will be in forward region. This process is modeled by POWHEG. The cross section of VBF process for $m_H = 125$ GeV is 0.03 pb at $\sqrt{s} = 7$ TeV.

- WH/ZH (Higgs-strahlung) processes produce a vector boson in the final states. This process is modeled by PYTHIA. The cross section of WH (ZH) process for $m_H = 125$ GeV is 0.01 pb (0.01 pb) at $\sqrt{s} = 7$ TeV.

The NLO electroweak radiation correction is applied to ggF, VBF and WH/ZH processes. The Higgs boson decay branching ratios are calculated with HDECAY [47].

5.1.1 Higgs p_T Reweighting

The Higgs p_T spectrum of the ggF from POWHEG is reweighted to NLO fixed order calculation and NNLL resummation using `HqT2.0` [48, 49]. The reweighting will change the Higgs p_T spectrum, leptons p_T spectrum and number of jets distributions. So it is very important to apply this reweighting to get correction theoretical predictions for the Higgs signal kinematics. The truth Higgs p_T distribution and weighted Higgs p_T distribution from POWHEG are plotted in Fig. 5.1.

Technically the weights are calculated by the ratio of `HqT` output and truth Higgs p_T spectrum from Monte Carlo. The `HqT` package takes the input of MSTW2008nnlo [50] PDF as input.

The systematic uncertainties are obtained by varying PDF error, resummation scale, renormalization scale μ_R, and factorization scale μ_F.

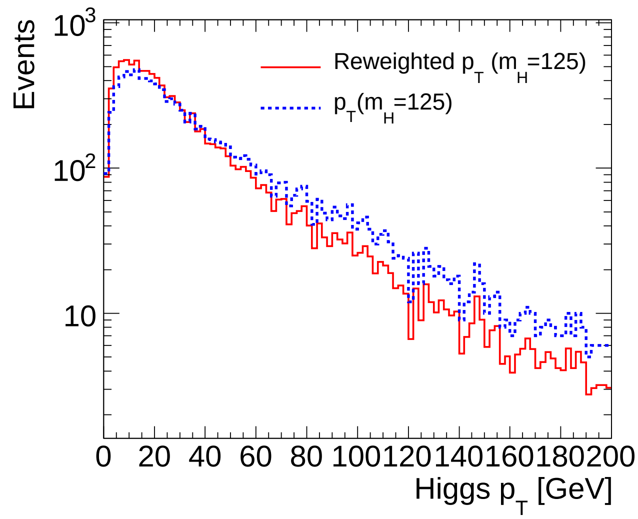

Figure 5.1 Truth Higgs p_T distribution and weighted Higgs p_T distribution from POWHEG.

5.1.2 Signal Extraction

The two leptons from the decay of W bosons will have spin correlation. Because the spin of Higgs boson is zero, the spin orientation of W bosons will be opposite to each other due to angular conservation. There are three spin configurations for the two W bosons as shown in Fig. 5.2. The W^+ will emit a neutrino opposite to its spin orientation. The W^- will emit a anti-neutrino in its spin orientation. Then the two neutrinos will have the same direction. The same is for the two leptons, which will make the two leptons fly in the same direction.

Since the two neutrinos can not be captured by detector, the mass of Higgs can not be fully reconstructed. In order to determine the mass of Higgs, a transverse mass definition has to reflect the mass of Higgs. One m_T definition is proposed in [51]. The m_T is defined,

$$m_T = \sqrt{(E_T^{ll} + E_T^{\nu\nu})^2 - (p_x^{ll} + p_x^{\nu\nu})^2 - (p_y^{ll} + p_y^{\nu\nu})^2}, \tag{5.1}$$

where E_T^{ll} is energy of di-lepton system, $E_T^{\nu\nu}$ is the final MET, p_x^{ll} (p_y^{ll}) is the x (y) component of

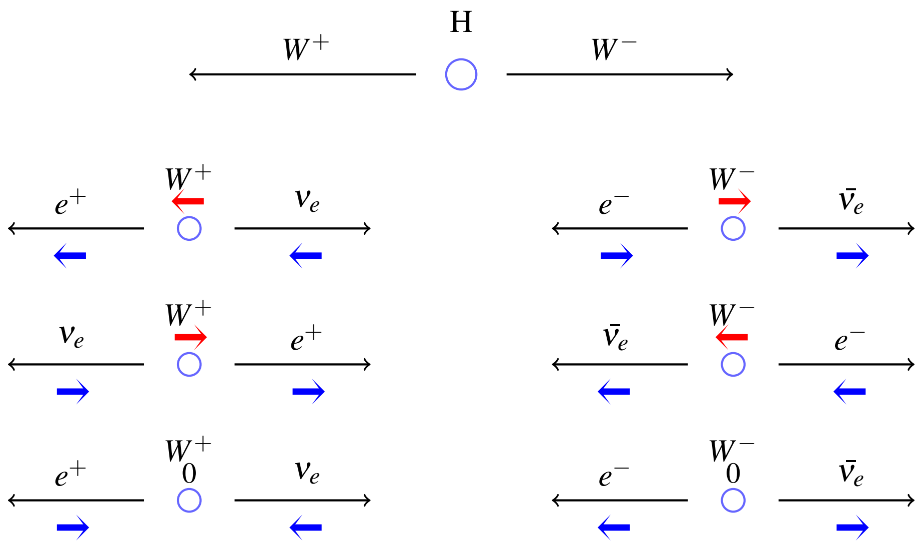

Figure 5.2 Spin correlation of Higgs to WW signal events.

the di-lepton momentum, $p_x^{\nu\nu}$ ($p_y^{\nu\nu}$) is the x (y) component of the MET.

5.2 Background Processes

Fig. 5.3 shows the SM cross section measurement in ATLAS at $\sqrt{s} = 7$ TeV. Most of $H \to WW$ background processes are in the plot. Most of the background processes have large cross sections. And the cross section of ggF signal at $m_H = 125$ GeV mass point is only 0.35 pb. If the contamination from background processes, like $W + jets$ or $Z + jets$, are too large in signal region, the signal will be washed out. So it's very important to keep the background under control.

- Standard Model (SM) WW background is the main (irreducible) background for $H \to WW$ analysis. The $qq/qg \to WW$ processes are modeled by MC@NLO [52]. $gg \to WW$ is a NLO process, which is simulated by `gg2WW` [53].

- $b\bar{t}$ background. For $t\bar{t}$ events, almost all the Top quark will decay to a W plus a b quark. If

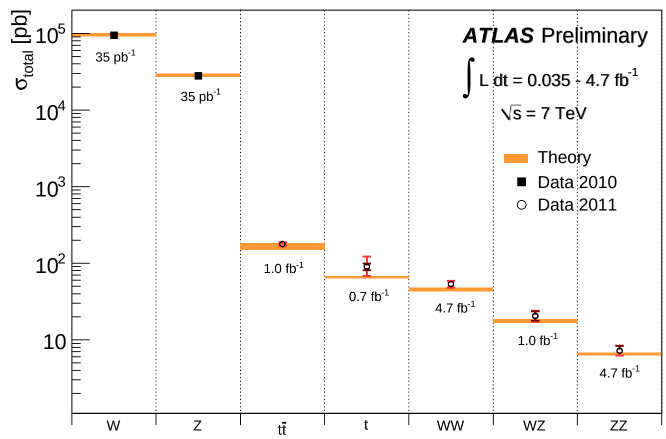

Figure 5.3 Summary of several Standard Model total production cross section measurements compared to the corresponding theoretical expectations [16].

the two b-jets are misidentified as light jets, $t\bar{t}$ events will be selected as signal events. $t\bar{t}$ is modeled by MC@NLO.

- Single Top. At the Wt channel of single Top process, a event will be treated as a signal event if the b-jet is misidentified as a light jet. AcerMC [54] is used to simulate the single Top events.

- Drell-Yan (γ^*, Υ, Z) background. In principle, Z events will not affect the signal region too much because the $E_{\mathrm{T}}^{\mathrm{miss}}$ and Z window cut (will be described in Section 5.6.1) will reject most of the Z events. But the low-mass Drell-Yan (DY) events will pass the final cuts if there is fake $E_{\mathrm{T}}^{\mathrm{miss}}$. The fake $E_{\mathrm{T}}^{\mathrm{miss}}$ is very sensitive to the soft interaction in a event, which is pile-up. So the pile-up description of Monte Carlo events is critical to the fake $E_{\mathrm{T}}^{\mathrm{miss}}$ description. And that is very important to the DY background rejection. DY background processes are modeled by ALPGEN [55].

- WZ/ZZ/Wγ/Wγ^* background. WZ is using MC@NLO. ZZ is modeled by SHERPA [56].

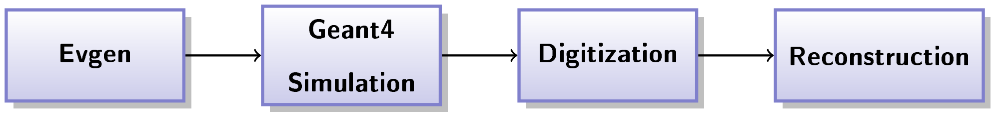

Figure 5.4 Monte Carlo production processes in ATLAS.

Wγ is very signal like in terms of m_T distribution if the γ can fake as an electron. Wγ is using ALPGEN. Wγ^* is using MADGRAPH [57].

- W+jets background. If one jet is misidentified as a lepton, the W+jets will pass the selection cuts. Even the fake factor (Eq. 6.4) is small, the huge cross section of W will lead to non-negligible W+jets contamination. W+jets is modeled by ALPGEN.

5.3 Detector Simulation and Reconstruction

As shown in Fig. 5.4, the Monte Carlo production in ATLAS has several steps. The first step is using generators to generate physics events. The format of the output is called `Evgen` file, which contains all the particles' information. The second step is GEANT4 [31] simulation. The GEANT4 simulation will simulate the interaction between the particles and detectors. The output of this step is called `HITS` file. The third step is `Digitization`. The output is `RDO` (Raw Data Outputs). The last step is `Reconstruction`. The output is `AOD` (Analysis Object Data).

5.3.1 Pile-up Simulation

Due to the high luminosity of LHC, several proton-proton interactions can happen in the same bunch crossing. The presence of additional interactions besides of hard interaction is called in-time pile-up effect. The detector will record the additional interactions with the hard interaction. So in the final events, both hard interaction and soft pile-up interactions will go to analysis. Because

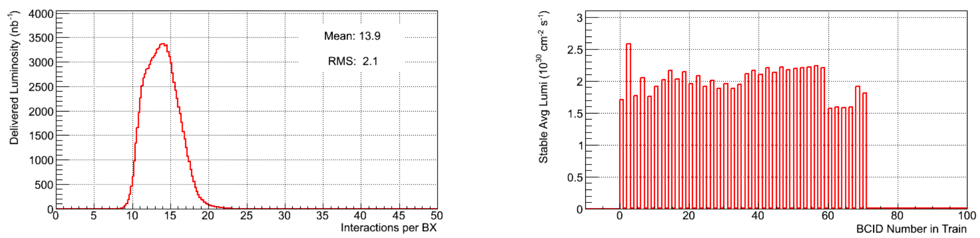

Figure 5.5 $<\mu>$ and BCID measured on October 23, 2011. Left: $<\mu>$. Right:BCIDs in a bunch train.

the time interval between the two bunches is 50 ns in most of 2011 data, the next will come when the detectors are still recording the information of first bunch crossing. From the pulse shape of LAr in Fig. 2.7, one can see the typical readout time for LAr is about 800 ns. 16 bunch crossings will come before the signal of LAr returns to zero. This effect is called out-of-time pile-up. Both in-time and out-of-time pile-up effects are simulated by Monte Carlo.

The idea of Monte Carlo simulation for pile-up is to overlay one hard interaction event and several other soft interaction events into one event for both in-time and out-of-time pile-up. The procedure is done after GEANT4 simulation with the input of `HITS` file. For the out-of-time pile-up, a window of [-800 ns, 800 ns] is set. One terminology used here is $<\mu>$, which is the **average interactions per bunch crossing** over a Luminosity Block (LB) and over all colliding Bunch-Crossing Identifications (BCID). The duration of a LB is approximately two minutes, with begin and end times set by the ATLAS data acquisition system (DAQ) [25]. The left plot of Fig. 5.5 is showing the luminosity weighted average interactions per bunch crossing in data.

There are three types of events:

- Hard interactions events.

- Minimum Bias events : One has to decide how many Minimum Bias events to be added in

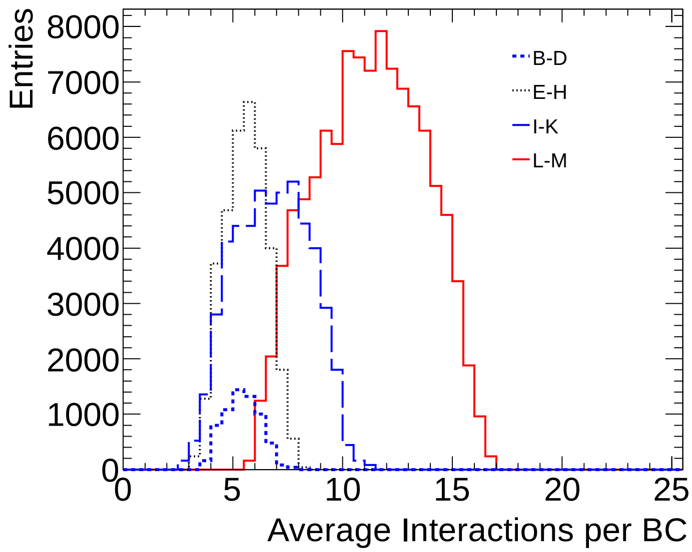

Figure 5.6 Average interactions per bunch crossing from Monte Carlo pile-up simulation.

the final event. N, the number of Minimum Bias events, is a random number taken from the Poisson distribution of $<\mu>$, where $<\mu>$ is a fixed input parameter. The parameter should be close to the data $<\mu>$.

- Cavern background events : Even after the collisions, a gas which are including some low energy neutrons and photons, are still in cavern. That is called "cavern background", which is very difficult to simulation. The number of cavern background events is constant, which is depending on $<\mu> \times$ fraction of colliding BCIDs.

The running conditions of LHC are always changing. That is why using only single $<\mu>$ value to do simulation is not enough. ATLAS produces four types of Monte Carlo samples which are corresponding different data taking periods as show in Fig. 5.6.

Period	$\mu\mu$	ee	$e\mu$
B - I	mu18_MG	e20_medium	mu18_MG $\|$ e20_medium
J	mu18_MG_medium	e20_medium	mu18_MG_medium $\|$ e20_medium
K	mu18_MG_medium	e22_medium	mu18_MG_medium $\|$ e22_medium
L - M	mu18_MG_medium	e22vh_medium1	mu18_MG_medium $\|$ e22vh_medium1

Table 5.1 Triggers used in data and MC.

$<\mu>$ **Reweighting**

The pile-up simulation can not be perfect to describe the $<\mu>$ in data. The weight on $<\mu>$ is the ratio of data $<\mu>$ distributions and the MC $<\mu>$ distributions. The weight will be applied to Monte Carlo events.

5.4 Trigger

The basic feature of $H \to WW$ is the presence of two high p_T leptons and large $E_{\mathrm{T}}^{\mathrm{miss}}$. The candidates events should be triggered by single lepton triggers. Table 5.1 shows the list of triggers used in each data taking periods. In both ee and $\mu\mu$ channels, a primary single lepton trigger is used. in $e\mu$ channel, the or of the electron and muon primary triggers is used. Due to the increasing of instant luminosity in different periods, the trigger thresholds for primary single lepton have been gradually tightened.

5.4.1 Electron Trigger

For electron triggers, `EF_e20_medium`, `EF_e22_medium` and `EF_e22vh_medium1` are used in the analysis. The numbers after `EF_e` in the names represent the nominal p_T threshold values for these triggers. medium, medium1 indicate the electron identification selection criteria and vh means that the trigger has both η dependent p_T threshold and hadronic leakage cut in Level 1.

Efficiencies for these triggers in both data and Monte Carlo are estimated using tag and probe method with $Z \to ee$ events. Monte Carlo trigger efficiencies are measured using the same method for data. The difference between data and Monte Carlo is corrected using scale factors which are calculated as,

$$\text{electron SF} = (\text{electron efficiency in data}) / (\text{electron efficiency in Monte Carlo}). \tag{5.2}$$

Scale factors will be applied to MC to correct the data MC difference.

5.4.2 Muon Trigger

The single muon triggers used in this analysis are EF_mu18_MG and EF_mu18_MG_medium. The nominal p_{T} threshold for these triggers are set to 18 GeV. The suffix medium indicates the difference in the L1 trigger threshold which was tightened from L1_MU10 to L1_MU11 in barrel region.

Muon trigger efficiency are estimated using tag and probe method with $Z \to \mu\mu$ events. In the measurement, the selection criteria for muons are the identical as the one used in the analysis. The following selection are applied on tag and probe pairs.

- $|M_{\mu\mu} - M_Z| < 10$ GeV
- $\Delta\phi_{\mu\mu} > 2.0$

In the estimation, tag muons are required to match a trigger object in interest. The matching ΔR for the estimation is set to 0.20. The estimation is done both in data and Monte Carlo. In the Monte Carlo estimation, the differences in muon reconstruction efficiency and momentum resolution from data are corrected.

5.4.3 Event Based Trigger Application

In order to compensate the difference in trigger efficiency in data and MC, trigger matching is done for leading and sub-leading p_T leptons on plateau. The definition of plateau is $p_{\mathrm{T}} > 21$ GeV for `EF_e20_medium`, $p_{\mathrm{T}} > 23$ GeV for `EF_e22_medium` and `EF_e22_medium1` and $p_{\mathrm{T}} > 20$ GeV for muon triggers. Trigger matching methods are identical as the one used in the per lepton efficiency estimations. If both leading and sub-leading offline lepton fail trigger matching, the event is rejected. Because the trigger selection is changing even in the same MC period, a luminosity weight has to be applied into MC events to simulate the data triggers. The weight is calculated according to which trigger the event passed, and integrated luminosity of that data taking period in which that trigger is used. The event scale factor is calculated as

$$\text{event SF} \;=\; \left[1-\left(1-\varepsilon_{MC}^{lead}\times SF^{lead}\right)\times\left(1-\varepsilon_{MC}^{sub}\times SF^{sub}\right)\right] / \left[1-\left(1-\varepsilon_{MC}^{lead}\right)\times\left(1-\varepsilon_{MC}^{sub}\right)\right],$$

where ε_{MC}^{lead}, ε_{MC}^{sub} are per lepton trigger efficiencies for leading and sub-leading leptons, and SF^{lead}, SF^{sub} are per lepton scale factors for leading and sub-leading leptons.

5.5 Objects Selection

5.5.1 Electrons

The electrons selected by this analysis are reconstructed by the ATLAS reconstruction software. A detailed electron reconstruction is described in Section 4.1. `Tight` electron identification selection cuts are applied. On top of that, this analysis uses several other cuts to reject background. The p_T of electron is bigger than 15 GeV to make sure that electron has high reconstruction efficiency and systematic can be understood. A geometrical acceptance ($|\eta_{\mathrm{cluster}}| < 2.47$) has to be applied because electron is reconstructed using track and calorimeter cluster matching and the inner detector has limited η coverage. To insure good energy and position precision, only candidates lying outside the transition region between the barrel and the endcap parts of the calorimeter ($|\eta| < 1.37$ or $|\eta| > 1.52$) are selected. In the data taking periods E to H, there was a LAr electronics front-end failure which affects $\sim 17\%$ data taken. That failure is fully simulated in Monte Carlo sample. A set of impact parameter cuts ($|z_0| < 1$ mm and $|\frac{d_0}{\sigma(d_0)}| < 10$) are applied to rejected fake electrons. To selected isolated electron candidates, a track isolation ($\frac{\text{pTcone30}}{p_T} = \frac{\Sigma(p_{\text{T}}^{\text{track}})}{p_T} < 0.13$) and calorimeter isolation ($\frac{\text{ETconecorr30}}{p_T} = \frac{\Sigma(E_{\text{T}}^{\text{cells}})}{p_T} < 0.14$) cuts are used. `pTcone30` is the $\sum p_T$ of inner detector tracks around the electron track in a crone of $\Delta R < 0.3$ in (η,ϕ) plane. `ETconecorr30` is the sum of energy in calorimeter in a cone of $\Delta R < 0.3$ with pile-up dependent correction [58].

5.5.2 Muons

Muons are reconstructed using an official muon reconstruction algorithm which is described in Section 4.2. Muon track selection is used to reduce mis-tag rate of muon and improve on the muon momentum resolution. Muons tracks are required to have at least two hits in the pixel detector and have 6 hits in SCT detector. Tracks are rejected if they have more than two holes[1] in the SCT and pixel detectors. For TRT detector, the sum of the hits on track and outliers is defined as n, where outliers is a set of nearby TRT hits when the track fit quality is bad. If the $|\eta| < 1.9$, the requirement is $n > 5$ and $n_{\text{TRT}}^{\text{outliers}} < 0.9n$. If the $|\eta| > 1.9$ and $n > 5$, the requirement is $n_{\text{TRT}}^{\text{outliers}} < 0.9n$. Kinematic cuts of $p_{\text{T}} > 15$ GeV an $|\eta| < 2.4$ are also applied. On the top of that, impact parameter cuts of $|z_0| < 1$ mm and $|\frac{d_0}{\sigma(d_0)}| < 3$ are applied. The muon isolation is using tracking ($\frac{\text{pTcone30}}{p_T} = \frac{\Sigma(p_{\text{T}}^{\text{track}})}{p_T} < 0.13$) selection and calorimeter ($\frac{\text{ETconecorr30}}{p_T} = \frac{\Sigma(E_{\text{T}}^{\text{cells}})}{p_T} < 0.14$) selection.

[1] A hole is defined as an absence of a hit when it is expected given the track trajectory.

5.5.3 Jet Selection

Jet reconstruction is described in Chapter 3. The jet is required to have $p_T > 25$ GeV and $|\eta| < 4.5$. The jet p_T threshold is raised to 30 GeV in the region $2.75 < |\eta| < 3.25$ which is the transition region between different calorimeters. That region is affected more by pile-up effects. In order to reject the pile-up jets in central region, jet vertex fraction (JVF) is defined. Each jet may match with several tracks. And those tracks can associate with different primary vertices. JVF is defined as,

$$\text{JVF}(jet, vtx) = \frac{\sum p_T(trk)\, if\, vtx \in track.vtx}{\sum p_T(trk)}. \tag{5.3}$$

JVF is a function of jet and vertex. Given a jet and a reference vertex, the numerator of JVF is the sum p_T of the tracks which are matched to this jet and associated to this vertex. The denominator of JVF is the sum p_T of the tracks which are matched to this jet. The cut on JVF is $|\text{JVF}| > 0.75$ which is proposed in [59]. Hard jets will have higher probability to pass this cut.

5.5.4 Event Cleaning

The jets in the proton-proton collisions can come from some backgrounds, like cosmic ray muons, large calorimeter noise. If one event has some background jets, the event topology will change. That event has to be rejected by the analysis if the fake jet is not overlapped with electrons or muons. This is called event cleaning. The *looser* cleaning definitions used in this analysis, are list in Table. 5.2.

The types of selections are :

- Noise cell in the hadronic endcap calorimeter (HEC). Because single cell contributes most of the energy of the jet, the jet energy fraction in HEC (f_{HEC}) is large. The signal shape quality in HEC ($f_{\text{HECquality}}$) is also very poor.
- Rare coherent noise in the EM calorimeter. Some fake jets have a large EM fraction (f_{EM})

	Looser
HEC spikes	($f_{\texttt{HEC}} > 0.5$ and $\lvert f_{\texttt{HEC}\,\text{quality}}\rvert > 0.5$ and $\bar{f}_{\text{quality}} > 0.8$) or $\lvert E_{\text{neg}}\rvert > 60$ GeV
Coherent EM noise	$f_{\text{EM}} > 0.95$ and $f_{\text{quality}} > 0.8$ and $\bar{f}_{\text{quality}} > 0.8$ and $\lvert\eta\rvert < 2.8$
Non-collision background	($f_{\text{EM}} < 0.05$ and $f_{\text{ch}} < 0.05$ and $\lvert\eta\rvert < 2$) or ($f_{\text{EM}} < 0.05$ and $\lvert\eta\rvert \geq 2$) or ($f_{\text{max}} > 0.99$ and $\lvert\eta\rvert < 2$)

Table 5.2 Selection criteria used to reject fake jets and non-collision background.

which is defined as the ratio of the energy deposited in EM calorimeter to the total jet energy. And some cells have a poor signal shape quality (f_{quality}) .

- Cosmic or non-collision background. The jets can come from cosmic or other non-collision background. f_{EM} are required to be larger than some value to make sure there is some energy in EM calorimeter. The cut for jet charge fraction (f_{ch}), which is defined as the ratio of the scalar sum of the tracks p_T to the jet p_T, is applied. The maximum energy fraction in any single calorimeter layer (f_{max}) has to be less than some value.

5.6 Event Selection

5.6.1 Common Event Selection

This section will describe several selections which are common for 0-jet, 1-jet and 2-jet channels. Due to different background processes, the cuts will not be the same for different flavor combinations, which are ee, $e\mu$ and $\mu\mu$.

Events have to pass primary vertex selection which requires least one primary vertex associated with at least three tracks. This selection will reject cosmic or other non-collision background. Since it is $H \rightarrow WW^* \rightarrow l\nu l\nu$ analysis, the events are selected by requiring exactly two oppsite-sign leptons. Events which have three or more leptons will be rejected to reduce other background contamination. The leading lepton p_T , which is used to trigger the event, has to be bigger than 25 GeV and subleading lepton $p_T > 15$ GeV. The leading and subleading lepton p_T distributions are shown in Fig. 5.7.

The Drell-Yan events (γ^*, Υ, Z), which have two leptons in the final states, can pass the signal region selection if there is fake $E_{\mathrm{T}}^{\mathrm{miss}}$. Those events can be suppressed by appling di-lepton invariant mass (m_{ll}) cut. For ee, $\mu\mu$ channels, the lower bound on invariant mass is $m_{ll} > 12$ GeV to reduce γ^*, Υ events. For $e\mu$ channel, the cut is $m_{ll} > 10$ GeV. Most of the $Z \rightarrow ee$, $Z \rightarrow \mu\mu$ events will be rejected by $|m_{ll} - m_Z| < 15$ GeV. The m_{ll} distributions can be found in Fig. 5.8.

The QCD multijets and Drell-Yan events usually have feature of low $E_{\mathrm{T}}^{\mathrm{miss}}$. Those events will be reduced by an additional cut on $E_{\mathrm{T}}^{\mathrm{miss}}$. However, the mis-measurement on the lepton direction will create fake $E_{\mathrm{T}}^{\mathrm{miss}}$. The $E_{\mathrm{T,rel}}^{\mathrm{miss}}$ is defined as,

$$E_{\mathrm{T,rel}}^{\mathrm{miss}} = \begin{cases} E_{\mathrm{T}}^{\mathrm{miss}} & \text{if } \Delta\phi \geq \pi/2 \\ E_{\mathrm{T}}^{\mathrm{miss}} \cdot \sin\Delta\phi & \text{if } \Delta\phi < \pi/2 \end{cases}, \tag{5.4}$$

where $\Delta\phi$ is the absolute value of difference in the azimuthal angle ϕ between $E_{\mathrm{T}}^{\mathrm{miss}}$ and nearest lepton or jet. The selection is $E_{\mathrm{T,rel}}^{\mathrm{miss}} > 45$ GeV for ee, $\mu\mu$ channels. The cut on $e\mu$ channel is $E_{\mathrm{T,rel}}^{\mathrm{miss}} > 25$ because $e\mu$ channel is less affected by Drell-Yan events. $E_{\mathrm{T,rel}}^{\mathrm{miss}}$ distributions in Z control region are shown in Fig. 5.9. The jet multiplicity distributions after $E_{\mathrm{T,rel}}^{\mathrm{miss}}$ cut are shown in Fig. 5.10. The number of events until $E_{\mathrm{T,rel}}^{\mathrm{miss}}$ cut are shown in Table 5.3.

The events after $E_{\mathrm{T,rel}}^{\mathrm{miss}}$ cut will be separated into three categories which are 0-jet, 1-jet and 2-jet. The reason why it is necessary to have three categories is that the contributions from different backgrounds vary a lot in 0-jet, 1-jet and 2-jet events. For example, Drell-Yan contribution is the most important background in 0-jet events. Top contribution is larger in 1-jet channel. Therefore,

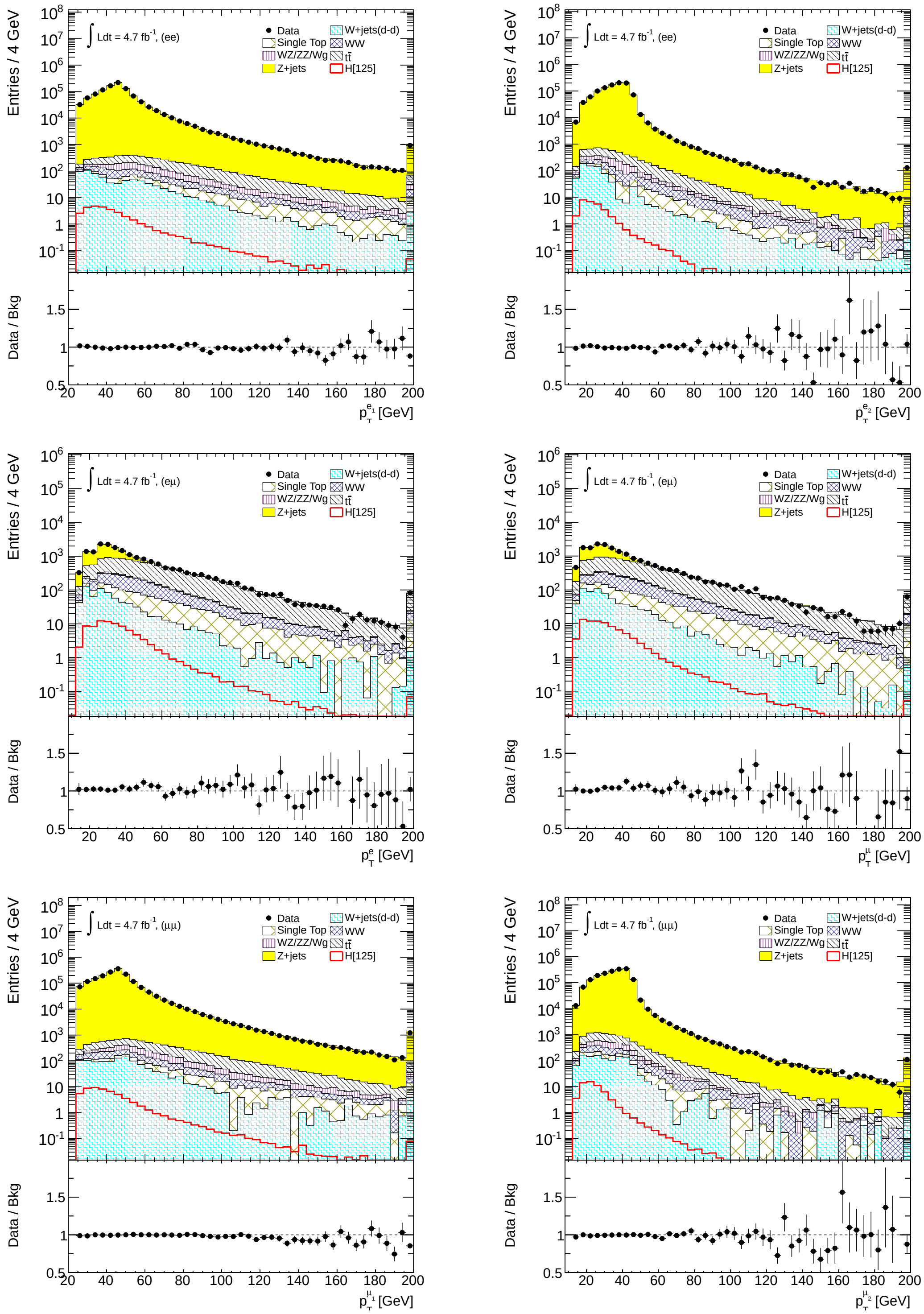

Figure 5.7 Lepton p_T distributions after low mass DY m_{ll} cut. Top row : *ee* channel with leading p_T electron on the left and subleading p_T electron on the right. Middle row : $e\mu$ channel with electron p_T on the left and muon p_T on the right. Bottom row : $\mu\mu$ channel with leading p_T muon on the left and subleading p_T muon on the right.

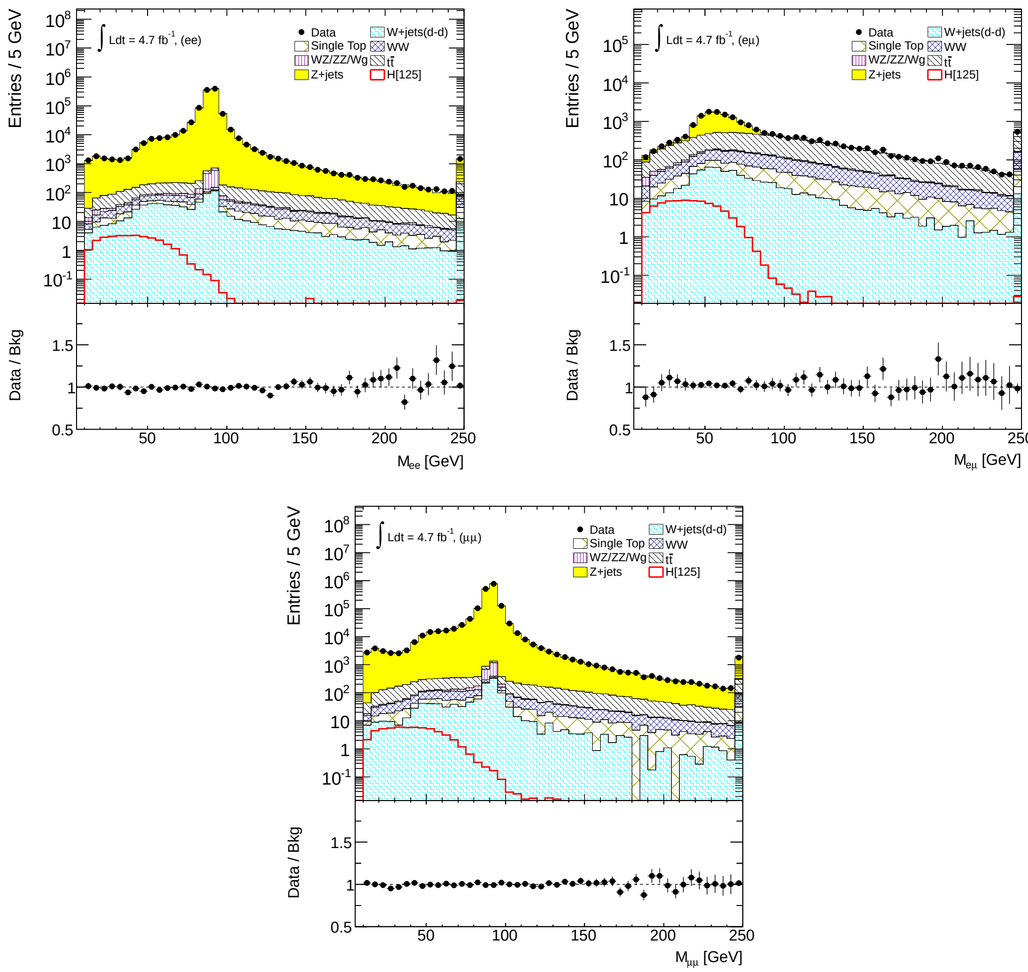

Figure 5.8 Di-lepton invariant mass m_{ll} distributions after low mass DY m_{ll} cut. The top left plot is for *ee* channel. the top right plot is for $e\mu$ channel. The bottom plot is for $\mu\mu$ channel.

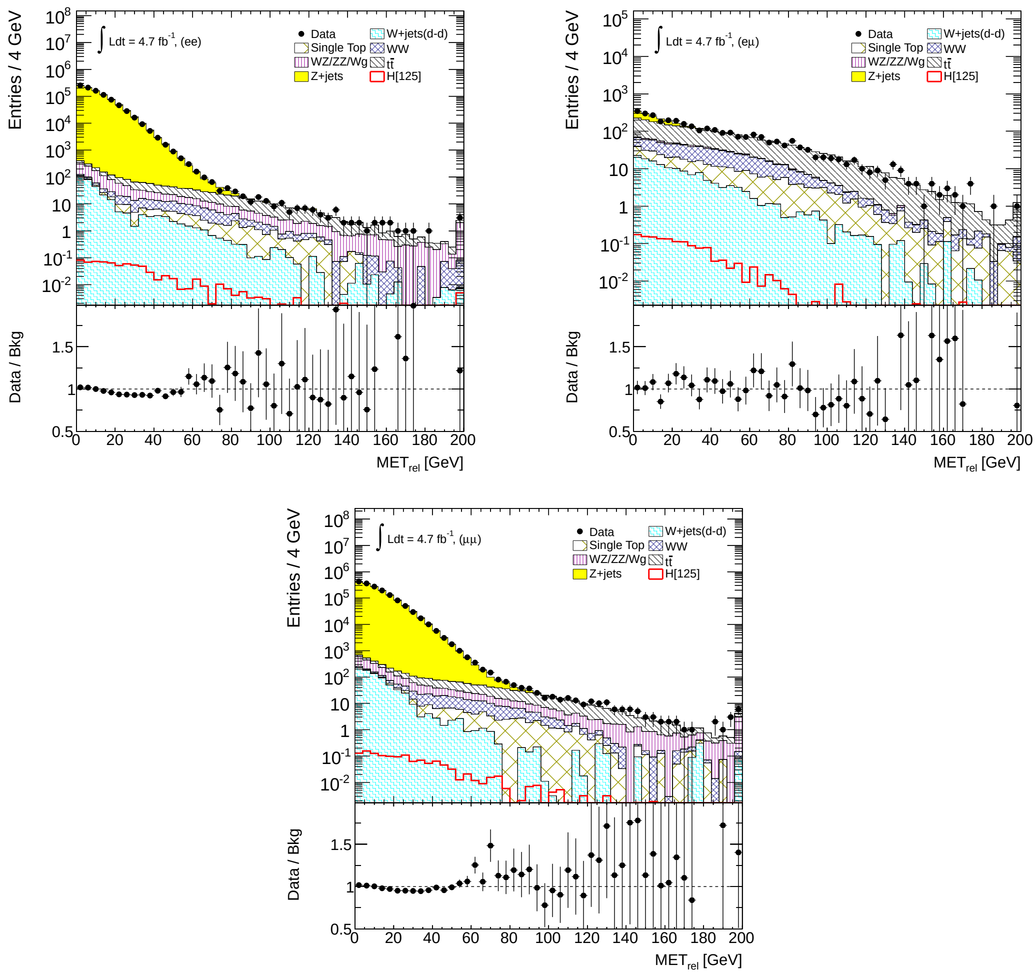

Figure 5.9 $E_{\mathrm{T,rel}}^{\mathrm{miss}}$ distributions in Z window ($|m_{ll} - m_Z| < 15$ GeV). The top left plot is for ee channel. the top right plot is for $e\mu$ channel. The bottom plot is for $\mu\mu$ channel.

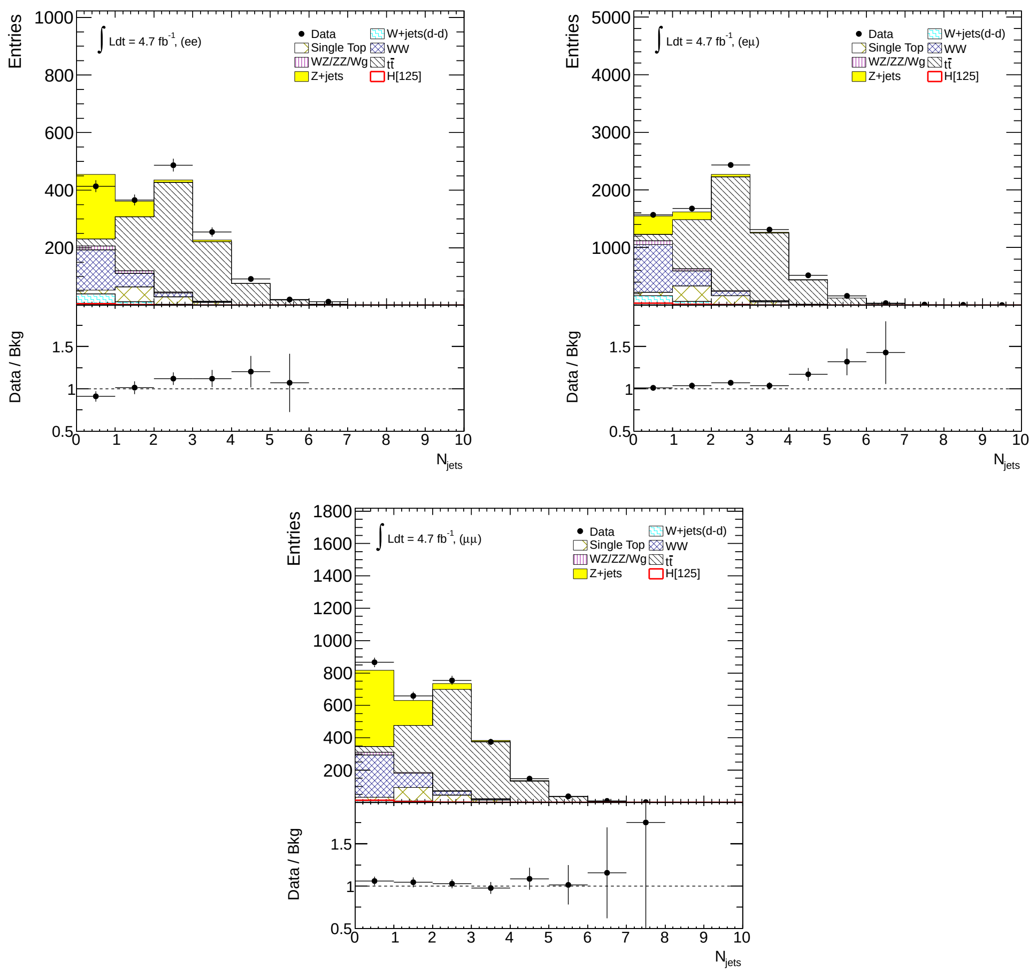

Figure 5.10 Jet multiplicity distributions after $E_{\mathrm{T,rel}}^{\mathrm{miss}}$ cut. The top left plot is for *ee* channel. the top right plot is for $e\mu$ channel. The bottom plot is for $\mu\mu$ channel.

Channel	Selection	Signal	ttbar	SingleTop	WW	WZ/ZZ/Wg	Zjets	WjetsDD	BG	Data
ee	TwoLepton	34.01 ± 0.17	3219.70 ± 12.41	347.17 ± 5.10	736.12 ± 4.24	1205.05 ± 13.80	1055207.75 ± 809.11	761.43 ± 12.08	1061477.12 ± 809.44	1056545
	LeadLepPt	32.42 ± 0.17	3191.76 ± 12.36	343.93 ± 5.08	725.35 ± 4.21	1166.23 ± 13.15	1032313.69 ± 800.37	761.43 ± 12.08	1038502.38 ± 800.70	1033180
	OppCharge	31.88 ± 0.17	3162.48 ± 12.31	340.01 ± 5.06	719.49 ± 4.19	1015.36 ± 9.94	1025296.94 ± 797.79	761.43 ± 12.08	1031295.69 ± 798.06	1027324
	DYRej	31.14 ± 0.17	3156.69 ± 12.29	339.39 ± 5.05	718.13 ± 4.19	1008.55 ± 9.87	1024452.50 ± 797.63	731.66 ± 12.05	1030406.88 ± 797.90	1024916
	ZRej	30.39 ± 0.16	2478.50 ± 10.91	267.26 ± 4.49	560.73 ± 3.68	163.53 ± 4.77	94308.60 ± 237.43	425.29 ± 5.47	98203.91 ± 237.86	97469
	MetRel	10.24 ± 0.10	895.76 ± 6.55	104.02 ± 2.79	202.77 ± 2.20	26.70 ± 1.88	292.96 ± 13.28	56.70 ± 1.10	1578.92 ± 15.39	1647
$e\mu$	TwoLepton	94.91 ± 0.29	8242.98 ± 19.65	888.01 ± 8.09	1930.31 ± 6.79	600.13 ± 13.43	8415.68 ± 54.19	743.51 ± 9.93	20820.62 ± 60.94	21983
	LeadLepPt	88.32 ± 0.28	8132.29 ± 19.52	876.79 ± 8.04	1886.97 ± 6.72	515.25 ± 11.90	6834.80 ± 49.00	743.51 ± 9.93	18989.62 ± 55.96	19815
	OppCharge	87.08 ± 0.27	8083.95 ± 19.46	867.63 ± 8.01	1877.83 ± 6.70	259.05 ± 6.21	6703.00 ± 48.29	743.51 ± 9.93	18534.97 ± 54.38	19045
	DYRej	86.24 ± 0.27	8076.57 ± 19.45	866.82 ± 8.00	1875.73 ± 6.70	252.44 ± 6.06	6686.43 ± 48.26	741.43 ± 9.91	18499.43 ± 54.33	19017
	ZRej	86.24 ± 0.27	8076.57 ± 19.45	866.82 ± 8.00	1875.73 ± 6.70	252.44 ± 6.06	6686.43 ± 48.26	741.43 ± 9.91	18499.43 ± 54.33	19017
	MetRel	58.28 ± 0.23	4678.09 ± 14.77	537.64 ± 6.31	1180.36 ± 5.30	124.49 ± 4.35	509.64 ± 12.96	261.80 ± 5.04	7292.03 ± 22.32	7719
$\mu\mu$	TwoLepton	66.17 ± 0.24	5111.84 ± 15.35	542.62 ± 6.24	1270.27 ± 5.45	1571.75 ± 10.82	1852959.12 ± 1059.59	1330.34 ± 32.39	1862786.00 ± 1060.28	1868224
	LeadLepPt	60.14 ± 0.23	5008.70 ± 15.18	532.59 ± 6.19	1230.74 ± 5.37	1532.14 ± 10.73	1759076.75 ± 1033.73	1330.34 ± 32.39	1768711.25 ± 1034.43	1766931
	OppCharge	59.48 ± 0.23	4993.88 ± 15.16	527.21 ± 6.16	1230.76 ± 5.37	1459.20 ± 10.58	1759070.00 ± 1033.73	1330.34 ± 32.39	1768611.38 ± 1034.43	1766680
	DYRej	57.76 ± 0.22	4978.50 ± 15.14	525.62 ± 6.15	1226.34 ± 5.36	1455.37 ± 10.58	1757143.50 ± 1033.47	1182.46 ± 32.10	1766511.75 ± 1034.16	1759444
	ZRej	56.48 ± 0.22	3901.31 ± 13.41	408.27 ± 5.43	957.75 ± 4.72	143.70 ± 2.15	176499.86 ± 321.75	408.37 ± 17.00	182319.25 ± 322.56	181823
	MetRel	22.31 ± 0.14	1480.40 ± 8.25	166.86 ± 3.47	379.58 ± 2.96	26.71 ± 0.84	670.89 ± 19.55	25.35 ± 2.86	2749.79 ± 21.91	2852

Table 5.3 The numbers of events after selecting two leptons with opposite charge and $m_{ll} > 12$ GeV ($m_{ll} > 10$ GeV for $e\mu$), after Z mass veto and $E_{\mathrm{T,rel}}^{\mathrm{miss}}$ cut. The W+jets contribution is estimated using data-driven method which will be mentioned in Section 6.2. Only statistic errors are given.

different cuts are designed to suppress different background in 0-jet, 1-jet and 2-jet channels.

5.6.2 Selection for $H+0$ Jet

Event which have two leptons, high $E_{\mathrm{T,rel}}^{\mathrm{miss}}$ and no $p_T > 25$ GeV jet within $|\eta| < 4.5$ will be categorized in $H+0$ jet channel. Some additional selection cuts will be applied to the events to reject more background.

- The transverse momentum of di-lepton system, p_{T}^{ll}, is required to be larger than 45 GeV for ee, $\mu\mu$ channels and 30 GeV for $e\mu$ channel. For same flavor channels, the low mass DY events can contribute to signal region if they are not treated properly. The p_{T}^{ll} distributions after 0-jet veto are shown in Fig. 5.11. A large fraction of DY events have p_{T}^{ll} less than 45 GeV for ee and $\mu\mu$ channels and less than 30 GeV for $e\mu$ channel. After this selection, most of the DY events will be rejected.

- For low mass Higgs search ($m_H < 200$ GeV)[2], selection $m_{ll} < 50$ GeV is applied. For $200 < m_H \leq 300$ GeV, this cut is $m_{ll} < 150$ GeV. For $m_H \geq 300$, there is no m_{ll} cut. Di-lepton invariant mass distributions after p_{T}^{ll} cut are shown in the left column of Fig. 5.12.

- The two leptons from Higgs to WW decay tend to have the same direction due to the spin correlation in WW system as explained in Section 5.1.2. For low mass Higgs search, $\Delta\phi_{\ell\ell}$ is required to be less than 1.8 radians. For Higgs mass $m_H \geq 200$ GeV, this cut is removed due to the large invariant mass of WW system. The $\Delta\phi_{\ell\ell}$ distributions are shown in right column of Fig. 5.12.

The transverse mass m_T distributions after 0-jet $\Delta\phi_{ll}$ selections are shown in Fig. 5.13. Table 5.4 is showing the expected and observed number of events for different cuts in 0-jet channel. WW processes are the dominant background in different flavor channels for this analysis. It is 64%

[2] Low mass Higgs is referred to $m_H < 200$ GeV and high mass Higgs is referred to $m_H \geq 200$ GeV.

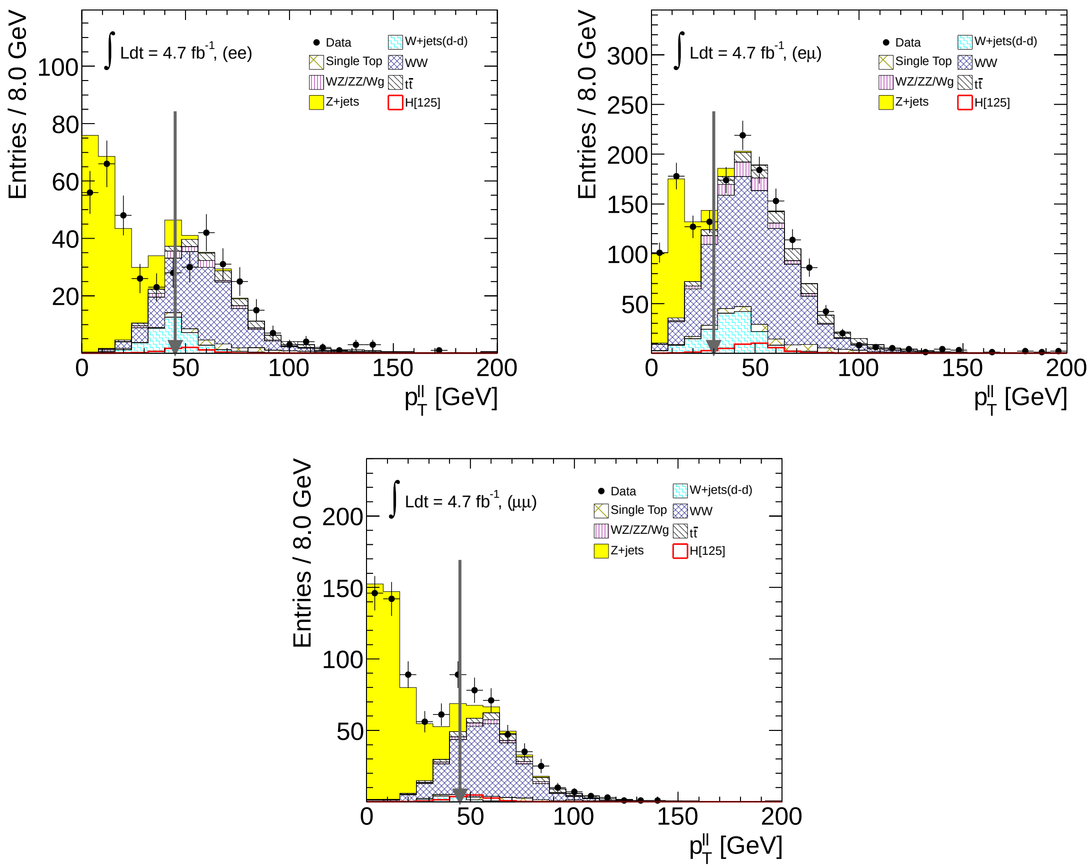

Figure 5.11 p_T^{ll} distributions after 0-jet veto in ee (top left), $e\mu$ (top right) and $\mu\mu$ (bottom) channels.

for *ee*, 60% in $e\mu$ and 69% in $\mu\mu$ channel from pure MC estimation. The total background is a little bit higher than data in *ee* and $e\mu$ and is lower than data in $\mu\mu$ channel.

Channel	Selection	Signal	ttbar	SingleTop	WW	WZ/ZZ/Wg	Zjets	WjetsDD	BG	Data
ee	0jet_ZeroJet	6.26 ± 0.08	24.28 ± 1.09	13.87 ± 1.02	138.96 ± 1.85	13.41 ± 1.43	224.21 ± 11.89	39.63 ± 0.87	454.35 ± 12.24	414
	0jet_PtLL	4.38 ± 0.07	20.46 ± 1.00	11.94 ± 0.95	109.07 ± 1.64	9.29 ± 1.07	6.63 ± 1.91	17.30 ± 0.53	174.69 ± 3.11	179
	0jet_mLL	4.01 ± 0.06	3.49 ± 0.48	3.19 ± 0.49	36.37 ± 0.95	4.08 ± 0.80	3.77 ± 1.23	7.76 ± 0.38	58.66 ± 1.92	52
	0jet_deltaPhi	4.00 ± 0.06	3.49 ± 0.48	3.19 ± 0.49	36.32 ± 0.95	4.08 ± 0.80	3.77 ± 1.23	7.72 ± 0.38	58.56 ± 1.92	52
$e\mu$	0jet_ZeroJet	36.14 ± 0.18	107.40 ± 2.23	58.20 ± 2.07	828.13 ± 4.48	66.04 ± 3.36	321.26 ± 11.00	166.41 ± 3.13	1547.43 ± 13.10	1567
	0jet_PtLL	33.13 ± 0.18	95.21 ± 2.11	52.15 ± 1.96	693.22 ± 4.09	54.17 ± 2.99	13.90 ± 2.32	125.53 ± 2.45	1034.18 ± 6.74	1068
	0jet_mLL	26.75 ± 0.16	15.57 ± 0.91	9.28 ± 0.83	163.57 ± 2.01	24.47 ± 2.34	1.73 ± 0.72	40.47 ± 1.37	255.09 ± 3.66	253
	0jet_deltaPhi	25.67 ± 0.15	15.18 ± 0.90	9.21 ± 0.82	157.35 ± 1.97	23.00 ± 2.25	1.41 ± 0.68	35.41 ± 1.25	241.57 ± 3.54	239
$\mu\mu$	0jet_ZeroJet	14.32 ± 0.12	35.62 ± 1.30	19.33 ± 1.18	262.02 ± 2.48	17.16 ± 0.66	469.59 ± 16.68	12.53 ± 1.58	816.25 ± 17.04	866
	0jet_PtLL	10.20 ± 0.10	29.39 ± 1.17	16.56 ± 1.09	201.82 ± 2.18	13.40 ± 0.58	23.38 ± 3.33	3.79 ± 0.83	288.34 ± 4.41	311
	0jet_mLL	9.37 ± 0.09	7.21 ± 0.60	4.65 ± 0.58	72.33 ± 1.32	6.20 ± 0.41	16.20 ± 2.51	1.54 ± 0.52	108.13 ± 3.03	138
	0jet_deltaPhi	9.34 ± 0.09	7.17 ± 0.60	4.58 ± 0.57	72.23 ± 1.32	6.20 ± 0.41	16.20 ± 2.51	1.54 ± 0.52	107.92 ± 3.03	138

Table 5.4 The number of expected and observed events in $H+0j$ channel. The uncertainties are statistic error only. Signal sample is from $m_H = 125$ GeV Monte Carlo.

5.6.3 Selection for $H+1$ Jet

Event which have two leptons, high $E_{\mathrm{T,rel}}^{\mathrm{miss}}$ and one $p_T > 25$ GeV jet within $|\eta| < 4.5$ will be categorized in $H+1$ jet channel. Those events have to pass the following selections :

- Events should not contain any *b*-jets to suppress Top background since Top quark will decay to two *b*-jets. The *b*-tagging algorithm is using `JetFitter+IP3D` as mentioned in Section 4.4. If the *b*-tag weight is bigger than -1.25, then jet will be considered as a *b*-jet. This operation point has 80% efficiency for *b*-jets in Top MC events.

- The total p_{T} of event which is defined as the vector sum $\mathbf{p}_{\mathrm{T}}^{\mathrm{tot}} = \mathbf{p}_{\mathrm{T}}^{\mathrm{l1}} + \mathbf{p}_{\mathrm{T}}^{\mathrm{l2}} + \mathbf{p}_{\mathrm{T}}^{\mathrm{j}} + \mathbf{p}_{\mathrm{T}}^{\mathrm{miss}}$, is required to be not larger than 30 GeV. This will suppress the events with soft gluon radiation that recoils against the $ll+1j$ system but does not produce other $p_{\mathrm{T}} > 25$ GeV jets. In the event selection, only jets with $p_{\mathrm{T}} > 25$ GeV are selected. It's possible that the event has

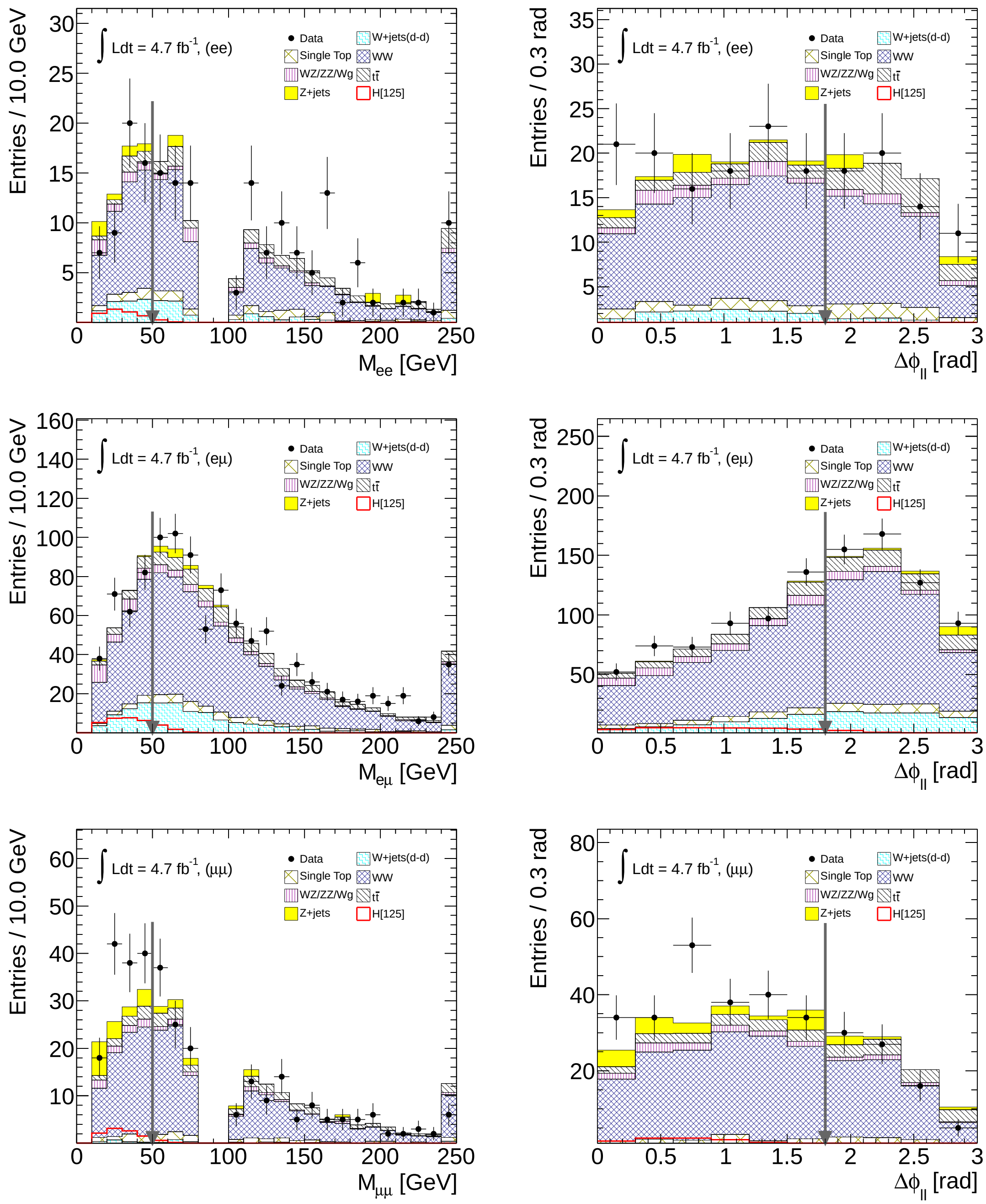

Figure 5.12 m_{ll} and $\Delta\phi_{ll}$ distributions after 0-jet p_{T}^{ll} in *ee* (top row), $e\mu$ (middle row) and $\mu\mu$ (bottom row) channels. Most of DY events are already rejected by p_{T}^{ll} cut.

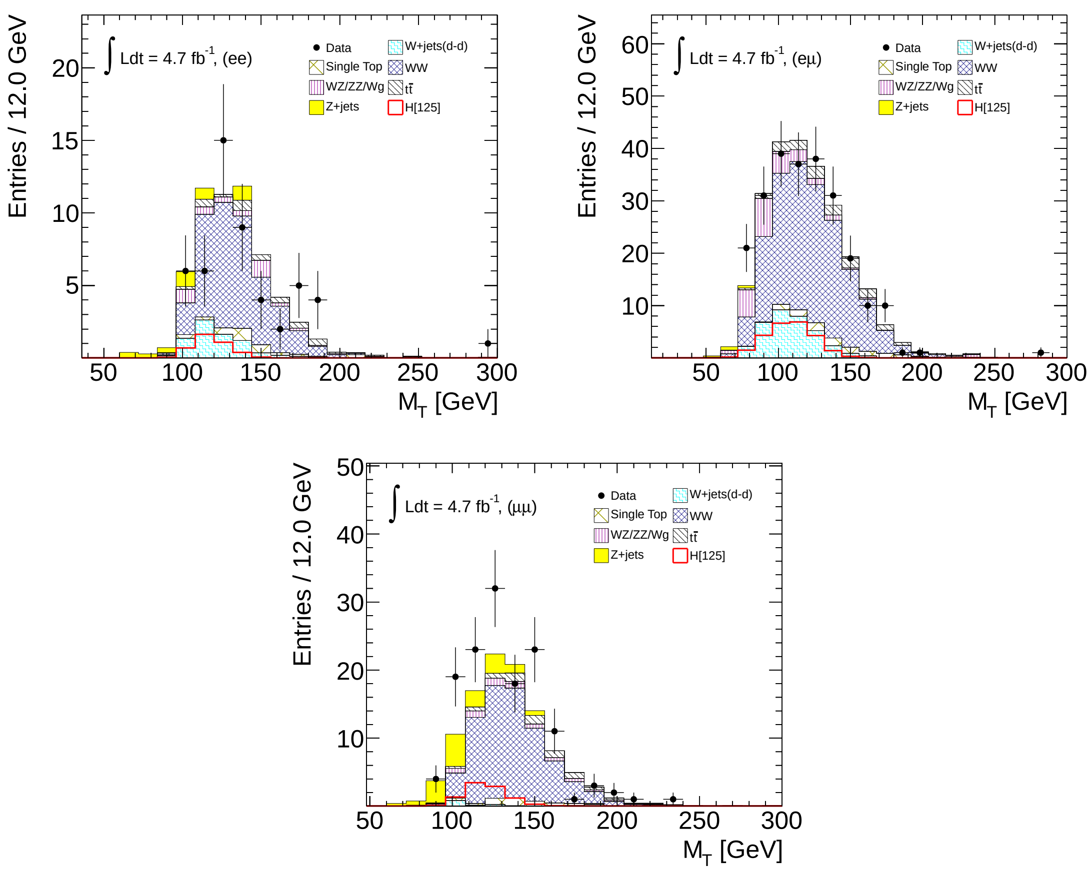

Figure 5.13 m_T distributions after 0-jet $\Delta\phi_{ll}$ cut in ee (top left), $e\mu$ (top right) and $\mu\mu$ (bottom) channels.

several jets with $p_{\mathrm{T}} < 25$ GeV which will lead to large $p_{\mathrm{T}}^{\mathrm{tot}}$ value. Fig. 5.14 shows the $p_{\mathrm{T}}^{\mathrm{tot}}$ distributions after 1-jet veto.

- $Z \rightarrow \tau\tau$ veto to suppress Z to $\tau\tau$ events. Only the leptonic decay of τ will pass the di-lepton selection. Since τ has small mass and it can have high p_T, the visible decay products and neutrinos can be collinear which is called collinear approximation. The invariant mass of $\tau\tau$ system can be reconstructed using collinear approximation :

$$m_{\tau\tau} = \frac{m_{ll}}{\sqrt{x1\,x2}}, \tag{5.5}$$

where $x1$,$x2$ are the momentum fractions of lepton momentum and τ momentum. $x1, x2$ can be calculated as,

$$x1 = \frac{p_x^{l1} p_y^{l2} - p_y^{l1} p_x^{l2}}{p_y^{l2} E_x^{miss} - p_x^{l2} E_y^{miss} + p_x^{l1} p_y^{l2} - p_y^{l1} p_x^{l2}}, \tag{5.6}$$

$$x1 = \frac{p_x^{l1} p_y^{l2} - p_y^{l1} p_x^{l2}}{p_y^{l1} E_x^{miss} - p_x^{l1} E_y^{miss} + p_x^{l1} p_y^{l2} - p_y^{l1} p_x^{l2}}. \tag{5.7}$$

$m_{\tau\tau}$ will be set to zero if $x1 \cdot x2 < 0$. The event with $|m_{\tau\tau} - m_Z| < 25$ GeV will be rejected.

- Apply the same m_{ll} and $\Delta\phi$ selections as mentioned in Section 5.6.2. The plots after $Z \rightarrow \tau\tau$ veto are shown in Fig. 5.15.

The m_T distributions after all the 1-jet selections are shown in Fig. 5.16. The number of expected and observed events after different cuts are list in Table 5.5. The b-jet veto reduces a lot of $t\bar{t}$ and single Top background. $p_{\mathrm{T}}^{\mathrm{tot}}$ is also very efficient to reject Top background since Top can produce several low p_T jets. $Z \rightarrow \tau\tau$ veto rejects lot of $Z + jets$ events in $e\mu$ channel in which no Z mass veto is applied. In ee and $\mu\mu$ channel, $Z \rightarrow \tau\tau$ veto has less rejection power. The m_{ll} cut is very important for WW background suppression. After all the selections, WW is the main background which is 38% in ee channel, 37% in $e\mu$ channel and 42% in $\mu\mu$ channel from pure MC estimation. Top background is more important in 1-jet channel compared with 0-jet case. It's 30% in ee channel, 32% in $e\mu$ channel and 35% in $\mu\mu$ channel from pure MC estimation.

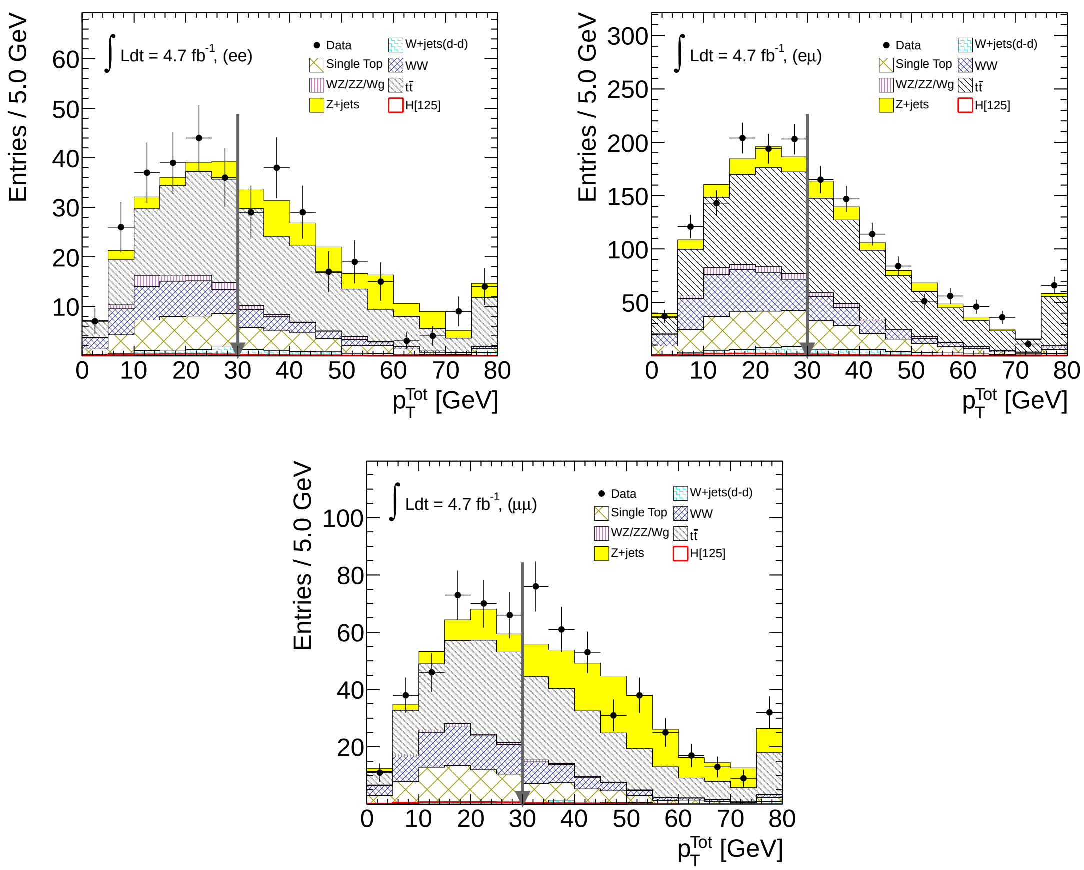

Figure 5.14 $p_{\mathrm{T}}^{\mathrm{tot}}$ distributions after 1-jet veto in *ee* (top left), $e\mu$ (top right) and $\mu\mu$ (bottom) channels.

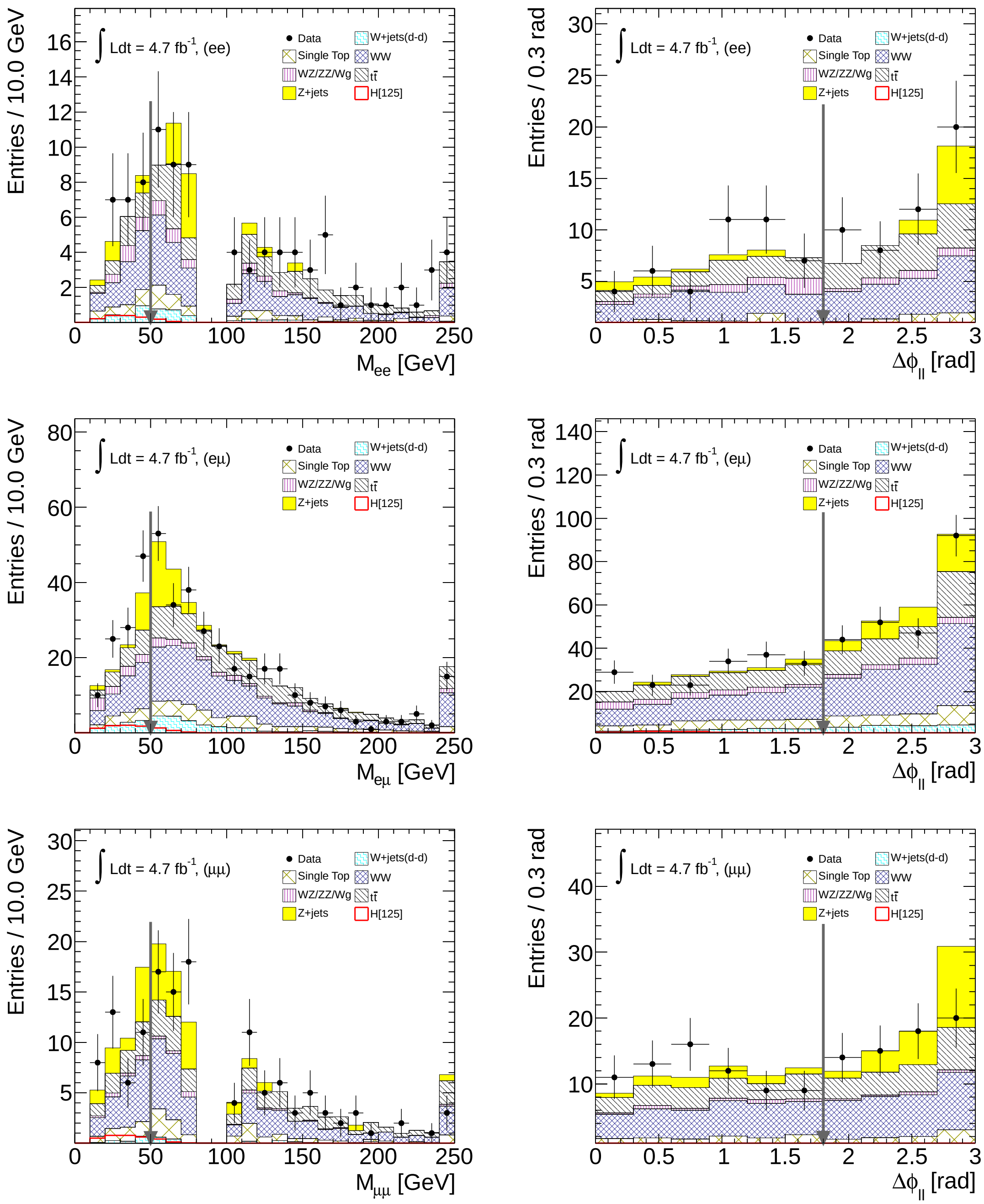

Figure 5.15 m_{ll} and $\Delta\phi$ distributions after $Z \to \tau\tau$ veto in ee (top row), $e\mu$ (middle row) and $\mu\mu$ (bottom row) channels.

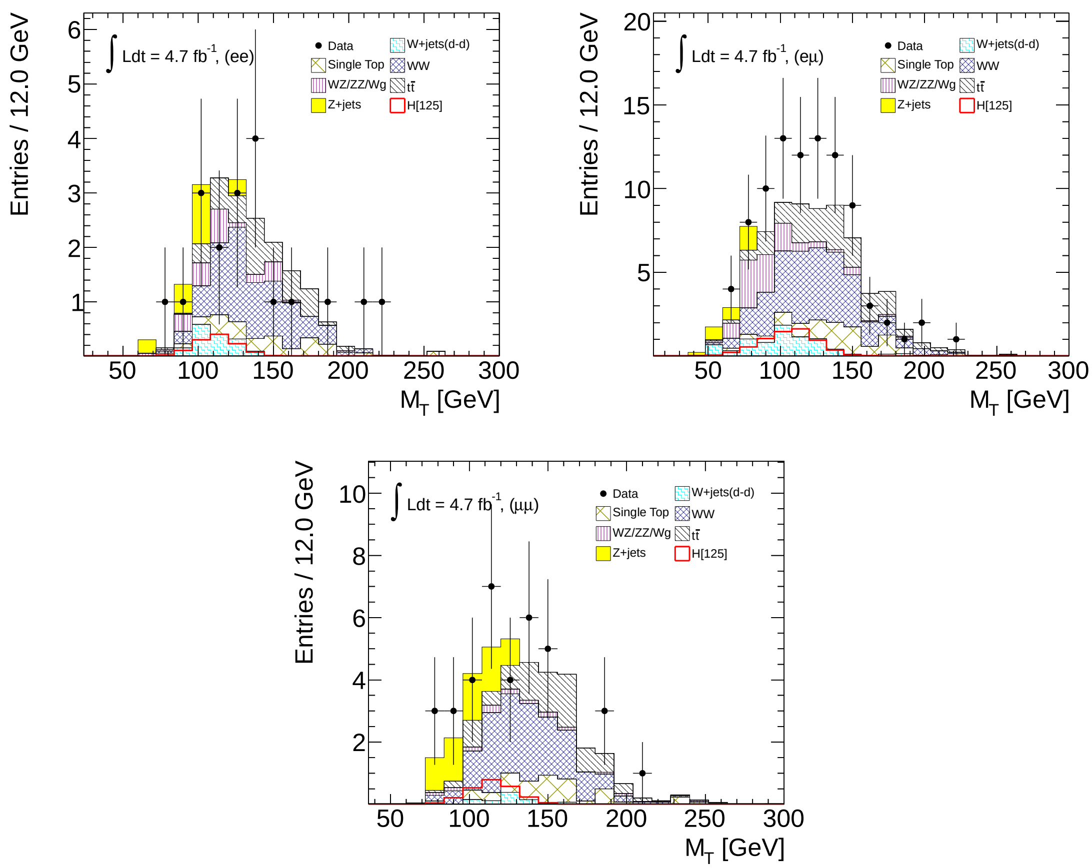

Figure 5.16 m_T distributions after 1-jet $\Delta\phi_{ll}$ cut in *ee* (top left), $e\mu$ (top right) and $\mu\mu$ (bottom) channels.

Channel	Selection	Signal	ttbar	SingleTop	WW	WZ/ZZ/Wg	Zjets	WjetsDD	BG	Data
ee	1jet_OneJet	2.58 ± 0.05	187.79 ± 2.98	51.99 ± 1.98	46.57 ± 1.03	9.14 ± 1.08	53.14 ± 5.35	12.39 ± 0.50	361.03 ± 6.62	366
	1jet_Bjet	2.38 ± 0.04	53.71 ± 1.60	15.71 ± 1.09	43.52 ± 0.99	8.85 ± 1.08	48.30 ± 5.09	11.34 ± 0.46	181.42 ± 5.66	200
	1jet_PtTotal	1.61 ± 0.04	23.65 ± 1.04	8.58 ± 0.81	31.26 ± 0.84	6.54 ± 1.00	10.62 ± 2.28	5.17 ± 0.32	85.82 ± 2.96	94
	1jet_Ztau	1.60 ± 0.04	23.07 ± 1.03	8.19 ± 0.79	30.68 ± 0.84	6.49 ± 1.00	10.02 ± 2.24	5.23 ± 0.32	83.68 ± 2.92	93
	1jet_mLL	1.33 ± 0.03	4.21 ± 0.49	2.41 ± 0.43	8.20 ± 0.43	2.21 ± 0.63	2.39 ± 0.88	2.05 ± 0.21	21.47 ± 1.35	22
	1jet_deltaPhi	1.22 ± 0.03	4.00 ± 0.49	2.34 ± 0.43	7.68 ± 0.42	2.15 ± 0.63	2.16 ± 0.85	1.66 ± 0.19	20.00 ± 1.32	19
$e\mu$	1jet_OneJet	14.74 ± 0.11	853.50 ± 6.30	266.23 ± 4.44	259.54 ± 2.45	39.78 ± 2.38	132.34 ± 5.93	64.72 ± 2.42	1616.10 ± 10.59	1678
	1jet_Bjet	13.57 ± 0.10	243.56 ± 3.41	85.60 ± 2.53	241.69 ± 2.35	36.78 ± 2.27	122.54 ± 5.68	58.40 ± 2.10	788.57 ± 8.09	808
	1jet_PtTotal	9.12 ± 0.08	107.66 ± 2.25	48.46 ± 1.90	171.41 ± 1.99	23.94 ± 1.89	67.50 ± 4.28	29.23 ± 1.46	448.20 ± 6.05	449
	1jet_Ztau	9.09 ± 0.08	102.46 ± 2.20	46.35 ± 1.86	166.35 ± 1.96	23.55 ± 1.88	45.77 ± 3.62	31.01 ± 1.45	415.48 ± 5.56	414
	1jet_mLL	6.90 ± 0.07	17.40 ± 0.96	9.25 ± 0.83	31.70 ± 0.86	9.99 ± 1.42	12.44 ± 1.85	9.21 ± 0.83	89.98 ± 2.91	110
	1jet_deltaPhi	6.39 ± 0.07	16.39 ± 0.93	9.04 ± 0.82	28.49 ± 0.81	9.62 ± 1.42	3.09 ± 1.00	7.66 ± 0.71	74.30 ± 2.39	90
$\mu\mu$	1jet_OneJet	5.32 ± 0.06	289.53 ± 3.65	84.72 ± 2.48	86.30 ± 1.39	6.71 ± 0.43	153.95 ± 8.89	8.70 ± 1.50	629.92 ± 10.14	659
	1jet_Bjet	4.92 ± 0.06	84.20 ± 1.99	26.98 ± 1.40	79.89 ± 1.34	6.28 ± 0.41	145.94 ± 8.63	6.13 ± 1.21	349.43 ± 9.16	360
	1jet_PtTotal	3.30 ± 0.05	35.94 ± 1.31	17.14 ± 1.12	55.91 ± 1.13	3.56 ± 0.31	30.41 ± 3.98	2.85 ± 0.77	145.82 ± 4.56	141
	1jet_Ztau	3.30 ± 0.05	35.03 ± 1.30	16.74 ± 1.11	55.28 ± 1.12	3.54 ± 0.31	29.29 ± 3.92	3.06 ± 0.77	142.94 ± 4.50	137
	1jet_mLL	2.70 ± 0.04	8.75 ± 0.68	4.64 ± 0.58	16.17 ± 0.60	1.33 ± 0.20	10.50 ± 2.11	1.22 ± 0.46	42.61 ± 2.42	38
	1jet_deltaPhi	2.49 ± 0.04	8.38 ± 0.66	4.45 ± 0.57	14.87 ± 0.58	1.32 ± 0.20	6.22 ± 1.41	0.91 ± 0.40	36.15 ± 1.81	36

Table 5.5 The number of expected and observed events in $H+1j$ channel. The uncertainties are statistic error only. Signal sample is from $m_H = 125$ GeV Monte Carlo.

5.6.4 Selection for $H+2$ Jet

Vector boson fusion (VBF) process can produce two forward jets which have large η separation. Event which have two leptons, high $E_{\mathrm{T,rel}}^{\mathrm{miss}}$ and two $p_T > 25$ GeV jets within $|\eta| < 4.5$ will be categorized in $H+2$ jet channel. Besides the two tagged jets, event should not contain any other $p_T > 25$ GeV jets within $|\eta| < 3.2$. This is called central jet veto. The b-jet veto is the same with the definition in Section. 5.6.3. The two jets have to locate in opposite rapidity hemispheres ($\eta_{j1} \times \eta_{j2} < 0$). The $\Delta\eta$ of the two jets should be larger than 3.8. The distributions of $\Delta\eta$ after 2-jet veto are shown in the left column of Fig. 5.6. The two jet invariant mass m_{jj} should be at least 500 GeV due to the feature of VBF process. The right column of Fig. 5.6 shows the m_{jj} distributions after 2-jet veto. The di-lepton invariant mass cut is $m_{ll} < 80$ GeV. The candidate events will have pass the $\Delta\phi$ selections as described in Section. 5.6.2.

Table 5.6 shows the expected and observed number of events after different cuts in 2-jet channel. Top is dominant background in the channel.

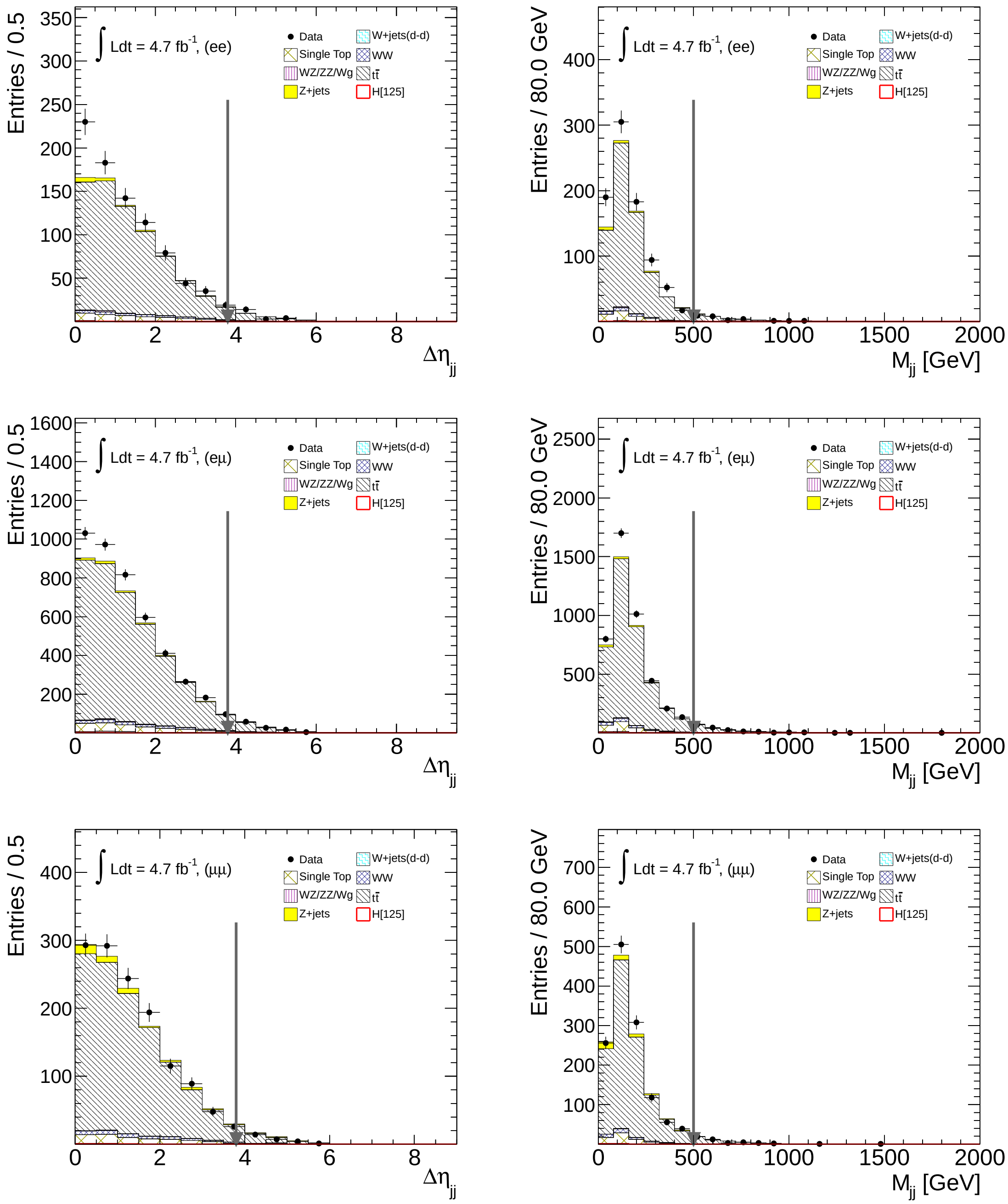

Figure 5.17 $\Delta\eta_{jj}$ and m_{jj} distributions after 2-jet veto in *ee* (top row), $e\mu$ (middle row) and $\mu\mu$ (bottom row) channels.

Channel	Selection	Signal	ttbar	SingleTop	WW	WZ/ZZ/Wg	Zjets	WjetsDD	BG	Data
ee	2jet_TwoJet	1.40 ± 0.03	682.63 ± 5.75	38.19 ± 1.70	17.05 ± 0.61	4.11 ± 0.55	14.69 ± 2.34	4.68 ± 0.46	761.35 ± 6.50	867
	2jet_CJetVeto	1.08 ± 0.03	397.93 ± 4.35	27.06 ± 1.43	13.53 ± 0.55	3.09 ± 0.51	8.62 ± 1.85	4.68 ± 0.46	454.91 ± 5.02	510
	2jet_Bjet	0.91 ± 0.03	42.71 ± 1.46	5.91 ± 0.68	11.89 ± 0.50	2.76 ± 0.49	8.05 ± 1.76	3.48 ± 0.28	74.80 ± 2.50	96
	2jet_OppHemi	0.49 ± 0.02	19.28 ± 0.97	3.02 ± 0.48	5.56 ± 0.34	0.97 ± 0.19	3.62 ± 1.20	1.28 ± 0.18	33.73 ± 1.67	37
	2jet_DeltaEta	0.22 ± 0.01	3.40 ± 0.40	0.27 ± 0.14	1.14 ± 0.15	0.25 ± 0.10	1.23 ± 0.87	0.22 ± 0.07	6.52 ± 0.99	8
	2jet_Mjj	0.15 ± 0.01	1.89 ± 0.30	0.00 ± 0.00	0.45 ± 0.09	0.03 ± 0.01	0.00 ± 0.00	0.05 ± 0.04	2.41 ± 0.32	2
	2jet_PtTotal	0.11 ± 0.00	0.90 ± 0.20	0.00 ± 0.00	0.28 ± 0.07	0.02 ± 0.01	0.00 ± 0.00	0.02 ± 0.03	1.22 ± 0.21	1
	2jet_Ztau	0.11 ± 0.00	0.90 ± 0.20	0.00 ± 0.00	0.28 ± 0.07	0.02 ± 0.01	0.00 ± 0.00	0.02 ± 0.03	1.22 ± 0.21	1
	2jet_mLL	0.10 ± 0.00	0.04 ± 0.06	0.00 ± 0.00	0.04 ± 0.03	0.01 ± 0.01	0.00 ± 0.00	0.01 ± 0.02	0.10 ± 0.07	0
	2jet_deltaPhi	0.09 ± 0.00	0.00 ± 0.05	0.00 ± 0.00	0.04 ± 0.03	0.01 ± 0.01	0.00 ± 0.00	0.01 ± 0.02	0.06 ± 0.06	0
$e\mu$	2jet_TwoJet	7.35 ± 0.08	3711.90 ± 13.23	212.35 ± 3.97	92.00 ± 1.40	18.60 ± 1.39	55.58 ± 3.39	30.67 ± 3.12	4121.10 ± 14.70	4474
	2jet_CJetVeto	5.78 ± 0.07	2068.23 ± 9.80	151.50 ± 3.36	73.72 ± 1.26	14.52 ± 1.31	41.66 ± 3.06	28.86 ± 3.03	2378.49 ± 11.36	2547
	2jet_Bjet	4.90 ± 0.06	225.60 ± 3.30	32.63 ± 1.56	63.44 ± 1.15	13.09 ± 1.27	36.21 ± 2.84	20.94 ± 1.90	391.91 ± 5.28	407
	2jet_OppHemi	2.73 ± 0.04	98.64 ± 2.17	12.67 ± 0.97	29.73 ± 0.79	5.46 ± 0.80	15.10 ± 1.83	8.48 ± 1.16	170.08 ± 3.40	164
	2jet_DeltaEta	1.18 ± 0.02	17.29 ± 0.89	1.31 ± 0.30	5.23 ± 0.33	0.53 ± 0.12	1.51 ± 0.55	1.39 ± 0.39	27.27 ± 1.21	22
	2jet_Mjj	0.83 ± 0.01	8.88 ± 0.62	0.90 ± 0.26	2.59 ± 0.23	0.26 ± 0.09	0.44 ± 0.23	0.48 ± 0.27	13.55 ± 0.80	9
	2jet_PtTotal	0.63 ± 0.01	3.56 ± 0.39	0.60 ± 0.21	1.56 ± 0.18	0.13 ± 0.06	0.27 ± 0.19	0.17 ± 0.14	6.29 ± 0.54	4
	2jet_Ztau	0.62 ± 0.01	3.53 ± 0.39	0.60 ± 0.21	1.50 ± 0.17	0.14 ± 0.06	0.15 ± 0.15	0.20 ± 0.14	6.11 ± 0.52	4
	2jet_mLL	0.49 ± 0.01	0.41 ± 0.15	0.08 ± 0.08	0.26 ± 0.08	0.09 ± 0.06	0.15 ± 0.15	0.08 ± 0.08	1.08 ± 0.26	2
	2jet_deltaPhi	0.47 ± 0.01	0.39 ± 0.14	0.08 ± 0.08	0.19 ± 0.06	0.09 ± 0.06	0.00 ± 0.00	0.07 ± 0.08	0.82 ± 0.20	1
$\mu\mu$	2jet_TwoJet	2.65 ± 0.05	1154.21 ± 7.31	62.50 ± 2.13	31.05 ± 0.81	2.80 ± 0.29	45.53 ± 4.79	4.12 ± 1.84	1300.21 ± 9.23	1327
	2jet_CJetVeto	2.11 ± 0.04	656.15 ± 5.48	45.68 ± 1.82	24.63 ± 0.73	1.91 ± 0.24	36.46 ± 4.36	3.67 ± 1.82	768.51 ± 7.50	791
	2jet_Bjet	1.78 ± 0.04	73.70 ± 1.88	9.37 ± 0.82	21.21 ± 0.67	1.73 ± 0.22	31.07 ± 4.01	2.57 ± 1.08	139.64 ± 4.69	172
	2jet_OppHemi	0.96 ± 0.02	30.44 ± 1.22	4.38 ± 0.56	9.97 ± 0.45	0.87 ± 0.14	11.34 ± 2.33	1.84 ± 0.81	58.83 ± 2.85	71
	2jet_DeltaEta	0.41 ± 0.01	5.91 ± 0.51	0.82 ± 0.25	1.66 ± 0.19	0.14 ± 0.06	2.89 ± 1.18	0.50 ± 0.34	11.92 ± 1.36	10
	2jet_Mjj	0.29 ± 0.01	2.47 ± 0.33	0.39 ± 0.18	0.67 ± 0.12	0.10 ± 0.06	0.25 ± 0.25	0.62 ± 0.34	4.51 ± 0.58	2
	2jet_PtTotal	0.21 ± 0.01	1.04 ± 0.22	0.18 ± 0.13	0.54 ± 0.10	0.05 ± 0.05	0.00 ± 0.00	0.35 ± 0.24	2.16 ± 0.37	1
	2jet_Ztau	0.21 ± 0.01	0.99 ± 0.22	0.18 ± 0.13	0.54 ± 0.10	0.05 ± 0.05	0.00 ± 0.00	0.36 ± 0.24	2.13 ± 0.37	1
	2jet_mLL	0.18 ± 0.01	0.21 ± 0.12	0.08 ± 0.08	0.10 ± 0.05	0.00 ± 0.00	0.00 ± 0.00	0.23 ± 0.18	0.62 ± 0.23	0
	2jet_deltaPhi	0.17 ± 0.01	0.21 ± 0.12	0.08 ± 0.08	0.08 ± 0.05	0.00 ± 0.00	0.00 ± 0.00	-0.02 ± 0.01	0.36 ± 0.15	0

Table 5.6 The number of expected and observed events in $H+2j$ channel. The uncertainties are statistic error only. Signal sample is from $m_H = 125$ GeV Monte Carlo.

Chapter 6

Background Estimation

6.1 Drell-Yan Background Estimation

Drell-Yan (γ^*, Υ, Z) processes have a signature of two leptons. In principle, those background will not affect the signal region which has large missing transverse momentum ($E_{\mathrm{T}}^{\mathrm{miss}}$). But that is not true when there is fake $E_{\mathrm{T}}^{\mathrm{miss}}$. The fake $E_{\mathrm{T}}^{\mathrm{miss}}$ mainly comes from the detector noise or pile-up interaction. Since the modeling of detector noise and pile-up is not perfect in Monte Carlo samples, the modeling of Drell-Yan processes from Monte Carlo is not sufficient in $H \rightarrow WW$ analysis. Therefore, a data-driven ABCD method is developed to correct the effect of $E_{\mathrm{T}}^{\mathrm{miss}}$ mis-modeling in Drell-Yan Monte Carlo.

6.1.1 $E_{\mathrm{T}}^{\mathrm{miss}}$ Mis-modeling in Z Window

Fig. 5.9 is showing the $E_{\mathrm{T}}^{\mathrm{miss}}$ distributions in Z window ($|m_{ll} - m_Z| < 15$ GeV). The Drell-Yan samples contribute to the low $E_{\mathrm{T}}^{\mathrm{miss}}$ region ($E_{\mathrm{T,rel}}^{\mathrm{miss}} < 70$ GeV) mostly. Data is about 9% lower than MC at $E_{\mathrm{T,rel}}^{\mathrm{miss}} = 30$ GeV region and is about 20% higher than MC at $E_{\mathrm{T,rel}}^{\mathrm{miss}} = 70$ GeV region both for ee and $\mu\mu$ channels. This mis-modeling of $E_{\mathrm{T}}^{\mathrm{miss}}$ presents inside and outside of Z window because

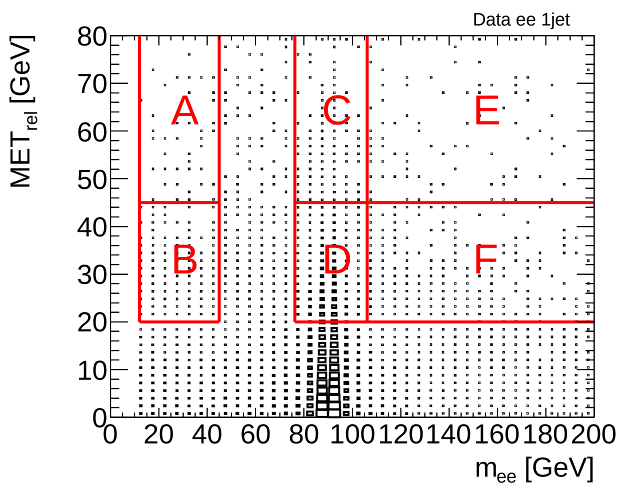

Figure 6.1 Illustration of ABCD method for Drell-Yan background estimation. *A* is the signal region which has large $E_{\mathrm{T}}^{\mathrm{miss}}$ and low m_{ll}. *CDEF* regions are used for WW control region.

it is caused by soft interactions like detector noise and pile-up. And those soft interactions are very hard to simulate in MC.

For the high $E_{\mathrm{T,rel}}^{\mathrm{miss}}$ region, real $E_{\mathrm{T}}^{\mathrm{miss}}$ samples like $t\bar{t}$, dominate the distribution.

6.1.2 ABCD Method

The ABCD method is explained in Fig. 6.1. The four kinematic regions are defined as : **A (signal region)** : $12 < m_{ll} < 50$ GeV and $E_{\mathrm{T,rel}}^{\mathrm{miss}} > 45$ GeV , **B** : $12 < m_{ll} < 50$ GeV and $20 < E_{\mathrm{T,rel}}^{\mathrm{miss}} < 45$ GeV, **C** : $|m_{ll} - m_Z| < 15$ GeV and $E_{\mathrm{T,rel}}^{\mathrm{miss}} > 45$ GeV, **D** : $|m_{ll} - m_Z| < 15$ GeV and $20 < E_{\mathrm{T,rel}}^{\mathrm{miss}} < 45$ GeV, **E** : $m_{ll} > m_Z + 15$ GeV and $E_{\mathrm{T,rel}}^{\mathrm{miss}} > 45$ GeV, **F** : $m_{ll} > m_Z + 15$ GeV and $20 < E_{\mathrm{T,rel}}^{\mathrm{miss}} < 45$ GeV. It is assumed that the di-lepton invariant mass (m_{ll}) and the $E_{\mathrm{T}}^{\mathrm{miss}}$ are not correlated. Then the ratio of **A** and **B** should be similar with the ratio of **C** and **D**. The estimation in signal region **A** is

$$A_{\mathrm{Z+jets}}^{\mathrm{estimated}} = B_{\mathrm{obs}} \times \frac{C_{\mathrm{obs}}}{D_{\mathrm{obs}}}, \tag{6.1}$$

where the contamination from other non-DY processes are subtracted using Monte Carlo predictions.

The $H\to WW^{(*)}\to \ell\nu\ell\nu$ analysis is using WW control region to constrain the WW background in signal region. In WW control region, the DY background needs to be subtracted. The contamination of DY events in WW control region are also estimated using ABCD method :

$$E_{\mathrm{Z+jets}}^{\mathrm{estimated}} = F_{\mathrm{obs}} \times \frac{C_{\mathrm{obs}}}{D_{\mathrm{obs}}}. \tag{6.2}$$

The ABCD method is validated by using a closure test based on Z+jets MC. The difference between ABCD estimation and pure MC yields can be used to estimate the systematic of the ABCD method. Table 6.1 shows the ABCD method input and results for *ee* channel after 0-jet $p_T^{ll} > 45$ GeV cut. Table 6.2 shows the ABCD method input and results for *ee* channel after 1-jet $\mathbf{p}_{\mathrm{T}}^{\mathrm{tot}}$ veto. Table 6.3 shows the ABCD method input and results for $\mu\mu$ channel after 0-jet $p_T^{ll} > 45$ GeV cut. Table 6.4 shows the ABCD method input and results for $\mu\mu$ channel after 1-jet $\mathbf{p}_{\mathrm{T}}^{\mathrm{tot}}$ veto. Only statistical errors are shown in the tables. In some cases, the numbers from data estimation are higher than the pure MC prediction.

The ratio between A/E (data estimated) and A/E (raw MC) will be used to normalize the DY background in limit setting procedure. The difference between MC expectations and predictions will be used as a systematic for the method.

6.2 W+jets Background Estimation

W+jets events have one lepton, $E_{\mathrm{T}}^{\mathrm{miss}}$ and jets in the final states. The Feynman diagram for W+jets process is shown in Fig. 6.2. It can contribute to the $H\to WW^{(*)}\to \ell\nu\ell\nu$ signal region if any jet can fake as another lepton. Given the huge cross section of W+jets in LHC (Fig. 5.3), the final contribution of W+jets to di-lepton plus $E_{\mathrm{T}}^{\mathrm{miss}}$ selection is not neglectable. The fake process is so complicated that one can not trust the MC simulation. A fake electron can be from decays of (π,

Sample	A	B	C	D	E	F
Data	52.00 ± 7.21	138.00 ± 11.75	124.00 ± 11.14	1213.00 ± 34.83	84.00 ± 9.17	83.00 ± 9.11
ttbar	3.48 ± 1.87	1.34 ± 1.16	5.34 ± 2.31	2.18 ± 1.48	13.01 ± 3.61	5.20 ± 2.28
SingleTop	3.19 ± 1.78	0.42 ± 0.65	2.34 ± 1.53	1.27 ± 1.13	6.14 ± 2.48	1.68 ± 1.30
WW	36.33 ± 6.03	10.66 ± 3.27	26.59 ± 5.16	8.60 ± 2.93	42.54 ± 6.52	22.03 ± 4.69
WZ/ZZ/Wg	4.07 ± 2.02	2.65 ± 1.63	45.75 ± 6.76	14.91 ± 3.86	2.94 ± 1.72	2.51 ± 1.58
Wjets	5.46 ± 2.34	0.00 ± 0.00	7.59 ± 2.76	1.13 ± 1.06	4.91 ± 2.22	4.46 ± 2.11
Zjets	3.77 ± 1.94	104.16 ± 10.21	40.97 ± 6.40	1189.16 ± 34.48	1.74 ± 1.32	54.28 ± 7.37
A (raw MC)			3.77 ± 1.94			
A (closure test)			3.59 ± 0.67			
A (data estimated)			3.77 ± 1.56			
E (raw MC)			1.74 ± 1.32			
E (closure test)			1.87 ± 0.39			
E (data estimated)			1.45 ± 0.67			

Table 6.1 Observed number of events in data and expected yields for the major backgrounds in six regions (A-F) for *ee* channel after 0-jet $p_T^{ll} > 45$ GeV selection. Closure test is done by applying the same ABCD method on $Z + jets$ MC yields directly. The closure test estimation can be compared with estimation using data to get the systematic of this method.

Sample	A	B	C	D	E	F
Data	22.00 ± 4.69	305.00 ± 17.46	118.00 ± 10.86	7206.00 ± 84.89	43.00 ± 6.56	292.00 ± 17.09
ttbar	4.21 ± 2.05	1.74 ± 1.32	6.29 ± 2.51	3.45 ± 1.86	12.46 ± 3.53	8.09 ± 2.84
SingleTop	2.41 ± 1.55	1.07 ± 1.03	2.16 ± 1.47	1.73 ± 1.31	3.41 ± 1.85	3.37 ± 1.84
WW	8.19 ± 2.86	3.54 ± 1.88	8.05 ± 2.84	7.85 ± 2.80	13.88 ± 3.73	15.95 ± 3.99
WZ/ZZ/Wg	2.21 ± 1.49	6.66 ± 2.58	16.54 ± 4.07	25.18 ± 5.02	2.25 ± 1.50	4.43 ± 2.11
Wjets	3.60 ± 1.90	7.61 ± 2.76	0.61 ± 0.78	2.40 ± 1.55	0.00 ± 0.00	3.93 ± 1.98
Zjets	2.98 ± 1.73	359.99 ± 18.97	82.74 ± 9.10	7744.73 ± 88.00	1.66 ± 1.29	242.67 ± 15.58
A (raw MC)			2.98 ± 1.73			
A (closure test)			3.85 ± 0.47			
A (data estimated)			3.35 ± 0.53			
E (raw MC)			1.66 ± 1.29			
E (closure test)			2.59 ± 0.33			
E (data estimated)			3.02 ± 0.49			

Table 6.2 Observed number of events in data and expected yields for the major backgrounds in six regions (A-F) for *ee* channel after 1-jet $\mathbf{p}_{\mathrm{T}}^{\mathrm{tot}}$ veto. Closure test is done by applying the same ABCD method on $Z + jets$ MC yields directly. The closure test estimation can be compared with estimation using data to get the systematic of this method.

Sample	A	B	C	D	E	F
Data	138.00 ± 11.75	364.00 ± 19.08	260.00 ± 16.12	2423.00 ± 49.22	91.00 ± 9.54	142.00 ± 11.92
ttbar	7.21 ± 2.68	2.35 ± 1.53	7.77 ± 2.79	2.88 ± 1.70	15.57 ± 3.95	7.44 ± 2.73
SingleTop	4.65 ± 2.16	1.24 ± 1.11	3.39 ± 1.84	1.22 ± 1.10	7.19 ± 2.68	2.87 ± 1.70
WW	72.25 ± 8.50	15.84 ± 3.98	49.11 ± 7.01	12.99 ± 3.60	72.53 ± 8.52	28.37 ± 5.33
WZ/ZZ/Wg	6.19 ± 2.49	2.83 ± 1.68	74.74 ± 8.65	21.91 ± 4.68	4.29 ± 2.07	2.38 ± 1.54
Wjets	1.03 ± 1.01	0.52 ± 0.72	0.00 ± 0.00	1.13 ± 1.06	0.00 ± 0.00	7.76 ± 2.79
Zjets	16.18 ± 4.02	292.04 ± 17.09	99.20 ± 9.96	2229.22 ± 47.21	2.51 ± 1.59	83.85 ± 9.16
A (raw MC)			16.18 ± 4.02			
A (closure test)			13.00 ± 1.54			
A (data estimated)			17.90 ± 3.05			
E (raw MC)			2.51 ± 1.59			
E (closure test)			3.73 ± 0.56			
E (data estimated)			4.89 ± 1.07			

Table 6.3 Observed number of events in data and expected yields for the major backgrounds in six regions (A-F) for $\mu\mu$ channel after 0-jet $p_T^{ll} > 45$ GeV selection. Closure test is done by applying the same ABCD method on $Z + jets$ MC yields directly. The closure test estimation can be compared with estimation using data to get the systematic of this method.

Sample	A	B	C	D	E	F
Data	38.00 ± 6.16	791.00 ± 28.12	221.00 ± 14.87	13531.00 ± 116.32	53.00 ± 7.28	479.00 ± 21.89
ttbar	8.74 ± 2.96	3.53 ± 1.88	10.33 ± 3.21	5.61 ± 2.37	17.89 ± 4.23	9.97 ± 3.16
SingleTop	4.64 ± 2.15	1.69 ± 1.30	4.18 ± 2.04	1.60 ± 1.26	6.80 ± 2.61	5.32 ± 2.31
WW	16.17 ± 4.02	7.95 ± 2.82	14.88 ± 3.86	12.93 ± 3.60	22.44 ± 4.74	25.46 ± 5.05
WZ/ZZ/Wg	1.32 ± 1.15	1.48 ± 1.22	25.78 ± 5.08	38.54 ± 6.21	1.16 ± 1.08	0.97 ± 0.98
Wjets	1.10 ± 1.05	1.10 ± 1.05	2.79 ± 1.67	0.62 ± 0.79	3.14 ± 1.77	0.58 ± 0.76
Zjets	11.08 ± 3.33	829.10 ± 28.79	194.36 ± 13.94	14313.50 ± 119.64	4.62 ± 2.15	435.56 ± 20.87
A (raw MC)			11.08 ± 3.33			
A (closure test)			11.26 ± 0.90			
A (data estimated)			9.38 ± 1.02			
E (raw MC)			4.62 ± 2.15			
E (closure test)			5.91 ± 0.51			
E (data estimated)			5.29 ± 0.61			

Table 6.4 Observed number of events in data and expected yields for the major backgrounds in six regions (A-F) for $\mu\mu$ channel after 1-jet $\mathbf{p}_{\mathrm{T}}^{\mathrm{tot}}$ veto. Closure test is done by applying the same ABCD method on $Z + jets$ MC yields directly. The closure test estimation can be compared with estimation using data to get the systematic of this method.

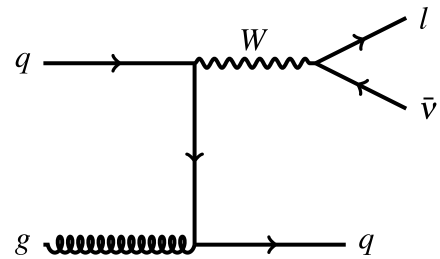

Figure 6.2 Feynman disgram for W+jets process.

K) or from the photon conversion. A fake μ could be a real μ decayed from a heavy quark (s, c, b), in-flight decays of (π, K) and punch-through from calorimeter. That's why a data-driven technique is developed to estimate the W+jets contribution.

6.2.1 Data-driven Method

The W+jets background in signal region is extrapolated from a W+jets enriched control sample multiplied by a fake factor which is measured in multi-jets sample. The estimated W+jets contribution is,

$$N^{SR}_{\text{W+jets}} = f_l \times N^{CR}_{\text{W+jets}}, \tag{6.3}$$

where $N^{SR}_{\text{W+jets}}$ is the number of events for W+jets in signal region, $N^{CR}_{\text{W+jets}}$ is the number of events in W+jets control region, and f_l is lepton fake factor measured in independent sample.

The W+jets control region selection requires one identified (ID) lepton and one anti-ID lepton from real data sample. The rest of kinematic selections are the same with nominal analysis as described in Section 5.6. The contributions of other non-W background (Top, Z, $WW/WZ/ZZ/W\gamma$) are subtracted using corresponding Monte Carlo samples.

The ID lepton definition is the same with main analysis. The anti-ID lepton is defined using loose ID requirement. Anti-ID electron drops the requirement on impact parameter significance

(d_0) cut and loosen the calorimeter cut to $\frac{\text{ETconecorr30}}{p_T} < 0.3$. Anti-ID muon also drops the impact parameter significance requirement and track isolation cut. The calorimeter isolation of anti-ID muon is loosened to $\frac{\text{ETconecorr30}}{p_T} < 0.3$. The anti-ID objects have to pass the anti-ID requirement and fail the ID selection used in main analysis.

6.2.2 Fake Factor Measurement

The lepton fake factor can be measured as,

$$f_l \equiv \frac{N_{\text{ID}}}{N_{\text{anti-ID}}}, \tag{6.4}$$

where N_{ID} ($N_{\text{anti-ID}}$) is the number of ID leptons (anti-ID leptons) in multi-jets sample. The multi-jets events from data is triggered by `EF_g20_etcut` trigger. In order to reduce the contamination from W/Z events, the following cuts are applied to multi-jets sample :

- Z veto : remove events if the invariant mass of two opposite sign same flavor leptons are in Z mass window ($76 < m_{ll} < 106$ GeV).
- W veto : remove events if the transverse mass (calculated from lepton and $E_{\text{T}}^{\text{miss}}$ information) is larger than 30 GeV.

The possible systematic uncertainties sources for fake factor measurement are,

- The trigger bias for the multi-jets samples. The `EF_g20_etcut` trigger is prescalled and the total luminosity for data is about 1.46 pb^{-1}. The systematic from trigger is investigated by switching off the trigger requirement. The difference is taken as the systematic from trigger selection.
- The W/Z contamination in multi-jets samples. The W/Z subtraction is done by Monte Carlo samples. The systematic from this procedure is caused by the W/Z cross section uncertainty. 20% of uncertainty is assigned to the cross section to evaluate the systematic.

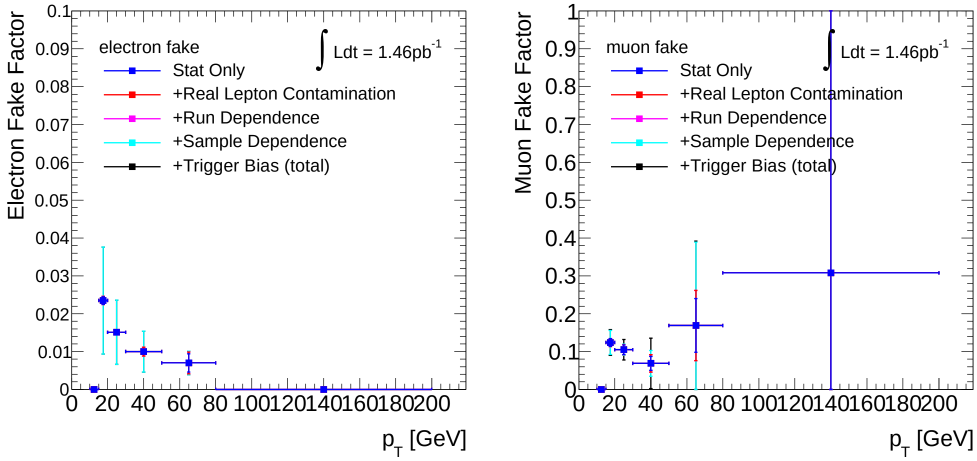

Figure 6.3 The fake factor as a function of p_T including all systematic uncertainties for electrons (left) and muons (right) [3].

- The sample dependent on the fake factor. Currently the fake factor is measured in multi-jets sample and is applied to W+jets control sample. The fake factors can be different in different sample due to lots of unknown reasons. This effect is evaluated using di-jet MC sample and W+jets samples. The difference between fake factor $f_{\text{dijet}}^{\text{MC}}$ and $f_{\text{wjets}}^{\text{MC}}$ is taken as the sample dependent systematic uncertainty.

The fake factors with all the systematic uncertainties in the function of lepton p_T are shown in Fig. 6.3. The data-driven W+jets background estimation is used for all the plots and limit setting. Table 6.5 and Table 6.6 are showing the cutflow comparison between MC W+jets and data-driven estimation W+jets in $H+0$ jet and $H+1$ jet channels. The MC W+jets yields have large statistic error which indicate MC W+jets sample is suffering from lacking statistic. For 0-jet channel, the difference can be 50% at ee and $\mu\mu$ channels. For 1-jet channel, the MC statistic is not enough. And the data-driven estimation for W+jets is quite different with MC prediction.

Channel	Selection	Signal	ttbar	SingleTop	WW	WZ/ZZ/Wg	Zjets	Wjets	WjetsDD	Data
ee	0jet_ZeroJet	6.26 ± 0.08	24.28 ± 1.09	13.87 ± 1.02	138.96 ± 1.85	13.41 ± 1.43	224.21 ± 11.89	28.55 ± 8.25	39.63 ± 0.87	414
	0jet_PtLL	4.38 ± 0.07	20.46 ± 1.00	11.94 ± 0.95	109.07 ± 1.64	9.29 ± 1.07	6.63 ± 1.91	16.50 ± 6.09	17.30 ± 0.53	179
	0jet_mLL	4.01 ± 0.06	3.49 ± 0.48	3.19 ± 0.49	36.37 ± 0.95	4.08 ± 0.80	3.77 ± 1.23	5.46 ± 3.87	7.76 ± 0.38	52
	0jet_deltaPhi	4.00 ± 0.06	3.49 ± 0.48	3.19 ± 0.49	36.32 ± 0.95	4.08 ± 0.80	3.77 ± 1.23	5.46 ± 3.87	7.72 ± 0.38	52
$e\mu$	0jet_ZeroJet	36.14 ± 0.18	107.40 ± 2.23	58.20 ± 2.07	828.13 ± 4.48	66.04 ± 3.36	321.26 ± 11.00	133.93 ± 18.54	166.41 ± 3.13	1567
	0jet_PtLL	33.13 ± 0.18	95.21 ± 2.11	52.15 ± 1.96	693.22 ± 4.09	54.17 ± 2.99	13.90 ± 2.32	104.68 ± 16.34	125.53 ± 2.45	1068
	0jet_mLL	26.75 ± 0.16	15.57 ± 0.91	9.28 ± 0.83	163.57 ± 2.01	24.47 ± 2.34	1.73 ± 0.72	37.17 ± 9.83	40.47 ± 1.37	253
	0jet_deltaPhi	25.67 ± 0.15	15.18 ± 0.90	9.21 ± 0.82	157.35 ± 1.97	23.00 ± 2.25	1.41 ± 0.68	32.43 ± 9.32	35.41 ± 1.25	239
$\mu\mu$	0jet_ZeroJet	14.32 ± 0.12	35.62 ± 1.30	19.33 ± 1.18	262.02 ± 2.48	17.16 ± 0.66	469.59 ± 16.68	11.32 ± 5.11	12.53 ± 1.58	866
	0jet_PtLL	10.20 ± 0.10	29.39 ± 1.17	16.56 ± 1.09	201.82 ± 2.18	13.40 ± 0.58	23.38 ± 3.33	2.15 ± 1.08	3.79 ± 0.83	311
	0jet_mLL	9.37 ± 0.09	7.21 ± 0.60	4.65 ± 0.58	72.33 ± 1.32	6.20 ± 0.41	16.20 ± 2.51	1.03 ± 0.73	1.54 ± 0.52	138
	0jet_deltaPhi	9.34 ± 0.09	7.17 ± 0.60	4.58 ± 0.57	72.23 ± 1.32	6.20 ± 0.41	16.20 ± 2.51	1.03 ± 0.73	1.54 ± 0.52	138

Table 6.5 The number of expected and observed events in $H+0j$ channel including comparison between MC W+jets (Wjets) and data-driven W+jets (WjetsDD). The uncertainties are statistic error only. Signal sample is from $m_H = 125$ GeV Monte Carlo.

Channel	Selection	Signal	ttbar	SingleTop	WW	WZ/ZZ/Wg	Zjets	Wjets	WjetsDD	Data
ee	1jet_OneJet	2.58 ± 0.05	187.79 ± 2.98	51.99 ± 1.98	46.57 ± 1.03	9.14 ± 1.08	53.14 ± 5.35	7.52 ± 3.37	12.39 ± 0.50	366
	1jet_Bjet	2.38 ± 0.04	53.71 ± 1.60	15.71 ± 1.09	43.52 ± 0.99	8.85 ± 1.08	48.30 ± 5.09	7.52 ± 3.37	11.34 ± 0.46	200
	1jet_PtTotal	1.61 ± 0.04	23.65 ± 1.04	8.58 ± 0.81	31.26 ± 0.84	6.54 ± 1.00	10.62 ± 2.28	5.95 ± 3.24	5.17 ± 0.32	94
	1jet_Ztau	1.60 ± 0.04	23.07 ± 1.03	8.19 ± 0.79	30.68 ± 0.84	6.49 ± 1.00	10.02 ± 2.24	5.95 ± 3.24	5.23 ± 0.32	93
	1jet_mLL	1.33 ± 0.03	4.21 ± 0.49	2.41 ± 0.43	8.20 ± 0.43	2.21 ± 0.63	2.39 ± 0.88	3.60 ± 3.02	2.05 ± 0.21	22
	1jet_deltaPhi	1.22 ± 0.03	4.00 ± 0.49	2.34 ± 0.43	7.68 ± 0.42	2.15 ± 0.63	2.16 ± 0.85	3.60 ± 3.02	1.66 ± 0.19	19
$e\mu$	1jet_OneJet	14.74 ± 0.11	853.50 ± 6.30	266.23 ± 4.44	259.54 ± 2.45	39.78 ± 2.38	132.34 ± 5.93	48.74 ± 12.42	64.72 ± 2.42	1678
	1jet_Bjet	13.57 ± 0.10	243.56 ± 3.41	85.60 ± 2.53	241.69 ± 2.35	36.78 ± 2.27	122.54 ± 5.68	46.87 ± 12.38	58.40 ± 2.10	808
	1jet_PtTotal	9.12 ± 0.08	107.66 ± 2.25	48.46 ± 1.90	171.41 ± 1.99	23.94 ± 1.89	67.50 ± 4.28	35.28 ± 12.11	29.23 ± 1.46	449
	1jet_Ztau	9.09 ± 0.08	102.46 ± 2.20	46.35 ± 1.86	166.35 ± 1.96	23.55 ± 1.88	45.77 ± 3.62	35.28 ± 12.11	31.01 ± 1.45	414
	1jet_mLL	6.90 ± 0.07	17.40 ± 0.96	9.25 ± 0.83	31.70 ± 0.86	9.99 ± 1.42	12.44 ± 1.85	18.37 ± 11.30	9.21 ± 0.83	110
	1jet_deltaPhi	6.39 ± 0.07	16.39 ± 0.93	9.04 ± 0.82	28.49 ± 0.81	9.62 ± 1.42	3.09 ± 1.00	18.37 ± 11.30	7.66 ± 0.71	90
$\mu\mu$	1jet_OneJet	5.32 ± 0.06	289.53 ± 3.65	84.72 ± 2.48	86.30 ± 1.39	6.71 ± 0.43	153.95 ± 8.89	7.68 ± 3.16	8.70 ± 1.50	659
	1jet_Bjet	4.92 ± 0.06	84.20 ± 1.99	26.98 ± 1.40	79.89 ± 1.34	6.28 ± 0.41	145.94 ± 8.63	7.68 ± 3.16	6.13 ± 1.21	360
	1jet_PtTotal	3.30 ± 0.05	35.94 ± 1.31	17.14 ± 1.12	55.91 ± 1.13	3.56 ± 0.31	30.41 ± 3.98	5.31 ± 2.93	2.85 ± 0.77	141
	1jet_Ztau	3.30 ± 0.05	35.03 ± 1.30	16.74 ± 1.11	55.28 ± 1.12	3.54 ± 0.31	29.29 ± 3.92	5.31 ± 2.93	3.06 ± 0.77	137
	1jet_mLL	2.70 ± 0.04	8.75 ± 0.68	4.64 ± 0.58	16.17 ± 0.60	1.33 ± 0.20	10.50 ± 2.11	1.10 ± 0.79	1.22 ± 0.46	38
	1jet_deltaPhi	2.49 ± 0.04	8.38 ± 0.66	4.45 ± 0.57	14.87 ± 0.58	1.32 ± 0.20	6.22 ± 1.41	0.45 ± 0.45	0.91 ± 0.40	36

Table 6.6 The number of expected and observed events in $H+1j$ channel including comparison between MC W+jets (Wjets) and data-driven W+jets (WjetsDD). The uncertainties are statistic error only. Signal sample is from $m_H = 125$ GeV Monte Carlo.

The method is also validated in same sign di-lepton region. The distributions in $e\mu$ channel are shown in Fig. 6.4. The same sign region is defined as after $E_{\mathrm{T,rel}}^{\mathrm{miss}}$ cut with two same sign leptons. In that region, W+jets (one fake lepton) and di-boson (real leptons) events dominate. The data MC agreement looks fine.

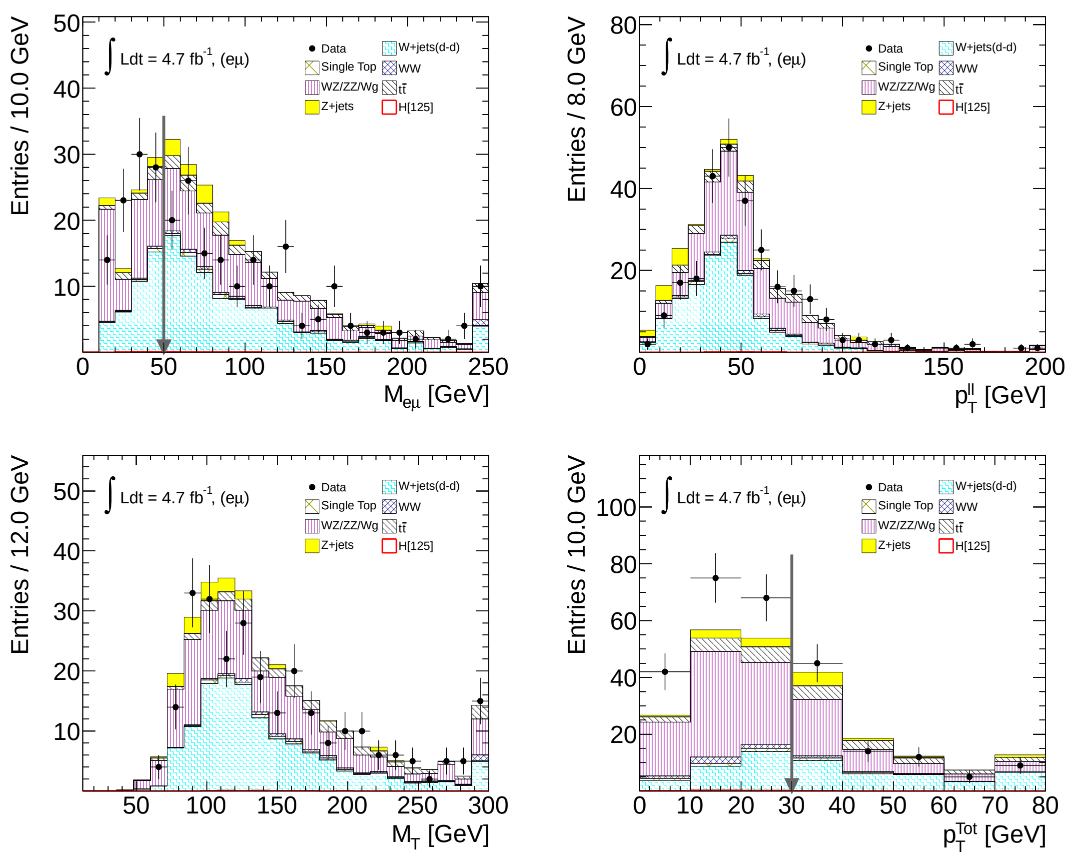

Figure 6.4 Kinematic distributions after $E_{\mathrm{T}}^{\mathrm{miss}}$ with two same sign leptons selections in $e\mu$ channel.

6.3 Top Background

6.3.1 Top Background in $H+0$ Jet

The Top process ($t\bar{t}$ and single Top) will yield two opposite sign leptons, two b-jets and $E_{\mathrm{T}}^{\mathrm{miss}}$ in the final states. It will contribute to the $H+0$ jet signal region if the two b-jets can not pass the jet p_T threshold or are too forward. The method is proposed in [60]. The estimated Top background in $H+0$ jet signal region is,

$$N_{\mathrm{Top}}^{\mathrm{Estimated}}(\ell\ell+E_{\mathrm{T}}^{\mathrm{miss}},0j) = N_{\mathrm{Top}}^{\mathrm{Data}}(\ell\ell+E_{\mathrm{T}}^{\mathrm{miss}}) \times P_2^{\mathrm{Estimated}}, \tag{6.5}$$

where $N_{\mathrm{Top}}^{\mathrm{Data}}(\ell\ell+E_{\mathrm{T}}^{\mathrm{miss}})$ is the number of observed Top events in data without the requirement on jet multiplicity (Top control sample), $P_2^{\mathrm{Estimated}}$ is the jet veto efficiency estimated from a control sample with two leptons, $E_{\mathrm{T}}^{\mathrm{miss}}$ and at least one b-jet in final states (b-tag control sample).

The $N_{\mathrm{Top}}^{\mathrm{Data}}(\ell\ell+E_{\mathrm{T}}^{\mathrm{miss}})$ is obtained by subtracting other non-Top contribution by Monte Carlo in the Top control sample. The $P_2^{\mathrm{Estimated}}$ is the full jet veto efficiency measured in b-tag sample. It should be the square of the jet veto efficiency in b-tag control sample (at least one b-jet) with a correction derived from MC :

$$P_2^{\mathrm{Estimated}} = (P_1^{\mathrm{Btag,Data}})^2 \times \frac{P_2^{\mathrm{MC}}}{(P_1^{\mathrm{Btag,MC}})^2}, \tag{6.6}$$

where P_2^{MC} and $P_1^{\mathrm{Btag,MC}}$ are the quantities in MC. In b-tag control sample, b-jet is defined as the jet which has the highest value of b-tagging weight in that event. Probing jets are defined as the rest of jets whose ΔR with the b-jet is larger than 1. The jet veto efficiency is the ratio between number of events with no probing jet and the total number of events in control sample. The b-jet p_T and η distributions are given in Fig. 6.5.

The ratio of data-driven Top 0-jet ($N_{\mathrm{Top}}^{\mathrm{Estimated}}(\ell\ell+E_{\mathrm{T}}^{\mathrm{miss}},0j)$ and MC yields using the 4.7 fb^{-1} data is,

$$1.038 \pm 0.070(\mathrm{stat}) \pm 0.166(\mathrm{syst}). \tag{6.7}$$

The systematic uncertainty is including 10% from non-Top background substraction (Monte Carlo uncertainty), 3% from jet energy scale, 1.5% from jet energy resolution, 4.8% from b-tagging efficiency and 15% from theoretical error [60]. The ratio will be applied to MC yields in the limit setting.

6.3.2 Top Background in $H+1$ Jet

The Top background in $H+1$ jet channel is normalized by a Top 1-jet control region which is defined by reversing b-jet veto and removing m_{ll} and $\Delta\phi_{ll}$ cuts. The estimated Top background in $H+1$ jet signal region is,

$$N^S_{\text{estimated}} = \alpha_{\text{Top}} \times N^C_{\text{Data}}, \tag{6.8}$$

where $\alpha_{\text{Top}} = \frac{N^S_{MC}}{N^C_{MC}}$ is from MC.

Table 6.7 shows the numbers of expected and observed events in Top 1-jet control region which is a very clean control region. Top events ($t\bar{t}$ and single Top) dominate the control region. The di-lepton invariant mass and m_T distributions are shown in Fig. 6.6.

Channel	Selection	Signal	ttbar	SingleTop	WW	WZ/ZZ/Wg	Zjets	WjetsDD	BG	Data
ee	CR_Top_1jet	0.13 ± 0.01	60.80 ± 1.73	22.18 ± 1.29	2.16 ± 0.24	0.16 ± 0.10	0.72 ± 0.72	0.68 ± 0.15	86.70 ± 2.29	91
$e\mu$	CR_Top_1jet	0.76 ± 0.03	275.05 ± 3.56	109.09 ± 2.84	12.54 ± 0.57	1.50 ± 0.45	4.44 ± 1.14	2.94 ± 0.74	405.56 ± 4.81	426
$\mu\mu$	CR_Top_1jet	0.27 ± 0.02	98.25 ± 2.11	37.22 ± 1.64	4.49 ± 0.33	0.24 ± 0.08	1.34 ± 0.83	1.42 ± 0.62	142.97 ± 2.88	158

Table 6.7 The number of expected and observed events in Top 1-jet control region. The uncertainties are statistic error only.

6.4 WW Background

In low mass Higgs search, WW background in signal region is normalized by WW control region. The WW control region is defined with the same selection as main analysis except that m_{ll} cut is

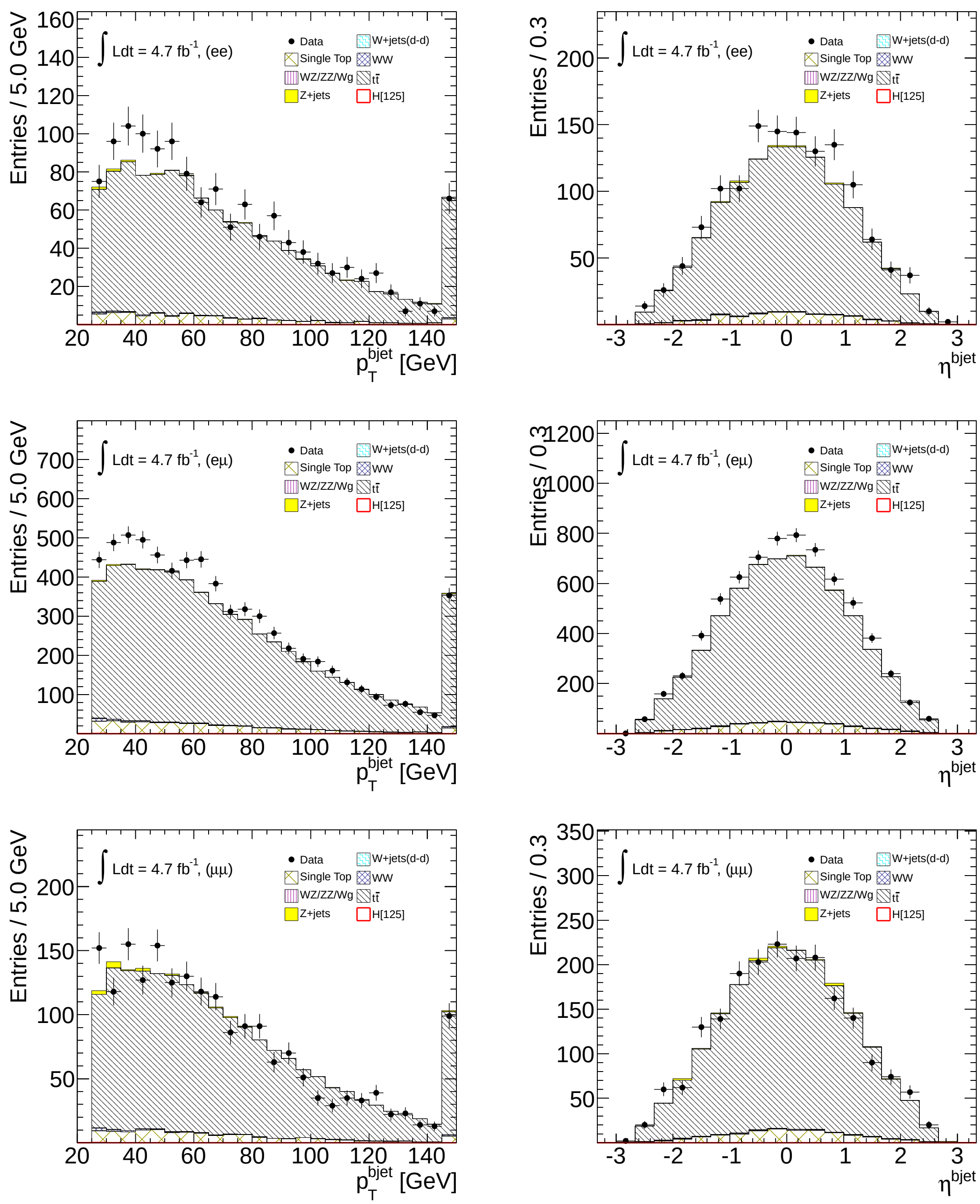

Figure 6.5 b-jet p_T and η distributions in b-tag control samples. It's a clean Top control region.

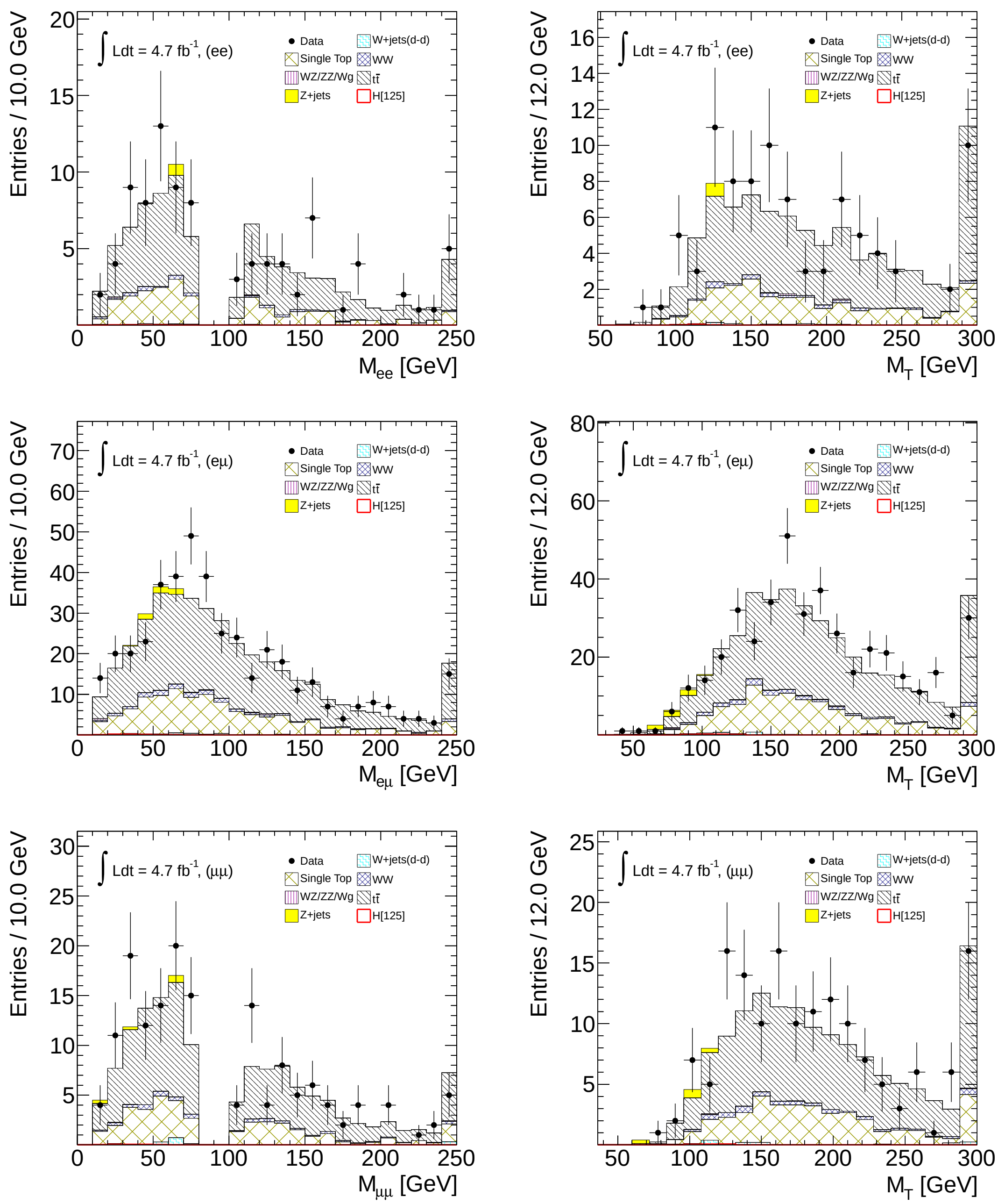

Figure 6.6 Di-lepton invariant mass and m_T distributions in Top 1-jet control region.

changed to $m_{ll} > 80$ GeV and $\Delta\phi_{ll}$ cut is removed. The estimated WW background in signal region is,

$$N^S_{\text{estimated}} = \alpha_{\text{WW}} \times N^C_{\text{Data}}, \tag{6.9}$$

where $\alpha_{\text{WW}} = \frac{N^S_{MC}}{N^C_{MC}}$ is from MC. In intermediate and high mass Higgs search, the WW background estimated using MC yields because it's difficult to find a clean control region in high mass Higgs search.

Table 6.8 and Table 6.9 are the expected and observed events in WW 0-jet and 1-jet control regions. In WW control region, signal ($m_H = 125$ GeV) contribution is tiny. The WW contribution dominate the region. But the Top contamination is not small (27% in $ee+0j$, 17% in $e\mu+0j$, 21% in $\mu\mu+0j$). In limit setting, the Top is also from data driven estimation described in Section 6.3. The W+jets contribution in WW control regions is from data-driven estimation. The di-lepton invariant mass and m_T distributions in WW 0-jet and 1-jet control regions are shown in Fig. 6.7 and Fig. 6.8.

Channel	Selection	Signal	ttbar	SingleTop	WW	WZ/ZZ/Wg	Zjets	WjetsDD	BG	Data
ee	CR_WW_0jet	0.02 ± 0.01	13.02 ± 0.75	6.15 ± 0.68	42.59 ± 1.00	2.95 ± 0.28	1.75 ± 1.23	4.44 ± 0.22	70.89 ± 1.92	84
$e\mu$	CR_WW_0jet	0.24 ± 0.02	58.65 ± 1.62	29.07 ± 1.47	351.26 ± 2.86	18.43 ± 1.40	2.94 ± 1.21	43.46 ± 1.46	503.80 ± 4.30	522
$\mu\mu$	CR_WW_0jet	0.02 ± 0.01	15.59 ± 0.82	7.19 ± 0.72	72.61 ± 1.27	4.29 ± 0.30	2.52 ± 1.27	1.04 ± 0.44	103.24 ± 2.17	91

Table 6.8 The number of expected and observed events in WW 0-jet control region. The uncertainties are statistic error only.

Channel	Selection	Signal	ttbar	SingleTop	WW	WZ/ZZ/Wg	Zjets	WjetsDD	BG	Data
ee	CR_WW_1jet	0.01 ± 0.00	11.90 ± 0.71	3.03 ± 0.49	13.33 ± 0.55	2.21 ± 0.45	1.66 ± 0.96	1.27 ± 0.13	33.39 ± 1.48	42
$e\mu$	CR_WW_1jet	0.10 ± 0.02	60.19 ± 1.64	24.69 ± 1.37	90.61 ± 1.43	8.15 ± 0.88	3.14 ± 0.90	9.69 ± 0.71	196.47 ± 2.95	179
$\mu\mu$	CR_WW_1jet	0.01 ± 0.01	17.04 ± 0.88	6.40 ± 0.69	21.87 ± 0.71	1.14 ± 0.19	4.10 ± 1.59	0.96 ± 0.44	51.51 ± 2.12	49

Table 6.9 The number of expected and observed events in WW 1-jet control region. The uncertainties are statistic error only.

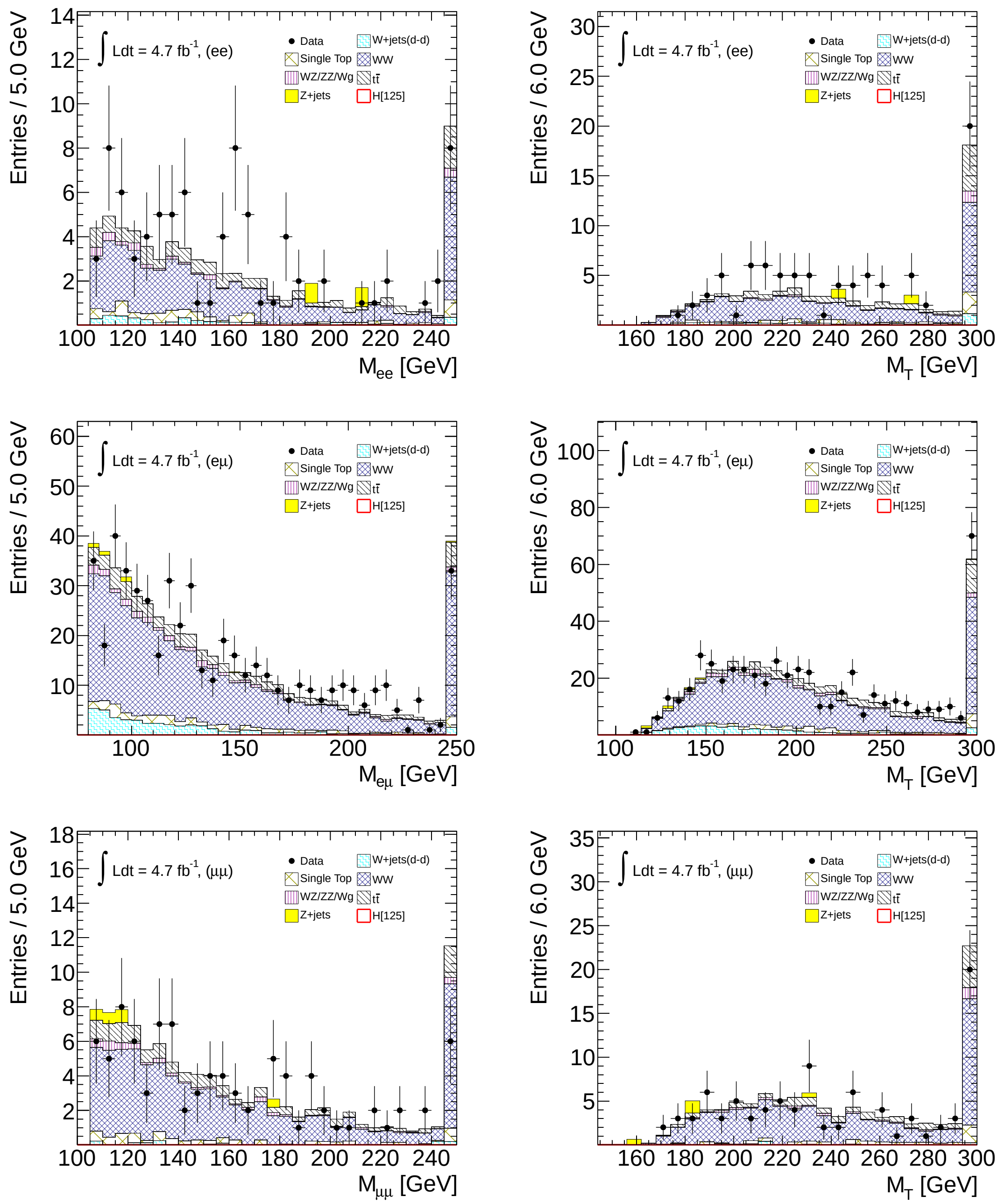

Figure 6.7 Di-lepton invariant mass and m_T distributions in WW 0-jet control region.

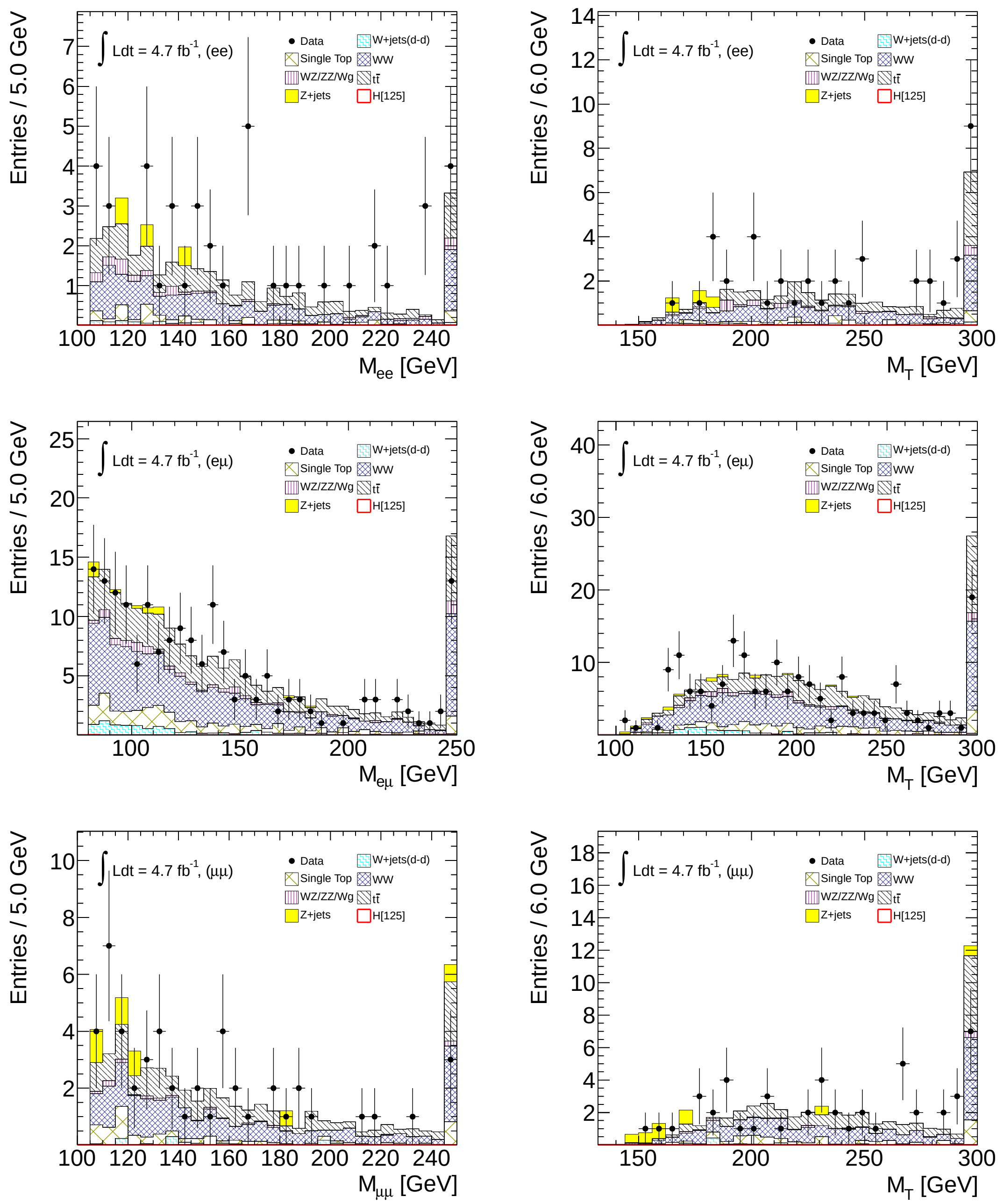

Figure 6.8 Di-lepton invariant mass and m_T distributions in WW 1-jet control region.

Chapter 7

Systematic Uncertainties

Systematic uncertainties considered for $H \rightarrow WW^{(*)} \rightarrow \ell\nu\ell\nu$ analysis includes detector systematic and theoretical systematic. In this chapter, different sources of systematic are described and the effects on the final results are evaluated.

7.1 Electron Systematic

7.1.1 Electron Energy Scale

The electron energy is calibrated with several steps [1]. First, the electronic signal in each calorimeter cell is converted into EM energy which is based on test beam measurement. Second, the energy of topocluster is calibrated using a Monte Carlo based technique to compensate the topocluster energy loss or leakage. Finally, a in-situ calibration, which is using $Z \rightarrow ee$ events, is adopted to further determine the electron energy. The different systematic uncertainties of this procedure are :

1. Additional material : Since the calibration is done by MC-based method, any material which is not taken into account by MC simulation, affects the electron energy.

2. Low transverse energy electrons : The low energy electron is calibrated by $J/\psi \to ee$ and higher energy electron is calibrated using $Z \to ee$. It is found the two calibrations have about 1% difference for the same transverse energy electrons. A 1% systematic is assigned to 10 GeV electrons.

3. Presampler energy scale : The presampler detector is used to correct the energy loss due to upstream material. The energy uncertainty measured in presampler is about 5% in barrel and about 10% in endcap regions up to $|\eta| = 1.8$.

4. Other electronic systematic like calorimeter electronic calibration and cross-talk, non-linearity in the readout electronics and different calorimeter operation condition.

5. Different background fit range and pile-up effects : For $Z \to ee$ calibration, other fit ranges (rather than $80 - 100$ GeV) are used to check the uncertainty. The pile-up effects are estimated using samples with different number of primary vertices.

The electron energy scale uncertainty is propagated into the analysis using Monte Carlo sample by varying the electron energy by $\pm 1\sigma$.

7.1.2 Electron Energy Resolution

The electron energy resolution is constrainted by the calorimeter energy resolution which can be parametrized as

$$\frac{\sigma_E}{E} = \frac{a}{\sqrt{E}} \oplus \frac{b}{E} \oplus c, \tag{7.1}$$

where a is the sampling term, b is the noise term and c is the constant term. Due to the limitation of sample statistics, only constant term is extracted from data. It is also found that the Monte Carlo describes the sampling term very well. And the noise term only contributes at low energy. The electron energy resolution is obtained from a fit to the di-electrons invariant mass distribution by using Breit-Wigner convolved with Crystal Ball function. The definition of Crystal Ball function is,

$$\left.\frac{(\frac{n}{|a|})^n e^{-\frac{1}{2}a^2}}{(\frac{n}{|a|}-|a|-x)^n}\right|_{x<-|a|}, \exp\Big(-\frac{1}{2}(\frac{x-m}{s})^2\Big)\Big|_{x>-|a|}, \tag{7.2}$$

where x is the variable, m, s, a, and n are the parameters of this function. Electrons within $|\eta| < 2.47$ (excluding $1.37 < |\eta| < 1.52$) are called central electrons candidates. Electrons within $2.5 < |\eta| < 4.9$ are called forward electrons candidates. Events with both electrons in central region are defined as central-central events. Events with one electron in central region and another electron in forward region are defined as central-forward events. The m_{ee} ranges vary for central-central events ($80-100$ GeV) and for central-forward events ($70-105$ GeV). The width of Breit-Wigner function will be fixed at Z mass. And the Crystal Ball function will give the electron energy resolution. The systematic uncertainty from electron energy resolution is from the assumption that simulation has the same sampling term with data. This uncertainty is about 0.4% in EM calorimeter and about 1% in forward calorimeter.

The electron energy resolution systematic will be evaluated using Monte Carlo samples. The shape variations due to electron energy resolution in different channels are shown in Fig. 7.1.

7.1.3 Electron Identification and Reconstruction Efficiency

The electron efficiency measurement is using a data-driven tag-and-probe method. The *tag* is defined as a tight ID electron for $Z \to ee$ and $J/\psi \to ee$ measurement. For $W \to e\nu$ measurement, the tag is high $E_{\mathrm{T}}^{\mathrm{miss}}$. The selection cuts can be applied to the *probe* electron which is another electron in the event. This is designed to select a unbiased *probe* electron sample.

The electron identification efficiency is the selection efficiency for electron ID like *medium* and *tight*. The most important systematic uncertainty is from the background subtraction in *probe* sample. The background can be from jet-faked electrons. The uncertainty of discriminating variable for background determination can be the first source of background (m_{ee} for Z events and isolation

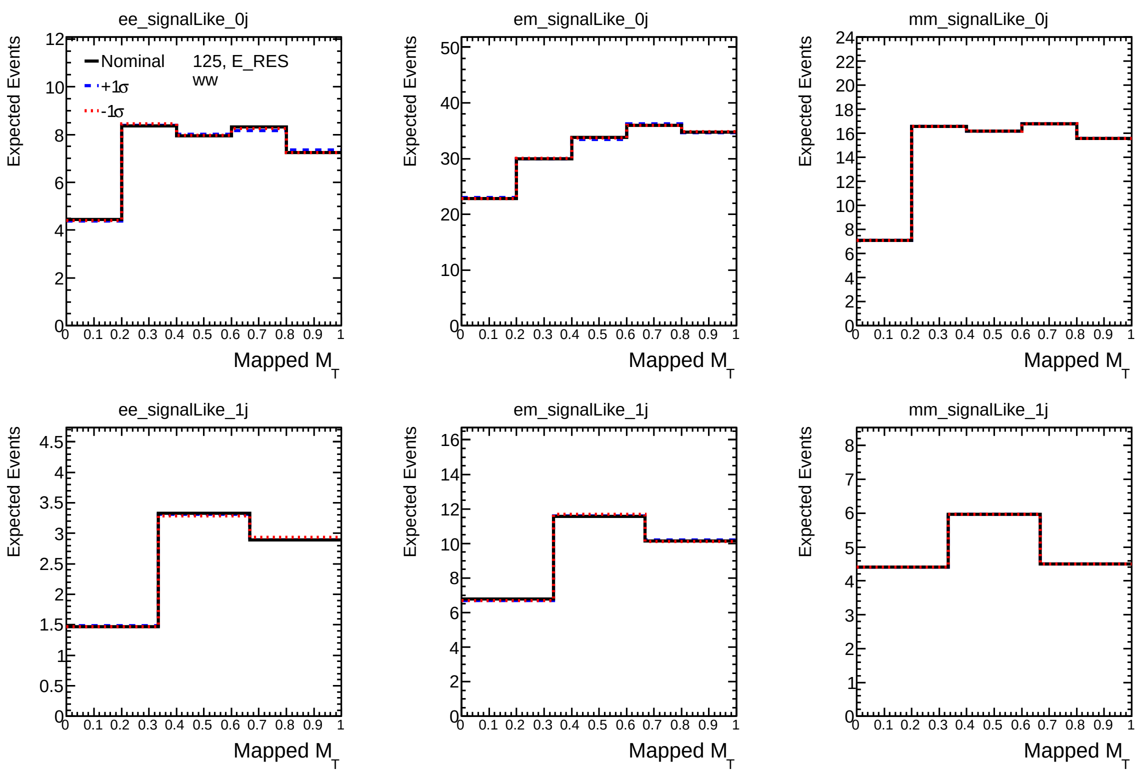

Figure 7.1 The mapped m_T distributions for SM WW background in signal region with electron energy resolution systematics. Only shape variations are shown in plots. The systematic distributions are normalized to the nominal distributions. The binning of m_T is chosen to have a flat total background.

for W events). The second source is the method of background subtraction. The $W \to e\nu$ case, the background modeling uncertainty is obtained by changing the calorimeter isolation criteria.

The electron reconstruction efficiency measures the electron track reconstruction and cluster to track matching efficiency. The electron reconstruction efficiency is also using tag-and-probe method as describe in Section 7.1.2. The possible bias of this measurement is also the background subtraction which is estimated using Monte Carlo closure test.

The electron identification efficiency systematic and electron reconstruction efficiency systematic are treated as uncorrelated error and summed in quadrature.

7.2 Muon Systematic

7.2.1 Muon Momentum Resolution

Muon momentum is measured by the Inner Detector (ID) and Muon Spectrometer (MS) [40]. The muon momentum resolution is related to the track momentum resolution measured in ID and MS. The momentum resolution in MS can be parametrized as

$$\frac{\sigma(p)}{p} = \frac{p_0^{MS}}{p_T} \oplus p_1^{MS} \oplus p_2^{MS} \cdot p_T. \tag{7.3}$$

p_0^{MC}, p_1^{MC} and p_0^{MC} are the coefficients related to energy loss in calorimeter, multiple scattering and intrinsic resolution terms respectively. The ID momentum resolution within $|\eta| < 1.9$ can parametrized as,

$$\frac{\sigma(p)}{p} = p_1^{ID} \oplus p_2^{ID} \cdot p_T, \tag{7.4}$$

where p_1^{ID} and p_2^{ID} are the multiple scattering and intrinsic resolution term. For $|\eta| > 1.9$ region, an additional term $1/\tan^2\theta$ is added into the Eq. 7.4.

There are two methods to measure the resolution. One is using di-muon invariant mass for $Z \to \mu\mu$ events. A convolution of Z lineshape and two Gaussian functions is used to fit the $m_{\mu\mu}$

spectrum. Another method is assign $W \rightarrow \mu\nu$ events in which only one muon is measured. The momentum difference in ID and MS will be used to determine the muon momentum resolution. A combined fitting technique [40] is used for final muon momentum resolution.

The sources of uncertainties can come from the ID multiple scattering term (p_1^{ID}) and alignment of muon chambers in transition region. The first uncertainty is estimated by using fixed p_1^{ID} (expected value) in the combined fitting procedure. The second uncertainty is obtained by removing all the muons within transition region $1.05 < |\eta| < 1.2$ in sample. Fig. 7.2 is showing the MS resolution shape systematic in WW background.

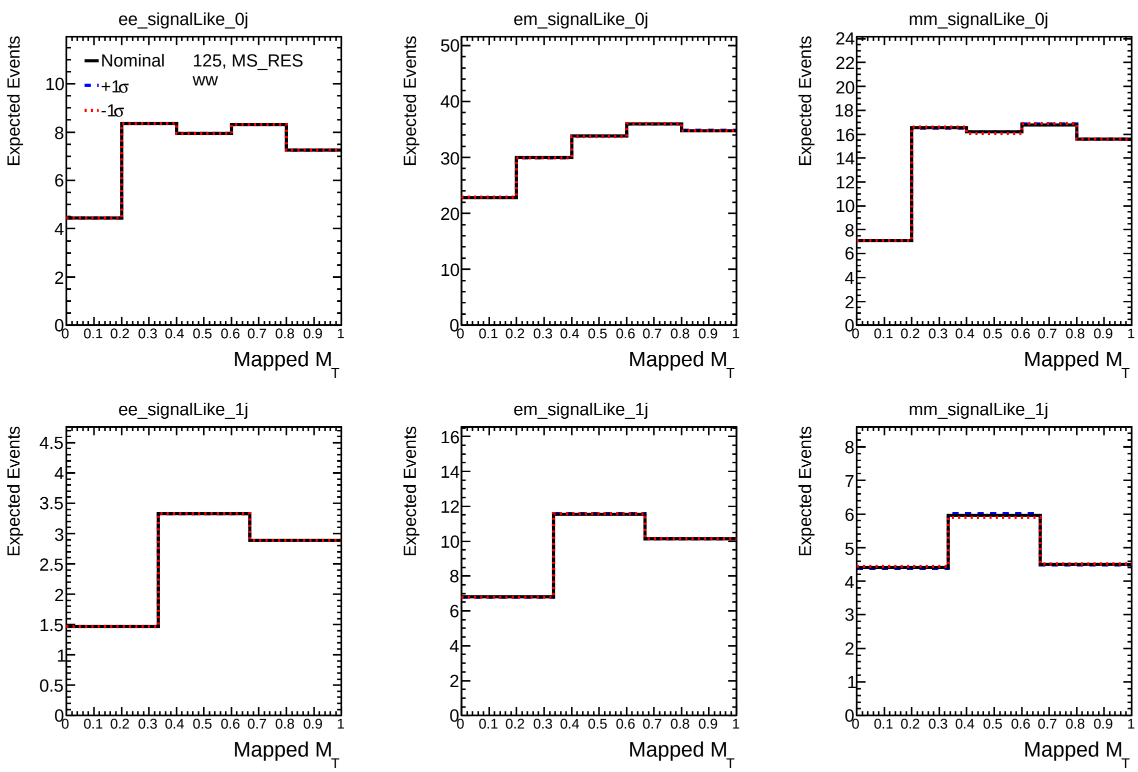

Figure 7.2 The mapped m_T distributions for SM WW background in signal region with muon spectrometer resolution systematics. Only shape variations are shown in plots. The systematic distributions are normalized to the nominal distributions. The binning of m_T is chosen to have a flat total background.

7.2.2 Muon Reconstruction Efficiency

The muon reconstruction efficiency is measured with tag-and-probe method which is mentioned in Section 7.1.3. The method is using $Z \to \mu\mu$ events. One of the muon must be a Combined (CB) muon which is called *tag* muon. The *probe* object should be stand-alone muon to measure ID efficiency. If the MS and matching efficiency is to be measured, the *probe* object must be an inner detector track. The systematic uncertainty is obtained by varying the selection cuts on the Z mass window range and the p_T of *probe* objects within its resolution.

7.3 Jet Systematic

7.3.1 Jet Energy Scale

The jet energy scale (JES) calibration is described in Section 3.2 and in [29]. The baseline calibration for all the jets with $|\eta| > 0.8$ is using the JES uncertainty from $0.3 < |\eta| < 0.8$ region where the detector geometry is better understood and test-beam measurement can be used. The jets in other part of detector will be calibrated with respect to the jets in central region. The sources of JES uncertainties can be :

1. Jet calibration method : The calibration from jet energy response and jet p_T response give different calibration constants. That is because the calibrated jet mass is not close to the truth jet mass. The difference between the two calibrations is taken as a systematic. It is about 2% for jets with $p_T < 30$ GeV and less than 1% for jets with $p_T > 30$ GeV.

2. Detector simulation : The calorimeter cell noise mis-modeling in Monte Carlo simulation and additional detector material. The modeling of fragmentation in Monte Carlo generators is another source of systematic in detector simulation.

3. Calorimeter response : Single particle measurements (single hadron using track response and pion response from test-beam) are used to calibrate the calorimeter response. The uncertainties can be from low p_T particle which does not pass noise thresholds, calorimeter non-linearity and longitudinal leakage, calorimeter response to neutral hadrons.

4. Relative calibration : The uncertainties from *in situ* intercalibration. The method is described in Section 3.3.

5. Pile-up effects : Jets are corrected for pile-up effects which is mentioned in Section 3.2.3. The uncertainty of this procedure can be estimated by measuring jet response in the function of number of primary vertices.

The JES systematic is obtained by varying the p_T of each jet. Fig 7.3 is showing the effect of jet energy scale systematic on the shape of mapped m_T distributions for Z+jets sample. Fig 7.4 is for WW background.

7.3.2 Jet Energy Resolution

The jet energy resolution (JER) can be parametrized as

$$\frac{\sigma_{p_T}}{p_T} = \frac{N}{p_T} \oplus \frac{S}{\sqrt{p_T}} \oplus C, \tag{7.5}$$

where N is the noise term, S is the sampling term and C is the constant term. Two methods are used for JER measurement [61]. One is di-jet balance method which is using QCD di-jet sample. The asymmetry between the two jets are used to determine the JER. The uncertainty from this method is about 8%. The other method, bi-sector method, has about 7% systematic uncertainty for 25 GeV jet. The final systematic affected by JER systematic is evaluated by smearing the jet p_T with 1 σ error for JER measurement. The shape variations for jet energy resolution on $t\bar{t}$ background are shown in Fig. 7.5.

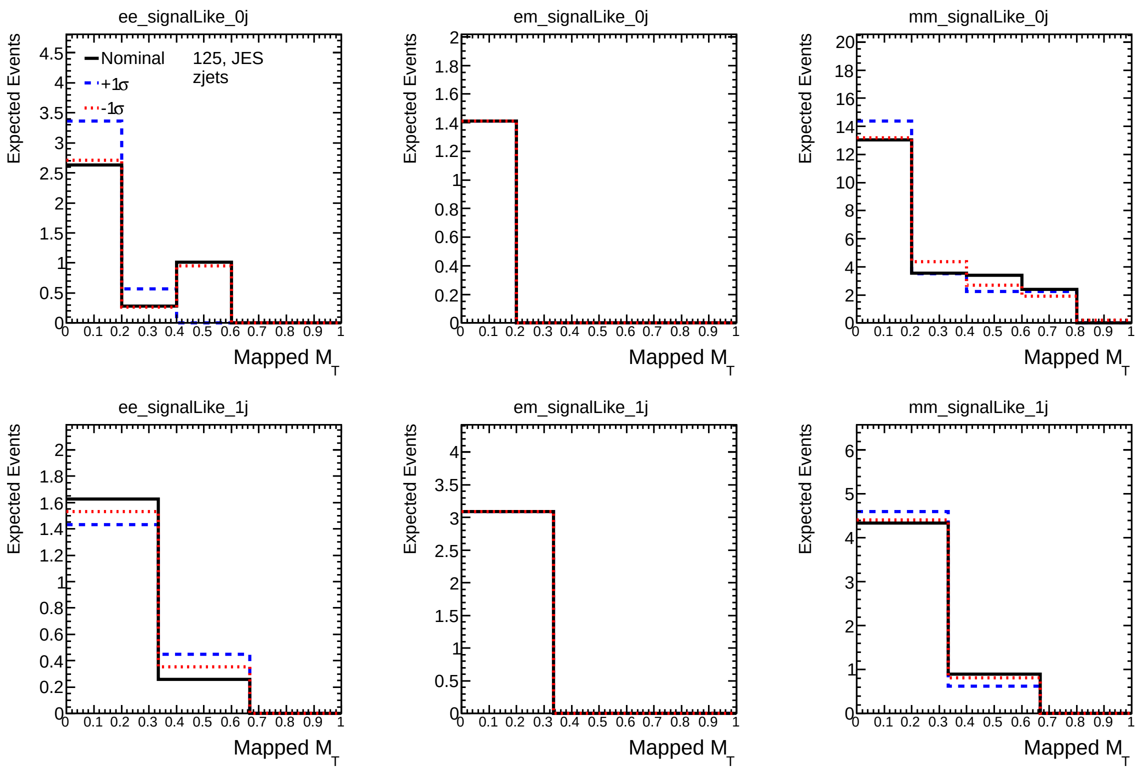

Figure 7.3 The mapped m_T distributions for Z+jets background in signal region with jet energy scale systematics. Only shape variations are shown in plots. The systematic distributions are normalized to the nominal distributions.

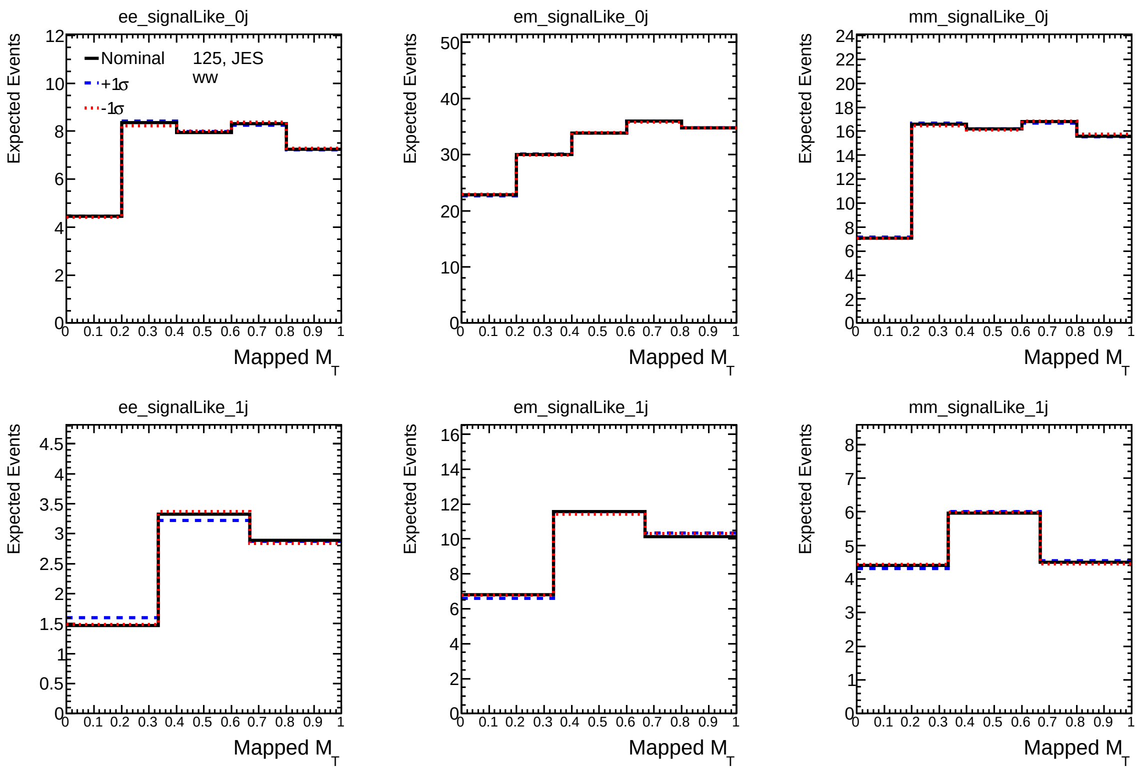

Figure 7.4 The mapped m_T distributions for SM WW background in signal region with jet energy scale systematics. Only shape variations are shown in plots. The systematic distributions are normalized to the nominal distributions.

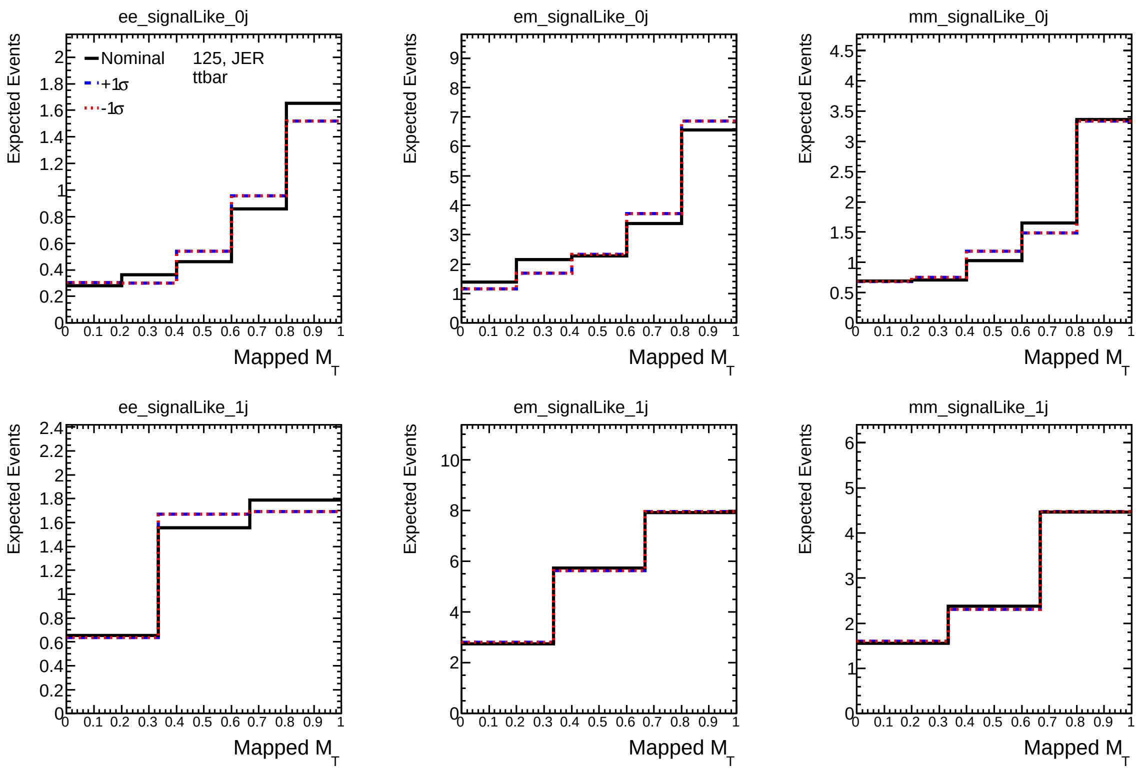

Figure 7.5 The mapped m_T distributions for $t\bar{t}$ background in signal region with jet energy resolution systematics. Only shape variations are shown in plots. The systematic distributions are normalized to the nominal distributions.

7.4 *b*-tagging Efficiency

The *b*-tagging efficiency measurements can be found in [62] and [15]. The *b*-tagging efficiency is defined as

$$\varepsilon_{btag} = \frac{N_{\text{tagged b-jets}}}{N_{\text{b-quark jets}}}, \tag{7.6}$$

where $N_{\text{tagged b-jets}}$ is the number of jets tagged by ATLAS *b*-tagging algorithm and $N_{\text{b-quark jets}}$ is the number *b*-quark jets. The light jets can also be tagged as *b*-jets by mistake which is called mis-tag rate :

$$r_{mistag} = \frac{N_{\text{tagged b-jets}}}{N_{\text{light-quark jets}}}. \tag{7.7}$$

There are different methods to measure *b*-tagging efficiency.

7.4.1 The p_T^{rel} Method

The p_T^{rel} method is using a sample with *b*-jets in which each jet contains a muon. The variable p_T^{rel}, which is defined as the relative momentum of muon with respect to the muon jet axis, is used in this method. Muons from *b*-hadron decays tend to have harder spectrum than muons from light-flavor jets. Fitting templates are obtained from *b*-jet, c-jet and light-flavor jets spectra separately from simulated Monte Carlo. Then relative fractions of different components are obtained by fitting the data using the combined fitting functions. The fraction of *b*-jets before and after the fitting will give the *b*-tag efficiency.

7.4.2 The $System8$ Method

The $system8$ method is using three independent selection criteria on a given sample, which will give eight uncorrelated observables. Those eight observables will be sufficient to solve a system of equations with eight unknowns : the number of *b* and non-*b* jets in given sample, the efficiency for

b and non-b jets to pass each of those three selection criteria. More information about this method can be found in Ref. [63].

In this analysis, the p_T^{rel} and $system8$ methods are combined to get the final b-tagging efficiency uncertainty.

7.4.3 Other Methods

The $D^*\mu$ method is using $b \to X\mu D^* \to X\mu D^0(\to K\pi)\pi$ decay to get a b-jets sample. There are two methods (*Tag Counting* and *Kinematic Selection*) using $t\bar{t}$ sample. The branching ratio of $t \to Wb$ is close to one. So each $t\bar{t}$ event should have two b-jets in before going into detector. *Tag Counting* method is using number of events by selecting zero, one or two b-tagged jets to get the b-tagging efficiency. *Kinematic Selection* method selects the events to get a high-purity $t\bar{t}$ sample. The b-tagging efficiency will be obtained by number of tagged jets and the rest of jets in the event. A inclusive jet sample is used to get the mis-tag rate by two methods, *SV0 mass method* and *negative tag method*. Detail information about the systematic for different methods can be found in [62]. Fig. 7.6 shows the b-tagging efficiency systematic for $t\bar{t}$ background.

7.5 $E_{\mathrm{T}}^{\mathrm{miss}}$

$E_{\mathrm{T}}^{\mathrm{miss}}$ reconstruction is described in Section 4.3. Uncertainties from different $E_{\mathrm{T}}^{\mathrm{miss}}$ terms determine the final $E_{\mathrm{T}}^{\mathrm{miss}}$ systematic. The uncertainties from energy scale and resolution of leptons and hard jets ($p_T^{jet} > 25$ GeV) are propagated to $E_{\mathrm{T}}^{\mathrm{miss}}$. The systematic from $E_{\mathrm{T}}^{\mathrm{miss,CellOut}}$ can be from event generator modeling and calorimeter response. $E_{\mathrm{T}}^{\mathrm{miss,CellOut}}$ is sensitive to the different tunings of underling events and different shower models for hadronic interaction in detector simulation. The calorimeter response uncertainty can be evaluated using single hadron response. The topocluster with different energy scale will lead to different $E_{\mathrm{T}}^{\mathrm{miss,CellOut}}$. And the differences between varia-

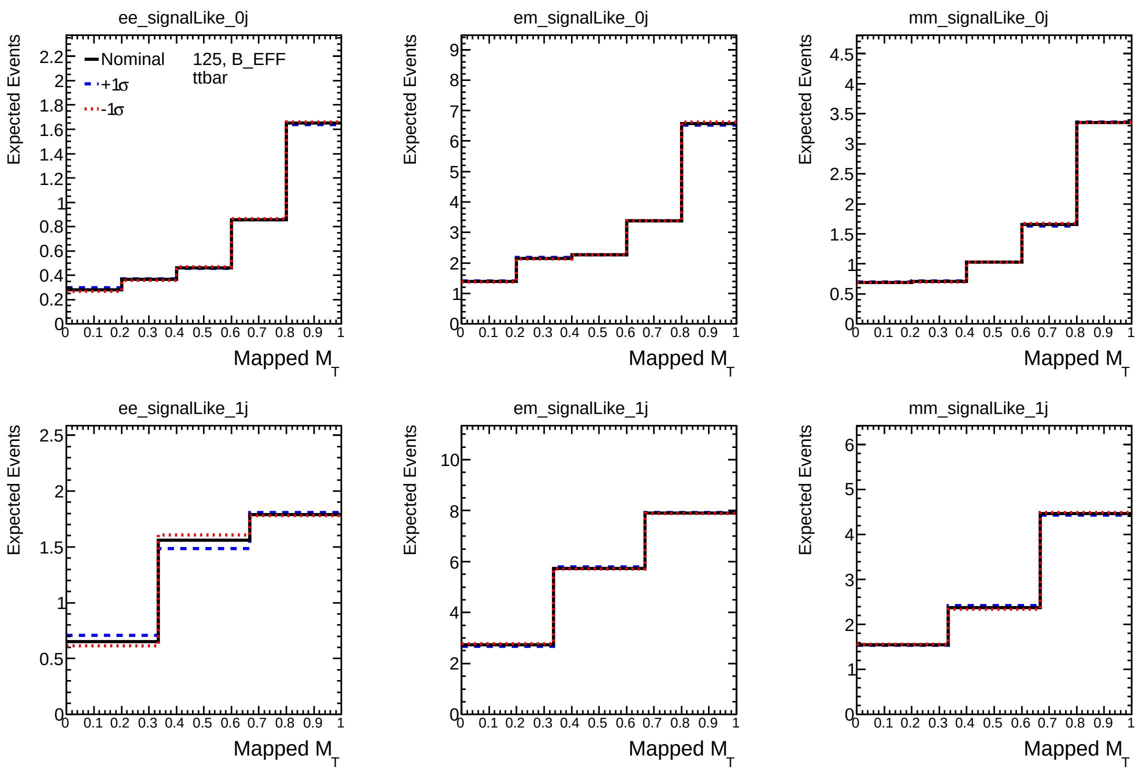

Figure 7.6 The mapped m_T distributions for $t\bar{t}$ background in signal region with b-tagging efficiency systematics. Only shape variations are shown in plots. The systematic distributions are normalized to the nominal distributions.

tions can be considered as systematic uncertainty. The systematic from $E_{\mathrm{T}}^{\mathrm{miss,SoftJets}}$ is estimated using the similar methods [14]. The systematic of $E_{\mathrm{T}}^{\mathrm{miss,CellOut}}$ and $E_{\mathrm{T}}^{\mathrm{miss,SoftJets}}$ for WW background is shown in Fig 7.7. The $E_{\mathrm{T}}^{\mathrm{miss,CellOut}}$ and $E_{\mathrm{T}}^{\mathrm{miss,SoftJets}}$ are combined into `AllClusters` as being fully correlated.

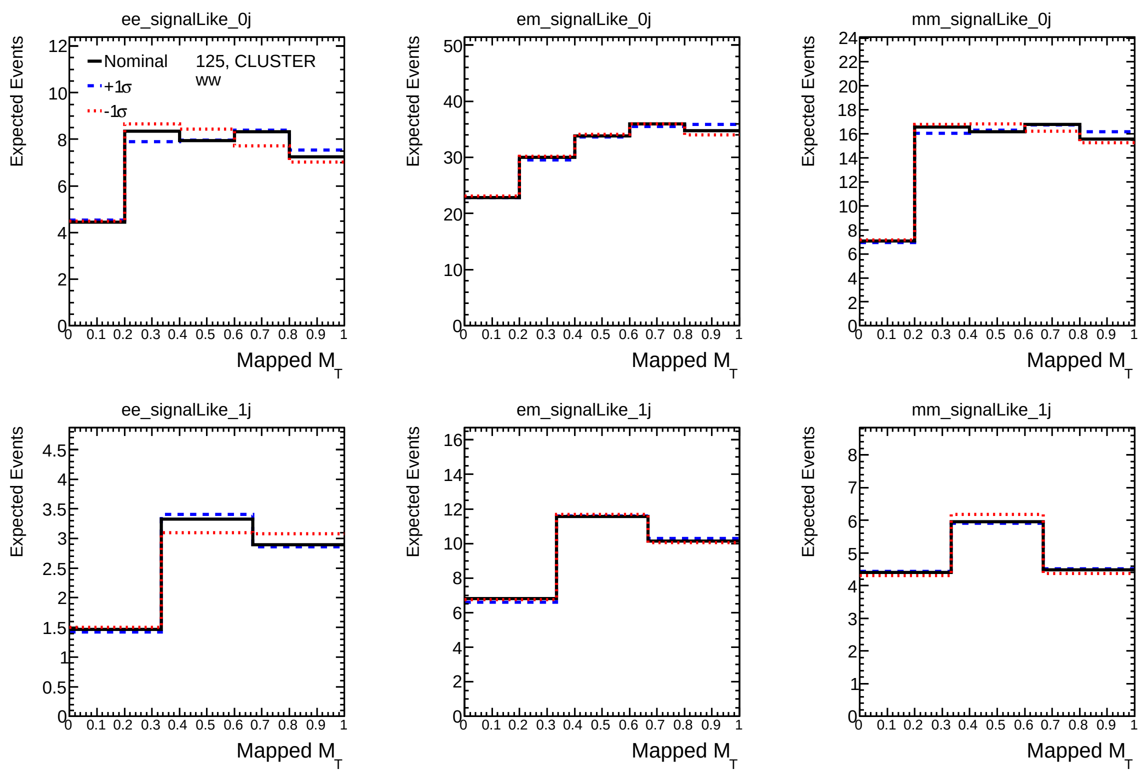

Figure 7.7 The mapped m_T distributions for SM WW background in signal region with $E_{\mathrm{T}}^{\mathrm{miss,CellOut}}$ and $E_{\mathrm{T}}^{\mathrm{miss,SoftJets}}$ systematics. Only shape variations are shown in plots. The systematic distributions are normalized to the nominal distributions. The $E_{\mathrm{T}}^{\mathrm{miss,CellOut}}$ and $E_{\mathrm{T}}^{\mathrm{miss,SoftJets}}$ systematics are combined into `AllClusters` as being fully correlated.

7.6 Trigger

The electron trigger efficiency measurement is using tag-and-probe method [1]. The systematic can come from the background contamination, trigger-offline matching and the probe object definition.

The muon trigger efficiency is also using a tag-and-probe method and the different sources of systematic uncertainty can be found in [64]. The electron and muon trigger efficiency systematic uncertainties are treated as uncorrelated error in $e\mu$ channel.

7.7 Summary Tables for Detector Systematic

The overall normalization systematic effects are show in Table 7.1 for 0-jet channel and Table 7.2 for 1-jet channel, In general, jet energy resolution and jet energy scale systematics have large effects on almost all the samples. The uncertainty on WW background comes from jet systematic and $E_{\mathrm{T}}^{\mathrm{miss}}$ systematic mainly.

7.8 Luminosity Uncertainty

The instantaneous luminosity of a proton-proton collider can be written as,

$$\mathscr{L} = \frac{\mu n_b f_r}{\sigma_{\mathrm{inel}}}, \tag{7.8}$$

where μ is the average number of inelastic interactions per bunch crossing, n_b is the number of colliding bunches, f_r is the machine revolution frequency and σ_{inel} is the proton-proton inelastic cross section. The detector can only measure the visible interactions. Eq. 7.8 can be rewritten as,

$$\mathscr{L} = \frac{\mu_{\mathrm{vis}} n_b f_r}{\sigma_{\mathrm{vis}}}, \tag{7.9}$$

where $\sigma_{\mathrm{vis}} = \varepsilon\sigma_{\mathrm{inel}}$ is the average number of visible interactions per bunch crossing. σ_{vis} is the visible cross section which is measured by *vdM* scan [25]. The uncertainty from different systematic sources are summarized at Table 7.3. The total systematic uncertainty from luminosity measurement is 3.7% [2].

[%]	Signal [125 GeV]	SM WW	WZ/ZZ	$W\gamma$	$t\bar{t}$	Single Top	Z+jets
ElecResolutionDown	0.08	-0.06	0.81	0.97	-0.35	0.41	0.00
ElecResolutionUp	-0.10	-0.01	-0.23	-2.97	0.39	-0.41	-1.17
ElecScaleDown	-0.54	-0.26	0.00	-3.25	-0.19	-0.41	-1.17
ElecScaleUp	0.64	0.11	0.46	1.95	-0.04	0.35	2.81
JERUp	-1.61	-1.63	-0.69	0.69	1.78	1.65	-11.88
JESDown	4.38	3.31	4.73	10.76	25.50	16.78	21.14
JESUp	-5.92	-4.75	-5.08	-3.78	-21.94	-18.67	-28.62
MuonScale	0.44	0.06	1.50	1.83	-0.15	0.00	2.39
MSLOW	-0.03	-0.03	-0.12	0.00	0.00	0.00	0.65
MSUP	0.00	-0.01	-0.12	0.00	0.15	0.00	0.00
IDLOW	-0.05	-0.02	-0.46	0.00	0.15	0.00	0.00
IDUP	0.00	-0.00	0.00	0.00	0.00	0.00	0.65
AllClustersDown	1.51	0.96	1.04	2.72	-0.50	2.94	-8.09
AllClustersUp	-1.51	-0.85	-1.96	-1.54	-0.12	-0.88	19.18
PileUpDown	0.92	0.56	0.81	2.92	-0.46	1.71	-5.10
PileUpUp	-0.92	-0.56	-0.58	-1.91	0.04	0.29	6.74
ElecEffDown	-1.54	-1.45	-1.15	-2.27	-1.43	-1.53	-0.80
ElecEffUp	1.56	1.46	1.27	2.27	1.43	1.59	0.84
MuonEffDown	-1.64	-1.55	-1.85	-1.34	-1.51	-1.41	-2.25
MuonEffUp	1.72	1.55	1.73	1.38	1.55	1.41	2.25
BtagDown	0.00	0.00	0.00	0.00	0.46	0.12	0.00
BtagUp	0.00	0.00	0.00	0.00	-0.46	-0.06	0.00
CtagDown	0.00	0.00	0.00	0.00	0.00	0.00	0.05
CtagUp	0.00	0.00	0.00	0.00	0.00	0.00	-0.09
MtagDown	0.03	0.03	0.00	0.04	0.08	-0.06	0.19
MtagUp	-0.03	-0.03	-0.12	-0.04	-0.12	0.12	-0.19
TriggerDown	-0.67	-0.53	-0.58	-0.89	-0.58	-0.53	-0.89
TriggerUp	0.64	0.52	0.58	0.93	0.54	0.53	0.89

Table 7.1 Normalization variations in percentage due to different detector systematic for signal and backgrounds in 0-jet channel.

[%]	Signal [125 GeV]	SM WW	WZ/ZZ	$W\gamma$	$t\bar{t}$	Single Top	Z+jets
ElecResolutionDown	0.10	-0.18	0.00	-4.18	0.24	0.25	1.83
ElecResolutionUp	0.00	-0.06	0.00	0.00	-0.03	0.19	0.00
ElecScaleDown	-0.30	-0.06	-0.92	-4.18	0.17	-0.38	0.00
ElecScaleUp	0.40	-0.18	0.92	0.00	0.28	0.51	0.00
JERUp	0.59	1.02	-2.45	-3.16	-3.23	-0.19	34.96
JESDown	-5.84	-7.11	0.92	-23.42	11.05	0.44	-4.01
JESUp	5.64	9.87	3.98	-0.31	-13.59	-3.22	19.70
MuonScale	0.30	0.16	0.31	2.65	0.14	-0.19	1.92
MSLOW	0.10	-0.06	0.00	0.00	0.24	0.00	0.00
MSUP	0.00	0.02	0.31	0.00	0.17	0.00	1.92
IDLOW	0.10	-0.02	0.31	0.00	0.00	0.00	0.00
IDUP	0.00	0.06	0.00	0.00	0.17	0.00	0.00
AllClustersDown	7.02	5.53	12.84	1.02	8.45	8.53	3.23
AllClustersUp	-7.81	-5.54	-7.65	-7.64	-9.38	-7.58	14.91
PileUpDown	4.45	3.33	5.50	0.31	5.11	5.12	-8.11
PileUpUp	-5.04	-3.53	-2.45	-9.37	-5.74	-4.17	10.64
ElecEffDown	-1.78	-1.43	-1.53	-2.24	-1.39	-1.39	-1.13
ElecEffUp	1.38	1.45	1.83	2.34	1.43	1.39	1.22
MuonEffDown	-1.58	-1.59	-1.22	-1.22	-1.56	-1.45	-2.01
MuonEffUp	1.68	1.57	1.83	1.22	1.60	1.52	2.01
BtagDown	0.10	0.06	0.00	0.00	16.23	13.01	0.00
BtagUp	-0.10	-0.04	0.00	0.00	-16.06	-13.01	0.00
CtagDown	0.20	0.24	0.61	0.41	0.07	0.06	0.70
CtagUp	-0.30	-0.24	-0.31	-0.41	-0.03	-0.13	-0.70
MtagDown	0.59	0.72	0.61	0.71	0.21	0.38	0.70
MtagUp	-0.59	-0.72	0.00	-0.61	-0.17	-0.38	-0.61
TriggerDown	-0.49	-0.57	0.00	-0.81	-0.52	-0.57	-0.78
TriggerUp	0.59	0.55	0.61	0.81	0.56	0.51	0.78

Table 7.2 Normalization variations in percentage due to different detector systematic for signal and backgrounds in 1-jet channel.

Uncertainty Source	$\delta\mathscr{L}/\mathscr{L}$
vdM Scan Calibration	3.4%
Afterglow Correction	0.2%
Long-term consistency	1.0%
μ Dependence	1.0%
Total	3.7%

Table 7.3 Relative uncertainty on the luminosity calibration [2].

7.9 Theoretical Uncertainties

7.9.1 α_{WW} for WW Background

The analysis is using MC@NLO [52] generator to model the WW background. The first systematic from α_{WW} is the comparison between different generators. Here MCFMv6.0 [65] is used to compare with MC@NLO. The difference is

$$\frac{\alpha(MC@NLO)}{\alpha(MCFM)} = 0.980. \tag{7.10}$$

Different PDF sets are used to get the variation of α_{WW}. Table 7.4 shows the variation of α_{WW} calculated using PDF spanning within the CTEQ6.6 errors. Table 7.5 shows the effect of changing renormalization scale (μ_R) and factorization scale (μ_F) in MC@NLO. More detail about theoretical systematic can be found in Ref. [66].

	CTEQ 6.6 error set
$\alpha_{\rm WW}^{\rm 0j}$	2.5%
$\alpha_{\rm WW}^{\rm 1j}$	2.6%

Table 7.4 The α parameters computed using different PDF sets and spread obtained spanning on the CTEQ6.6 error set [3].

	scale	PDFs	modelling
$\alpha_{\rm WW}^{\rm 0j}$	2.5%	3.7%	3.5%
$\alpha_{\rm WW}^{\rm 1j}$	4%	2.9%	3.5 %

Table 7.5 Scale, PDFs and modelling uncertainties on WW extrapolation parameters α for the NLO $qq, qg \rightarrow WW$ process [3].

.

Chapter 8

Limit Setting

In the analysis of searching new physics, it is necessary to find a statistic procedure to make a quantified estimation on whether observed data is consistent with background only model or observed data is consistent with background plus signal model.

8.1 Statistical Model

The simplest case is event counting analysis with only one channel. The number of observed data should be Possion distribution with mean value,

$$E[n] = \mu s + b, \tag{8.1}$$

where n is the number of observed events, μ is the signal strength parameter and b is the expected number of background events. μ is the parameter of interest in this measurement. The model with $\mu = 0$ is background only model. And the model with $\mu = 1$ is signal plus background model. The other parameters, where are not the purpose of this measurement, are called *nuisance parameters*. The background can be estimated from Monte Carlo generators. But the uncertainties from MC estimation are very large for most of the cases. One needs an auxiliary *control region* measurement.The control region is used to control the background in the signal region. Or one can say the control region is used to contraint the nuisance parameters in this measurement. The number of observed data in control region is Possion distribution with mean value,

$$E[m] = \tau b, \tag{8.2}$$

where τ is the ratio between number of background events in control region and the number of background events in signal region.

The likelihood function for this measurement is,

$$L(\mu,\theta) = \frac{(\mu s+b)^n}{n!}e^{-(\mu s+b)}\frac{(\tau b)^m}{m!}e^{-\tau b}, \tag{8.3}$$

where θ presents all the nuisance parameters. The log-likelihood function is,

$$\ln L(\mu,\theta) = n\ln(\mu s+b)-(\mu s+b)+m\ln(\tau b)-\tau b+C, \tag{8.4}$$

where C is constant term. Since all the channels are statistic independent, it is easy to get the full likelihood function with all channels :

$$L(\mu,\theta) = \prod_i L_i(\mu,\theta_i). \tag{8.5}$$

In $H\to WW^{(*)}\to \ell\nu\ell\nu$ analysis, there are three flavor channels (ee, $e\mu$ and $\mu\mu$), three jet channels (0-jet, 1-jet, 2-jet). The transverse mass spectrum m_T is used for limit setting. In order to reduce the effect of MC statistic limitation, the m_T is binned that the total expected background spectrum is flat in different channels. The number of bins is 5 in 0-jet channel, 3 in 1-jet channel and 1 in 2jet channel due to MC statistics. Therefore, the likelihood function for $H\to WW^{(*)}\to \ell\nu\ell\nu$ is,

$$L(\mu,\theta) = \{\prod_{k=ee,e\mu,\mu\mu}\prod_{j=0}^{N_{jets}}\prod_{i=1}^{N_{bins}}P(N_{ijk}|\mu s_{ijk}+\sum_l^{N_{bg}}b_{ijkl})\}\times\{\prod_{i=1}^{N_\theta}N(\tilde{\theta}|\theta)\}, \tag{8.6}$$

where N_{jets} is the number of jet channels, N_{bins} is the number of bins, N_{ijk} is the number of observed events in signal region, s_{ijk} is the number of expected signal events, b_{ijkl} is the number of expected background events from different type of background, N_{bg} is the number of background types, $N(\tilde{\theta}|\theta)$ is the term for nuisance parameters.

8.2 Test Statistics

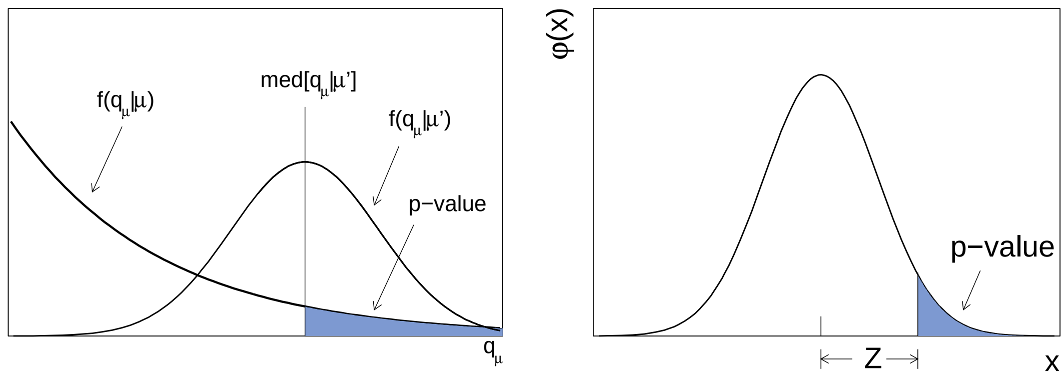

(a) **(b)**

Figure 8.1 (a) Determination of a p-value of a hypothesized value of μ. The area of shaded region is p-value. (b) Illustration of the correspondence between the significance Z and a p-value [17].

The $H \to WW^{(*)} \to \ell\nu\ell\nu$ is using profile likelihood ratio as the test staticstics,

$$\lambda(\mu) = \frac{L(\mu, \hat{\hat{\theta}}(\mu))}{L(\hat{\mu}, \hat{\theta})}, \tag{8.7}$$

where $\hat{\hat{\theta}}$ denotes the value of θ that maximizes L for fixed μ, $\hat{\theta}$ is the maximum-likelihood estimator of θ. If $\lambda(\mu)$ is close to one, it means data has good agreement with the hypothesis with signal strength μ value. Usually the log-likelihood ratio,

$$q_\mu = -2\ln\lambda(\mu), \tag{8.8}$$

is used for convenience. If q_μ is higher, the agreement between data and model is worse. q_μ has a sampling distributions $f(q_\mu|\mu)$. A p-value is defined to quantify the difference between data and model,

$$p_\mu = \int_{q_\mu,obs}^{\infty} f(q_\mu|\mu) dq_\mu, \tag{8.9}$$

where q_μ, obs is the observed test statistics value. This is illustrated in Fig. 8.1a where the shade area is is p-value.

8.2.1 Treatment For Discovery

For discovery, it needs to reject background only hypothesis ($\mu = 0$). The p-value will give the disagreement between observed data and Standard Model only hypothesis,

$$p_0 = \int_{q_{0,obs}}^{\infty} f(q_0|0) dq_0. \tag{8.10}$$

The p-value can be converted to *significance* :

$$Z = \Phi^{-1}(1-p), \tag{8.11}$$

where Φ is the cumulative distribution for standard Gaussian distribution. This is illustrated in Fig. 8.1b.

One can quantify the ability to discover a new model before seeing real data. The *median* significance is obtained with the hypothesis $\mu = 1$.

8.2.2 Treatment For Exclusion

Unfortunately not all the physics search can result a discovery. In this case, one can get the p-value none-zero μ hypothesis to reject them. This is done by getting p-value for different μ. The set of μ with p-value bigger than 1 - CL (confidence level), will be obtained. And the smallest μ is the CL upper limit for one kind of sampling.

If the $\mu \geq 0$, the λ can be rewritten as,

$$\tilde{\lambda}(\mu) = \begin{cases} \frac{L(\mu,\hat{\hat{\theta}}(\mu))}{L(\hat{\mu},\hat{\theta})} & \hat{\mu} \geq 0, \\ \frac{L(\mu,\hat{\hat{\theta}}(\mu))}{L(0,\hat{\hat{\theta}}(0))} & \hat{\mu} < 0 \,, \end{cases} \tag{8.12}$$

For the purpose of upper limit setting, the upward fluctuation of data, which gives $\hat{\mu} > \mu$, will not be counted because it will be compatible with large μ values. The test statistics $\tilde{q}_\mu$ is defined as,

$$\tilde{q}_\mu = \begin{cases} -2\ln\tilde{\lambda}(\mu) & \hat{\mu} \le \mu \\ 0 & \hat{\mu} > \mu \end{cases} = \begin{cases} -2\ln\frac{L(\mu,\hat{\hat{\theta}}(\mu))}{L(0,\hat{\hat{\theta}}(0))} & \hat{\mu} < 0\,, \\ -2\ln\frac{L(\mu,\hat{\hat{\theta}}(\mu))}{L(\hat{\mu},\hat{\theta})} & 0 \le \hat{\mu} \le \mu\,, \\ 0 & \hat{\mu} > \mu\,. \end{cases} \tag{8.13}$$

8.3 CL_s

A modified frequentist method CL_s [67] is used for limit setting. The CL_s is obtained from the ratio of p-values,

$$CL_s = \frac{p_{s+b}}{1-p_b}, \tag{8.14}$$

where p_{s+b} is the p-value for signal plus background sampling distribution and p_b is the p-value for background only hypothesis. Different μ values are used to construct CL_s and the solution of μ for $CL_s = 0.05$ will be the 95% CL upper limit.

8.4 Asymptotic Sampling Distributions

In order to get the p-value of a hypothesis, one has to obtain the sampling distribution $f(q_\mu|\mu)$. Throwing toy MC can generate sampling distributions. But it requires lots of CPU time. For a sufficiently large data sample, the $f(q_\mu|\mu)$ is found to approach [68],

$$f(\tilde{q}_\mu|\mu) = \frac{1}{2}\delta(\tilde{q}_\mu) + \begin{cases} \frac{1}{2}\frac{1}{\sqrt{2\pi}}\frac{1}{\sqrt{\tilde{q}_\mu}}e^{-\tilde{q}_\mu/2} & 0 < \tilde{q}_\mu \le \mu^2/\sigma^2\,, \\ \frac{1}{\sqrt{2\pi}(2\mu/\sigma)}\exp\left[-\frac{1}{2}\frac{(\tilde{q}_\mu+\mu^2/\sigma^2)^2}{(2\mu/\sigma)^2}\right] & \tilde{q}_\mu > \mu^2/\sigma^2\,. \end{cases} \tag{8.15}$$

8.5 Results

No significant excess is found in this analysis with 4.7 fb^{-1} ATLAS data. Fig. 8.2 is showing the upper limits at 95% confidence level for full Higgs mass range. A Standard Model Higgs boson with a mass range from 133 GeV to 258 GeV is excluded at 95% confidence level. The expected exclusion range is from 127 GeV to 233 GeV. A set of private limits results is shown in Appendix B.

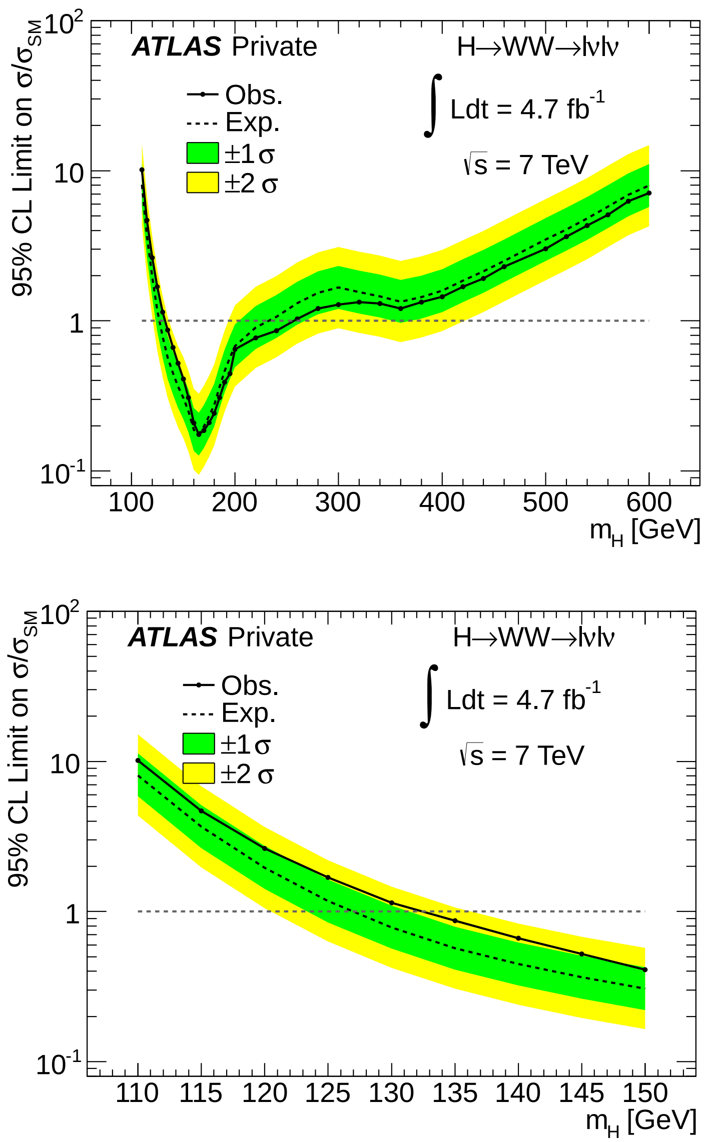

Figure 8.2 Expected (dashed) and observed (solid) 95% CL upper limits on the cross section, normalized to the SM cross section, as a function of m_H. The top plot is for full mass range. The bottom one is regstricted to the range $m_H < 150$ GeV. The green and yellow regions are the $\pm 1\sigma$ and $\pm 2\sigma$ uncertainty bands for expected limit.

Chapter 9

Conclusion and Outlook

A search for the Standard Model Higgs boson decaying two W bosons with di-lepton final states is performed using proton-proton collision data at center-of-mass energy of 7 TeV. The data is collected by ATLAS detector during 2011 and corresponding to an integrated luminosity $4.7\,\mathrm{fb}^{-1}$.

Events with exactly two opposite charge leptons are pre-selected. The data are triggered by single electron or single muon triggers. The leading lepton p_T, which triggers the event, is required to be bigger than 25 GeV. The sub-leading lepton p_T is required to be bigger than 15 GeV. There are five major backgrounds for $H \rightarrow WW^{(*)} \rightarrow \ell\nu\ell\nu$ analysis : QCD multi-jets, W+jets, Drell-Yan, Top and di-boson production. The QCD multi-jets and W+jets events can be an important background if a jet is mis-identified as a lepton. The probability of jet fake as lepton is measured in multi-jets samples and the fate rate is applied to W+jets rich sample. Drell-Yan (γ^*, Z, Υ) background can be suppressed by a di-lepton invariant mass cut ($|m_{ll} - m_Z| > 15$ GeV, $m_{ee} > 12$ GeV, $m_{\mu\mu} > 12$ GeV, and $m_{e\mu} > 10$ GeV). The Drell-Yan background will be further reduced by a $E_{\mathrm{T,rel}}^{\mathrm{miss}}$ cut. The systematics from WW (in zero and one jet channels) and Top one jet backgrounds are constrainted by corresponding control regions. The other di-boson production (WZ, ZZ, $W\gamma$) is estimated by Monte Carlo simulation. The Top quark production in zero jet channel is estimated by a data-driven method.

Limit setting is using profile likelihood ratio as test statistics. CL_s method is used to get the upper limits. No significant excess is found in this analysis with current data. A Standard Model Higgs boson with a mass range from 133 GeV to 258 GeV is excluded at 95% confidence level. The expected exclusion range is from 127 GeV to 233 GeV.

A combination of Standard Model Higgs searches with ATLAS detector is present [69] in which an integrated luminosity of 4.6 to 4.9 fb^{-1} collision data is used. The Standard Model Higgs exclusion ranges are 110 GeV to 117.5 GeV, 118.5 GeV to 122.5 GeV and 129 GeV to 539 GeV. There is an excess at $m_H = 126$ GeV with local significance of 2.5σ. In 2012, Large Hadron Collider will run at center-of-mass energy of 8 TeV. The expected integrated luminosity will be more than 10 fb^{-1}. $H \rightarrow WW^{(*)} \rightarrow \ell\nu\ell\nu$ will continue to play an important role in the low mass Standard Model Higgs search. Hopefully, the low mass Standard Model Higgs can be discovered or excluded with 2012 data.

Appendix A

SVD Unfolding Method

The detector effects can distort the measured spectrum in experiments, like p_T, invariant mass. It is very difficult to compare the experimental measurement and theoretical predictions. In the nominal inclusive jet analysis, a bin-by-bin unfolding method is used. That method is very simple. It takes the ratio of physics truth and the detector simulation spectrum. The ratio will be used to unfold the measurement in experiments. This method doesn't take into account the correlation between different bins. Besides bin-by-bin, Singular Value Decomposition(SVD) is also used in experiments to unfold spectrum. This method was proposed in [70].

A.1 The Unfolding Problem

The measured spectrum of a physical observable is usually distorted by detector effects, such as finite resolution and limited acceptance. A comparison of the measured spectrum with that predicted by theory requires a removal of these effects to obtain the truth, physical spectrum. This is called unfolding.

One can use the equation to describe the problem.

$$\hat{A}x = b \tag{A.1}$$

where x is the truth physics spectrum, $\hat{A}$ is a matrix. b is the measured data. The matrix element $\hat{A}_{ij}$ represents the probability for an event with a true value in bin x_j to be measured with a value in bin b_i.

If your Monte Carlo can describe the detector effects very well, you can use equation to determine the matrix $\hat{A}$.

$$\hat{A}x^{ini} = b^{ini} \tag{A.2}$$

Technically, the matrix element is determined by taking the number of events that falls into bin j of x^{ini} and bin i of b^{ini} at the same time, and by dividing this number by the number of events in bin j of x^{ini}. Then you can use $\hat{A}$ to solve the equation A.1, by applying $x = \hat{A}^{-1}b$. Unfortunately this is a kind of ill-posed problem in mathematics. The result will be nonphysically oscillating. That's why we have to explore the method to solve this problem.

A.2 Singular Value Decomposition

Actually Singular Value Decomposition(SVD) is a method to get the inverse of a matrix. Any real $(n_b \times n_x)$ matrix $\hat{A}$ can be decomposed into a diagonal $(n_b \times n_x)$ matrix S with non-negative elements and two orthogonal matrices U and V.

$$\hat{A} = USV^T,\ \hat{A}^{-1} = VS^{-1}U^T \tag{A.3}$$

Right now you can use

$$x = \hat{A}^{-1}b = VS^{-1}U^T b \tag{A.4}$$

to get your truth spectrum. This is called matrix inverse. If you look at the result, you can find the spectrum is oscillating. In order to find out the effect, we can do this kind of transformation. We can expand b using the matrix U and expand x using matrix V. We can have,

$$Ud = b,\ Vz = x \tag{A.5}$$

You can combine A.4 and A.5.

$$z = V^T x = V^T \hat{A}^{-1} U d = S^{-1} d, \longrightarrow z_i = \frac{d_i}{s_i} \tag{A.6}$$

So you can see the final result is

$$x = Vz = V\frac{d}{S} \tag{A.7}$$

The performance of your final result is related to V, d and S. Small values of S can contribute the oscillation. Then we need regularization to suppress the oscillation.

A.3 Rescaling

If the linear system is (almost) overdetermined, the equation should be treated as least-squares problem.

$$\sum_i ((\hat{A}x)_i - b_i)^2 \rightarrow min. \tag{A.8}$$

We can do this kind of scaling,

$$\omega_j = \frac{x_j}{x_j^{ini}}, \ A_{ij} = \hat{A}_{ij} x_j^{ini} \tag{A.9}$$

And the new system is,

$$A\omega = b \tag{A.10}$$

Then A_{ij} is no longer the probability, but the number of events. At the end of unfolding procedure one has to multiply the unfolding vector ω by x^{ini}.

Since in general, the errors on b are unequal, different equations have different weights for the solution. So it's natural to weight the equation as,

$$\sum_i (\frac{(Ax)_i - b_i}{\Delta b_i})^2 = min. \tag{A.11}$$

In general the Eq. A.11 is,

$$(Ax-b)^T B^{-1} (Ax-b) = min. \tag{A.12}$$

If B is not diagonal, the equations can be scaled like this. Because B is symmetric and positive definite,

$$B = QRQ^T,\ R_{ii} = r_i^2,\ B^{-1} = QR^{-1}Q^T \tag{A.13}$$

Substituting B^{-1} to Eq. A.12, one can rotate and rescale b and A.

$$\tilde{A}_{ij} = \frac{1}{r_i}\sum_i Q_{rim}A_{mj},\ \ \tilde{b}_i = \frac{1}{r_i}\sum_i Q_{im}b_m \tag{A.14}$$

After that, the system we want to solve is,

$$\tilde{A}\omega = \tilde{b} \tag{A.15}$$

The covariance matrix of rescaled equation equals to unit matrix.

A.4 Regularization

If we solve Eq.A.15, the result will still be oscillating. One can use a prior knowledge about the solution to suppress the oscillation. We can add a regularization to the result.

$$(\tilde{A}\omega - \tilde{b})^T(\tilde{A}\omega - \tilde{b}) + \tau(C\omega)^T(C\omega) \rightarrow min. \tag{A.16}$$

C is a matrix which defines the a prior condition on the solution, while the value of regularization parameter τ defines the relative weight of this solution.

Effectively, this expression favors solutions ω that solve the liner system (A.15) and also fulfill the additional condition to have $C\omega$ small.

A.4.1 Determine C

The second derivative of a discrete distribution ω can be defined,

$$\omega_j^{''} = \frac{\omega_{j+1}^{'} - \omega_j^{'}}{\Delta\omega_j} = \frac{1}{(\Delta\omega_j)}\left(\frac{\omega_{j+2} - \omega_{j+1}}{\Delta\omega_{j+1}} - \frac{\omega_j - \omega_j}{\Delta\omega_j}\right) = \frac{1}{(\Delta\omega_j)^2}(\omega_{j+2} - 2\omega_{j+1} + \omega_j) \tag{A.17}$$

One can define the curvature of c of a discrete distribution as the sum of squares its second derivatives,

$$c = \sum_i (\omega_{j+1} - 2\omega_j + \omega_{j-1})^2$$

One can choose

$$C \times \omega = \begin{pmatrix} -1 & 1 & 0 & 0 \\ 1 & -2 & 1 & 0 \\ 0 & 1 & -2 & 1 \\ 0 & 0 & 1 & -1 \end{pmatrix} \times \begin{pmatrix} \omega_1 \\ \omega_2 \\ \omega_3 \\ \omega_4 \end{pmatrix} = \begin{pmatrix} -\omega_1 + \omega_2 \\ \omega_1 - 2\omega_2 + \omega_3 \\ \omega_2 - 2\omega_3 + \omega_4 \\ \omega_3 - \omega_4 \end{pmatrix} \tag{A.18}$$

In general, one can define

$$C = \begin{pmatrix} -1 & 1 & 0 & 0 & \dots & & \\ 1 & -2 & 1 & 0 & \dots & & \\ 0 & 1 & -2 & 1 & \dots & & \\ & \dots & & & \dots & & \\ & \dots & & 1 & -2 & 1 \\ & \dots & & & 1 & -1 \end{pmatrix} \tag{A.19}$$

will suppress solution ω having large curvatures, which leads to a new system.

$$\begin{bmatrix} \tilde{A} \\ \sqrt{\tau} \cdot C \end{bmatrix} w = \begin{bmatrix} \tilde{b} \\ 0 \end{bmatrix}. \tag{A.20}$$

One can use SVD method to solve the equation A.20. In order not to do this for every τ, one can re-define the equation as,

$$\begin{bmatrix} \tilde{A} C^{-1} \\ \sqrt{\tau} \cdot I \end{bmatrix} C w = \begin{bmatrix} \tilde{b} \\ 0 \end{bmatrix}. \tag{A.21}$$

In order to inverse C, one can add a small $\xi \sim 10^{-3}$, or 10^{-4}, to C.

$$C = \begin{pmatrix} -1+\xi & 1 & 0 & 0 & \dots & & \\ 1 & -2+\xi & 1 & 0 & \dots & & \\ 0 & 1 & -2+\xi & 1 & \dots & & \\ & \dots & & & \dots & & \\ & \dots & & 1 & -2+\xi & 1 \\ & \dots & & & 1 & -1+\xi \end{pmatrix} \tag{A.22}$$

Let us now solve the system (A.21) with $\tau = 0$. First, one needs SVD to decompose the product of matrices $\tilde{A}C^{-1}$:

$$\tilde{A}C^{-1} = USV^T. \tag{A.23}$$

U and V are orthogonal and S is diagonal, with non-increasing positive diagonal elements s_i. Rotate both $\tilde{b}$ and Cw to obtain a diagonal system:

$$d \equiv U^T\tilde{b}\,, \qquad z \equiv V^T Cw. \tag{A.24}$$

The system now looks very simple. One can read equations (A.3, A.4, A.5, A.6).

$$s_i \cdot z_i = d_i \tag{A.25}$$

Note that because the covariance matrix of the r.h.s. $\tilde{b}$ was made equal to the unit matrix, the orthogonality of U guarantees that the new rotated r.h.s. d also has a unit covariance matrix, i.e. the equations in (A.25) are completely independent and have identical unit errors in their r.h.s.

Obviously, solving (A.25) one obtains the exact solution of the non-regularized system:

$$z_i^{(0)} = \frac{d_i}{s_i}, \qquad w^{(0)} = C^{-1}Vz^{(0)} \tag{A.26}$$

Introducing non-zero τ is effectively equivalent to changing d_i by a regularized distribution:

$$d_i^{(\tau)} = d_i \frac{s_i^2}{s_i^2 + \tau}, \tag{A.27}$$

so that the solution of the rotated system becomes

$$z_i^{(\tau)} = \frac{d_i s_i}{s_i^2 + \tau}, \qquad w^{(\tau)} = C^{-1} V z^{(\tau)}. \tag{A.28}$$

One can now see how nonzero τ regularizes the singularities due to small s_i's, effectively working as a cutoff for a low-pass filter, if Fourier-transform terminology is used. Indeed, s_i is small when the index i is large, which in general corresponds to quickly oscillating singular vectors (i.e. columns of U and V) defining the new basis in the rotated space.

Because d has a unit covariance matrix, the covariance matrix for z is,

$$Z_{ik}^{(\tau)} = \frac{s_i^2}{(s_i^2 + \tau)^2} \cdot \delta_{ik} \tag{A.29}$$

The property of covariance matrix is,

$$n = M k, \qquad V_n = M V_k M^T \tag{A.30}$$

The covariance matrices W is,

$$W^{(\tau)} = C^{-1} V Z^{(\tau)} V^T C^{T-1} \tag{A.31}$$

Now in order to obtain the true unfolded distribution x and its covariance matrix X one has to multiply w and W by the initial Monte Carlo distribution x^{ini}:

$$x_i^{(\tau)} = x_i^{\text{ini}} w_i^{(\tau)}, \tag{A.32}$$

$$X_{ik}^{(\tau)} = x_i^{\text{ini}} W_{ik}^{(\tau)} x_k^{\text{ini}}. \tag{A.33}$$

A.5 Error Determination

1. You can use the covariance matrix X^τ in Eq. A.33 to get the error of your unfolding results.

$$e_i = \sqrt{X_{ii}^\tau}$$

2. Or you can get the error of your unfolding results by varying the input data spectrum within error.

Appendix B

Private Limits Results

ATLAS Higgs to WW group has produced official ATLAS limits which are shown in Fig. 8.2. I am using my own analysis code to produce another set of results which are shown in Fig. B.1. The two sets of results are very close with each other.

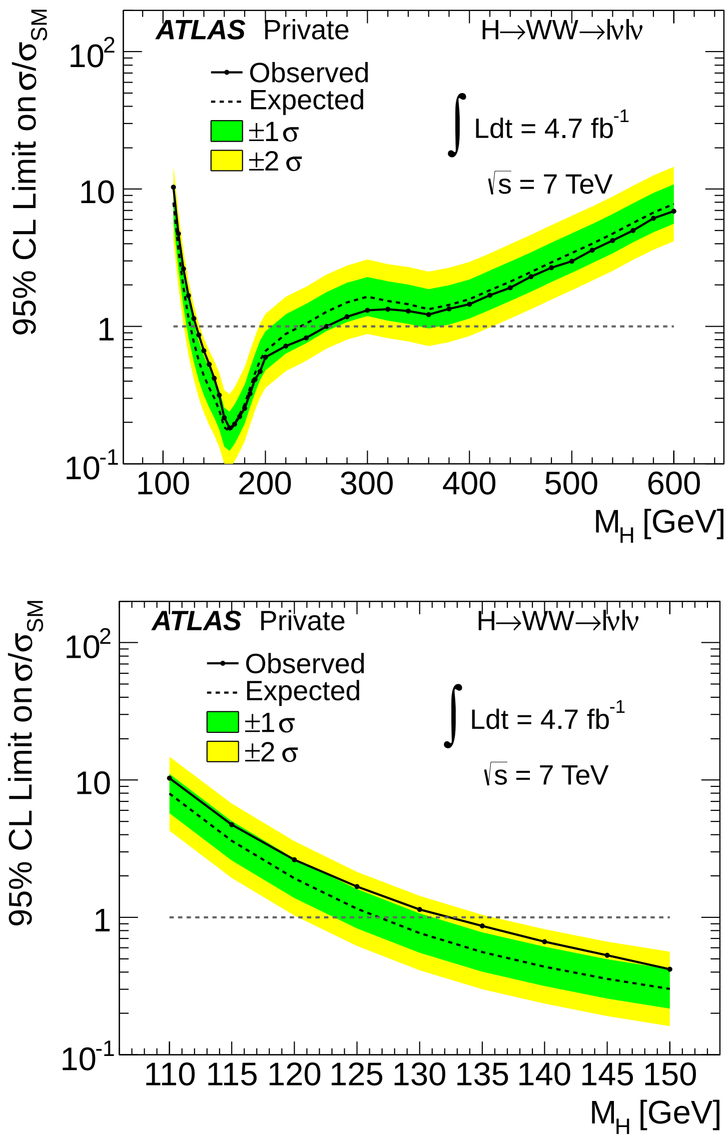

Figure B.1 Expected (dashed) and observed (solid) 95% CL upper limits on the cross section, normalized to the SM cross section, as a function of m_H. The top plot is for full mass range. The bottom one is restricted to the range $m_H < 150$ GeV. The green and yellow regions are the $\pm 1\sigma$ and $\pm 2\sigma$ uncertainty bands for expected limit.

Appendix C

Jet Vertex Fraction Study

The definition of Jet Vertex Fraction (JVF) is discussed in Section 5.5.3. One important feature of LHC physics is that collision events are affected by high pile-up effects. In $H \rightarrow WW^{(*)} \rightarrow \ell\nu\ell\nu$ analysis, one has to rely on Monte Carlo samples to do background estimation or subtraction. Therefore, whether Monte Carlo can describe data especially the pile-up effects in data, is crucial for LHC physics. Fig. C.1 shows the JVF distributions after $E_{\mathrm{T,rel}}^{\mathrm{miss}}$ cut where Top dominates the background. Monte Carlo can not describe data well at region $|JVF| < 0.75$. That is why one needs to cut on JVF to have better data MC agreement. Fig. C.2 shows the average number of jets distributions in the function of primary vertices. With JVF cut, data and Monte Carlo have better agreement in three flavor channels.

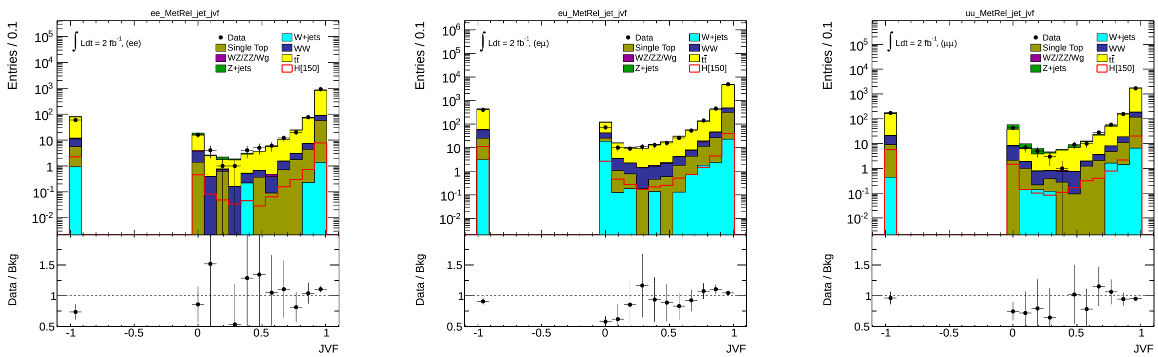

Figure C.1 Jet Vertex Fraction distributions after $E_{\mathrm{T,rel}}^{\mathrm{miss}}$ cut in ee (left), $e\mu$ (middle) and $\mu\mu$ (right) channel. The integrated luminosity of data is 2 fb^{-1}.

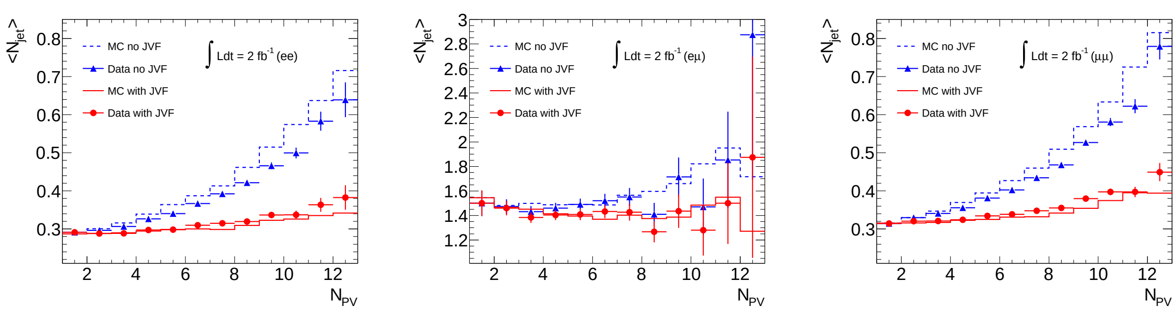

Figure C.2 Average number of jets distributions in the function of number of primary vertices after di-lepton cut in ee (left), $e\mu$ (middle) and $\mu\mu$ (right) channel. The integrated luminosity of data is 2 fb^{-1}.

Bibliography

[1] ATLAS Collaboration Collaboration, G. Aad et al., *Electron performance measurements with the ATLAS detector using the 2010 LHC proton-proton collision data*, Eur.Phys.J. **C72** (2012) 1909, arXiv:1110.3174 [hep-ex]. Long author list - awaiting processing.

[2] *Luminosity Determination in pp Collisions at sqrt(s) = 7 TeV using the ATLAS Detector in 2011*, Tech. Rep. ATLAS-CONF-2011-116, CERN, Geneva, Aug, 2011.

[3] R. Aben et al., *Background estimates in the $H \to WW^{(*)} \to l\nu l\nu$ analysis with 4.7 fb^{-1} of data collected with the ATLAS detector at $\sqrt{s} = 7$ TeV*, Tech. Rep. ATL-COM-PHYS-2011-1728, CERN, Geneva, Dec, 2011.

[4] W.-M. Yao et al, *Review of Particle Physics*, Journal of Physics G **33** (2006) 1+. http://pdg.lbl.gov.

[5] A. Pich, *The Standard model of electroweak interactions*, arXiv:0705.4264 [hep-ph].

[6] A. Djouadi, *The Anatomy of electro-weak symmetry breaking. I: The Higgs boson in the standard model*, Phys.Rept. **457** (2008) 1–216, arXiv:hep-ph/0503172 [hep-ph].

[7] ALEPH and CDF and D0 and DELPHI and L3 and OPAL and SLD and LEP Electroweak Working Group and Tevatron Electroweak Working Group and SLD Electroweak Working

Group and Heavy Flavour Group Collaboration, *Precision Electroweak Measurements and Constraints on the Standard Model*, arXiv:0811.4682 [hep-ex].

[8] LHC Higgs Cross Section Working Group, S. Dittmaier, C. Mariotti, G. Passarino, and R. Tanaka (Eds.), *Handbook of LHC Higgs Cross Sections: 1. Inclusive Observables*, CERN-2011-002 (CERN, Geneva, 2011) , arXiv:1101.0593 [hep-ph].

[9] M. Dobbs, S. Frixione, E. Laenen, K. Tollefson, H. Baer, et al., *Les Houches guidebook to Monte Carlo generators for hadron collider physics*, arXiv:hep-ph/0403045 [hep-ph]. Compiled by the Working Group on Quantum Chromodynamics and the Standard Model.

[10] S. Catani, *Aspects of QCD, from the Tevatron to the LHC*, arXiv:hep-ph/0005233 [hep-ph].

[11] *In-situ pseudo-rapidity inter-calibration to evaluate jet energy scale uncertainty and calorimeter performance in the forward region*, Tech. Rep. ATLAS-CONF-2010-055, CERN, Geneva, Jul, 2010.

[12] ATLAS Collaboration Collaboration, G. Aad et al., *Search for New Physics in the Dijet Mass Distribution using 1 fb-1 of pp Collision Data at sqrt(s) = 7 TeV collected by the ATLAS Detector*, arXiv:1108.6311 [hep-ex].

[13] *Muon reconstruction efficiency in reprocessed 2010 LHC proton-proton collision data recorded with the ATLAS detector*, Tech. Rep. ATLAS-CONF-2011-063, CERN, Geneva, Apr, 2011.

[14] ATLAS Collaboration Collaboration, G. Aad et al., *Performance of Missing Transverse Momentum Reconstruction in Proton-Proton Collisions at 7 TeV with ATLAS*, arXiv:1108.5602 [hep-ex].

[15] *Commissioning of the ATLAS high-performance b-tagging algorithms in the 7 TeV collision data*, Tech. Rep. ATLAS-CONF-2011-102, CERN, Geneva, Jul, 2011.

[16] ATLAS, *ATLAS Physics Summary Plots*, . https://twiki.cern.ch/twiki/bin/view/AtlasPublic/CombinedSummaryPlots.

[17] The ATLAS Collaboration Collaboration, G. Aad et al., *Expected Performance of the ATLAS Experiment - Detector, Trigger and Physics*, `arXiv:0901.0512 [hep-ex]`.

[18] S. Weinberg, *The Quantum Theory of Fields*. Cambridge Univ. Press, Cambridge, 1995.

[19] M. E. Peskin and D. V. Schroeder, *An Introduction to Quantum Field Theory; 1995 ed.* Westview, Boulder, CO, 1995.

[20] P. W. Higgs, *Spontaneous Symmetry Breakdown without Massless Bosons*, Phys.Rev. **145** (1966) 1156–1163.

[21] T. Kibble, *Symmetry breaking in nonAbelian gauge theories*, Phys.Rev. **155** (1967) 1554–1561.

[22] Tevatron New Phenomena Higgs Working Group and CDF and D0 Collaboration Collaboration, G. Bernardi et al., *Combined CDF and D0 Upper Limits on Standard Model Higgs Boson Production at High Mass* $(155 - 200 - GeV/c^{2})$ *with 3* fb^{-1} *of data*, `arXiv:0808.0534 [hep-ex]`.

[23] J. Pumplin, D. Stump, J. Huston, H. Lai, P. M. Nadolsky, et al., *New generation of parton distributions with uncertainties from global QCD analysis*, JHEP **0207** (2002) 012, `arXiv:hep-ph/0201195 [hep-ph]`.

[24] L. Evans and P. Bryant, *LHC Machine*, Journal of Instrumentation **3** (2008) no. 08, S08001. http://stacks.iop.org/1748-0221/3/i=08/a=S08001.

[25] ATLAS Collaboration Collaboration, G. Aad et al., *Luminosity Determination in pp Collisions at sqrt(s)=7 TeV Using the ATLAS Detector at the LHC*, Eur.Phys.J. **C71** (2011) 1630, `arXiv:1101.2185 [hep-ex]`.

[26] ATLAS Collaboration, *ATLAS Detector and Physics Performance: Technical Design Report*, CERN/LHCC/99-14 (1999) . http://atlas.web.cern.ch/Atlas/GROUPS/PHYSICS/TDR/TDR.html.

[27] The ATLAS Collaboration, *The ATLAS Experiment at the CERN Large Hadron Collider*, Journal of Instrumentation **3** (2008) no. 08, S08003. http://stacks.iop.org/1748-0221/3/i=08/a=S08003.

[28] M. Cacciari, G. P. Salam, and G. Soyez, *The Anti-k(t) jet clustering algorithm*, JHEP **0804** (2008) 063, `arXiv:0802.1189 [hep-ph]`.

[29] ATLAS Collaboration Collaboration, *Jet energy measurement with the ATLAS detector in proton-proton collisions at sqrt(s) = 7 TeV*, `arXiv:1112.6426 [hep-ex]`.

[30] T. Sjostrand, S. Mrenna, and P. Z. Skands, *PYTHIA 6.4 Physics and Manual*, JHEP **0605** (2006) 026, `arXiv:hep-ph/0603175 [hep-ph]`.

[31] S. Agostinelli et al., *Geant4 : a simulation toolkit*, Nuclear Instruments and Methods in Physics Research Section A: Accelerators, Spectrometers, Detectors and Associated Equipment **506** (2003) no. 3, 250 – 303. http://www.sciencedirect.com/science/article/pii/S0168900203013688.

[32] Z. Nagy, *Next-to-leading order calculation of three jet observables in hadron hadron collision*, Phys.Rev. **D68** (2003) 094002, `arXiv:hep-ph/0307268 [hep-ph]`.

[33] ATLAS Collaboration Collaboration, G. Aad et al., *Search for New Particles in Two-Jet Final States in 7 TeV Proton-Proton Collisions with the ATLAS Detector at the LHC*, Phys.Rev.Lett. **105** (2010) 161801, `arXiv:1008.2461 [hep-ex]`.

[34] ATLAS Collaboration Collaboration, G. Aad et al., *Search for New Physics in Dijet Mass and Angular Distributions in pp Collisions at $\sqrt{s} = 7$ TeV Measured with the ATLAS Detector*, New J.Phys. **13** (2011) 053044, `arXiv:1103.3864 [hep-ex]`.

[35] T. Han, I. Lewis, and Z. Liu, *Colored Resonant Signals at the LHC: Largest Rate and Simplest Topology*, JHEP **1012** (2010) 085, `arXiv:1010.4309 [hep-ph]`.

[36] J. Alwall, M. Herquet, F. Maltoni, O. Mattelaer, and T. Stelzer, *MadGraph 5 : Going Beyond*, JHEP **1106** (2011) 128, `arXiv:1106.0522 [hep-ph]`.

[37] *ATLAS Monte Carlo tunes for MC09*, Tech. Rep. ATL-PHYS-PUB-2010-002, CERN, Geneva, Mar, 2010.

[38] K. Nakamura et al, *Review of Particle Physics, 2010-2011. Review of Particle Properties*, J. Phys. G **37** (2010) no. 7A, 075021.

[39] *Expected electron performance in the ATLAS experiment*, Tech. Rep. ATL-PHYS-PUB-2011-006, CERN, Geneva, Apr, 2011.

[40] *Muon Momentum Resolution in First Pass Reconstruction of pp Collision Data Recorded by ATLAS in 2010*, Tech. Rep. ATLAS-CONF-2011-046, CERN, Geneva, Mar, 2011.

[41] T. Barillari et al., *Local Hadronic Calibration*, Tech. Rep. ATL-LARG-PUB-2009-001-2. ATL-COM-LARG-2008-006. ATL-LARG-PUB-2009-001, CERN, Geneva, Jun, 2008. Due to a report-number conflict with another document, the report-number ATL-LARG-PUB-2009-001-2 has been assigned.

[42] G. Piacquadio and C. Weiser, *A new inclusive secondary vertex algorithm for b-jet tagging in ATLAS*, Journal of Physics: Conference Series **119** (2008) no. 3, 032032. http://stacks.iop.org/1742-6596/119/i=3/a=032032.

[43] J. Baglio and A. Djouadi, *Higgs production at the lHC*, JHEP **1103** (2011) 055, arXiv:1012.0530 [hep-ph].

[44] P. Nason, *A New method for combining NLO QCD with shower Monte Carlo algorithms*, JHEP **0411** (2004) 040, arXiv:hep-ph/0409146 [hep-ph].

[45] S. Frixione, P. Nason, and C. Oleari, *Matching NLO QCD computations with Parton Shower simulations: the POWHEG method*, JHEP **0711** (2007) 070, arXiv:0709.2092 [hep-ph].

[46] S. Alioli, P. Nason, C. Oleari, and E. Re, *A general framework for implementing NLO calculations in shower Monte Carlo programs: the POWHEG BOX*, JHEP **1006** (2010) 043, arXiv:1002.2581 [hep-ph].

[47] A. Djouadi, J. Kalinowski, and M. Spira, *HDECAY: A Program for Higgs boson decays in the standard model and its supersymmetric extension*, Comput.Phys.Commun. **108** (1998) 56–74, arXiv:hep-ph/9704448 [hep-ph].

[48] D. de Florian, G. Ferrera, M. Grazzini, and D. Tommasini, *Transverse-momentum resummation: Higgs boson production at the Tevatron and the LHC*, JHEP **1111** (2011) 064, arXiv:1109.2109 [hep-ph].

[49] G. Bozzi, S. Catani, D. de Florian, and M. Grazzini, *Transverse-momentum resummation and the spectrum of the Higgs boson at the LHC*, Nucl.Phys. **B737** (2006) 73–120, arXiv:hep-ph/0508068 [hep-ph].

[50] A. D. Martin, W. J. Stirling, R. S. Thorne, and G. Watt, *Parton distributions for the LHC*, Eur. Phys. J. **C63** (2009) 189–285, arXiv:0901.0002 [hep-ph].

[51] A. J. Barr, B. Gripaios, and C. G. Lester, *Measuring the Higgs boson mass in dileptonic W-boson decays at hadron colliders*, JHEP **0907** (2009) 072, arXiv:0902.4864 [hep-ph].

[52] S. Frixione, P. Nason, and B. R. Webber, *Matching NLO QCD and parton showers in heavy flavor production*, JHEP **0308** (2003) 007, arXiv:hep-ph/0305252 [hep-ph].

[53] T. Binoth, M. Ciccolini, N. Kauer, and M. Kramer, *Gluon-induced W-boson pair production at the LHC*, JHEP **0612** (2006) 046, arXiv:hep-ph/0611170 [hep-ph].

[54] B. P. Kersevan and E. Richter-Was, *The Monte Carlo event generator AcerMC version 2.0 with interfaces to PYTHIA 6.2 and HERWIG 6.5*, arXiv:hep-ph/0405247 [hep-ph].

[55] M. L. Mangano, M. Moretti, F. Piccinini, R. Pittau, and A. D. Polosa, *ALPGEN, a generator for hard multiparton processes in hadronic collisions*, JHEP **0307** (2003) 001, arXiv:hep-ph/0206293 [hep-ph].

[56] T. Gleisberg, S. Hoeche, F. Krauss, M. Schonherr, S. Schumann, et al., *Event generation with SHERPA 1.1*, JHEP **0902** (2009) 007, arXiv:0811.4622 [hep-ph].

[57] J. Alwall, P. Demin, S. de Visscher, R. Frederix, M. Herquet, et al., *MadGraph/MadEvent v4: The New Web Generation*, JHEP **0709** (2007) 028, arXiv:0706.2334 [hep-ph].

[58] M. Hance, D. Olivito, and H. Williams, *Performance Studies for e/gamma Calorimeter Isolation*, Tech. Rep. ATL-COM-PHYS-2011-1186, CERN, Geneva, Sep, 2011.

[59] D. W. Miller, A. Schwartzman, and D. Su, *Pile-up jet energy scale corrections using the jet-vertex fraction method*, Tech. Rep. ATL-PHYS-INT-2009-090, CERN, Geneva, Sep, 2009.

[60] B. Mellado, X. Ruan, and Z. Zhang, *Extraction of Top Backgrounds in the Higgs Boson Search with the $H \to WW^{\star} \to \ell\ell + E_{\mathrm{T}}^{\mathrm{miss}}$ Decay with a Full-Jet Veto at the LHC*, Phys.Rev. **D84** (2011) 096005, `arXiv:1101.1383 [hep-ph]`.

[61] *Jet energy resolution and selection efficiency relative to track jets from in-situ techniques with the ATLAS Detector Using Proton-Proton Collisions at a Center of Mass Energy sqrts = 7 TeV*, Tech. Rep. ATLAS-CONF-2010-054, CERN, Geneva, Jul, 2010.

[62] *Calibrating the b-Tag Efficiency and Mistag Rate in 35 pb^{-1} of Data with the ATLAS Detector*, Tech. Rep. ATLAS-CONF-2011-089, CERN, Geneva, Jun, 2011.

[63] *b-Jet Tagging Efficiency Calibration using the System8 Method*, Tech. Rep. ATLAS-CONF-2011-143, CERN, Geneva, Oct, 2011.

[64] *A measurement of the ATLAS muon reconstruction and trigger efficiency using J/psi decays*, Tech. Rep. ATLAS-CONF-2011-021, CERN, Geneva, Mar, 2011.

[65] C. W. John Campbell, Keith Ellis, *MCFM - Monte Carlo for FeMtobarn processes*, . http://mcfm.fnal.gov/.

[66] R. Aben et al., *Monte Carlo generators and theoretical aspects for the search of the Higgs boson in the $H \to WW^{(*)} \to l\nu l\nu$ decay mode using 4.7 fb^{-1} of data collected with the ATLAS detector at $\sqrt{s} = 7$ TeV*, Tech. Rep. ATL-COM-PHYS-2011-1726, CERN, Geneva, Dec, 2011.

[67] A. L. Read, *Presentation of search results: The CL(s) technique*, J.Phys.G **G28** (2002) 2693–2704.

[68] G. Cowan, K. Cranmer, E. Gross, and O. Vitells, *Asymptotic formulae for likelihood-based tests of new physics*, The European Physical Journal C - Particles and Fields **71** (2011) 1–19. http://dx.doi.org/10.1140/epjc/s10052-011-1554-0. 10.1140/epjc/s10052-011-1554-0.

[69] *An update to the combined search for the Standard Model Higgs boson with the ATLAS detector at the LHC using up to 4.9 fb^{-1} of pp collision data at sqrt(s) = 7 TeV*, Tech. Rep. ATLAS-CONF-2012-019, CERN, Geneva, Mar, 2012.

[70] A. Hocker and V. Kartvelishvili, *SVD approach to data unfolding*, Nucl.Instrum.Meth. **A372** (1996) 469–481, `arXiv:hep-ph/9509307 [hep-ph]`.

List of Publications

[1] ATLAS Collaboration Collaboration, G. Aad et al., *Measurement of inclusive jet and dijet production in pp collisions at sqrt(s) = 7 TeV using the ATLAS detector*, arXiv:1112.6297 [hep-ex]. Accpected by PRD. **[Main Contribution]**.

[2] ATLAS Collaboration Collaboration, G. Aad et al., *Search for the Higgs boson in the $H \to WW(*) \to l\nu l\nu$ decay channel in pp collisions at sqrts = 7 TeV with the ATLAS detector*, Phys.Rev.Lett. **108** (2012) 111802, arXiv:1112.2577 [hep-ex]. **[Main Contribution]**.

[3] ATLAS Collaboration Collaboration, G. Aad et al., *Search for New Physics in the Dijet Mass Distribution using 1 fb^{-1} of pp Collision Data at sqrt(s) = 7 TeV collected by the ATLAS Detector*, Phys.Lett. **B708** (2012) 37–54, arXiv:1108.6311 [hep-ex]. **[Main Contribution]**.

[4] ATLAS Collaboration Collaboration, G. Aad et al., *Search for New Physics in Dijet Mass and Angular Distributions in pp Collisions at $\sqrt{s} = 7$ TeV Measured with the ATLAS Detector*, New J.Phys. **13** (2011) 053044, arXiv:1103.3864 [hep-ex]. **[Main Contribution]**.

[5] ATLAS Collaboration Collaboration, G. Aad et al., *Search for New Particles in Two-Jet Final States in 7 TeV Proton-Proton Collisions with the ATLAS Detector at the LHC*,

Phys.Rev.Lett. **105** (2010) 161801, arXiv:1008.2461 [hep-ex]. **[Main Contribution]**.

[6] Atlas Collaboration Collaboration, G. Aad et al., *Measurement of inclusive jet and dijet cross sections in proton-proton collisions at 7 TeV centre-of-mass energy with the ATLAS detector*, Eur.Phys.J. **C71** (2011) 1512, arXiv:1009.5908 [hep-ex]. **[Main Contribution]**.

[7] H.-F. Li, H.-l. Li, Z.-G. Si, and Z.-J. Yang, *Unparticle Effects on Top Quark Pair Production at Photon Collider*, Commun.Theor.Phys. **51** (2009) 707–712, arXiv:0802.0236 [hep-ph]. **[Main Contribution]**.

[8] ATLAS Collaboration Collaboration, G. Aad et al., *Search for the Standard Model Higgs boson in the decay channel $H \to ZZ(*) \to 4l$ with 4.8 fb-1 of pp collision data at sqrt(s) = 7 TeV with ATLAS*, Phys. Lett. **B710** (2012) 383–402, arXiv:1202.1415 [hep-ex].

[9] ATLAS Collaboration Collaboration, G. Aad et al., *Search for the Standard Model Higgs boson in the diphoton decay channel with 4.9 fb-1 of pp collisions at sqrt(s)=7 TeV with ATLAS*, Phys.Rev.Lett. **108** (2012) 111803, arXiv:1202.1414 [hep-ex].

[10] ATLAS Collaboration Collaboration, G. Aad et al., *Combined search for the Standard Model Higgs boson using up to 4.9 fb-1 of pp collision data at sqrt(s) = 7 TeV with the ATLAS detector at the LHC*, Phys.Lett. **B710** (2012) 49–66, arXiv:1202.1408 [hep-ex].

[11] ATLAS Collaboration Collaboration, G. Aad et al., *Rapidity gap cross sections measured with the ATLAS detector in pp collisions at sqrt(s) = 7 TeV*, Eur.Phys.J. **C72** (2012) 1926, arXiv:1201.2808 [hep-ex].

[12] ATLAS Collaboration Collaboration, G. Aad et al., *Search for anomalous production of prompt like-sign muon pairs and constraints on physics beyond the Standard Model with the ATLAS detector*, Phys.Rev. **D88** (2012) 032004, arXiv:1201.1091 [hep-ex].

[13] ATLAS Collaboration Collaboration, G. Aad et al., *Search for first generation scalar leptoquarks in pp collisions at sqrts=7 TeV with the ATLAS detector*, Phys.Lett. **B709** (2012) 158–176, arXiv:1112.4828 [hep-ex].

[14] ATLAS Collaboration Collaboration, G. Aad et al., *Measurement of $D^{*+/-}$ meson production in jets from pp collisions at sqrt(s) = 7 TeV with the ATLAS detector*, Phys. Rev. **D85** (2012) 052005, arXiv:1112.4432 [hep-ex].

[15] ATLAS Collaboration Collaboration, G. Aad et al., *Search for Extra Dimensions using diphoton events in 7 TeV proton-proton collisions with the ATLAS detector*, Phys. Lett. **B710** (2012) 538–556, arXiv:1112.2194 [hep-ex].

[16] ATLAS Collaboration Collaboration, G. Aad et al., *Measurement of the WZ production cross section and limits on anomalous triple gauge couplings in proton-proton collisions at sqrt(s) = 7 TeV with the ATLAS detector*, Phys.Lett. **B709** (2012) 341–357, arXiv:1111.5570 [hep-ex].

[17] ATLAS Collaboration Collaboration, G. Aad et al., *Search for Diphoton Events with Large Missing Transverse Momentum in 1 $fb^{-}1$ of 7 TeV Proton-Proton Collision Data with the ATLAS Detector*, Phys. Lett. **B710** (2012) 519–537, arXiv:1111.4116 [hep-ex].

[18] ATLAS Collaboration Collaboration, G. Aad et al., *Measurement of the production cross section for Z/gamma* in association with jets in pp collisions at sqrt(s) = 7 TeV with the ATLAS detector*, Phys.Rev. **D85** (2012) 032009, arXiv:1111.2690 [hep-ex].

[19] ATLAS Collaboration Collaboration, G. Aad et al., *Kshort and Lambda production in pp interactions at sqrt(s) = 0.9 and 7 TeV measured with the ATLAS detector at the LHC*, Phys.Rev. **D85** (2012) 012001, arXiv:1111.1297 [hep-ex].

[20] ATLAS Collaboration Collaboration, G. Aad et al., *Search for strong gravity signatures in same-sign dimuon final states using the ATLAS detector at the LHC*, Phys.Lett. **B709** (2012) 322–340, arXiv:1111.0080 [hep-ex].

[21] ATLAS Collaboration Collaboration, G. Aad et al., *A study of the material in the ATLAS inner detector using secondary hadronic interactions*, JINST **7** (2012) P01013, arXiv:1110.6191 [hep-ex].

[22] ATLAS Collaboration Collaboration, G. Aad et al., *Searches for supersymmetry with the ATLAS detector using final states with two leptons and missing transverse momentum in sqrts = 7 TeV proton-proton collisions*, Phys.Lett. **B709** (2012) 137–157, arXiv:1110.6189 [hep-ex].

[23] ATLAS Collaboration Collaboration, G. Aad et al., *Measurement of the ZZ production cross section and limits on anomalous neutral triple gauge couplings in proton-proton collisions at sqrt(s) = 7 TeV with the ATLAS detector*, Phys.Rev.Lett. **108** (2012) 041804, arXiv:1110.5016 [hep-ex].

[24] ATLAS Collaboration Collaboration, G. Aad et al., *Electron performance measurements with the ATLAS detector using the 2010 LHC proton-proton collision data*, Eur.Phys.J. **C72** (2012) 1909, arXiv:1110.3174 [hep-ex].

[25] ATLAS Collaboration Collaboration, G. Aad et al., *Search for Massive Colored Scalars in Four-Jet Final States in sqrts=7 TeV proton-proton collisions with the ATLAS Detector*, Eur.Phys.J. **C71** (2011) 1828, arXiv:1110.2693 [hep-ex].

[26] Atlas Collaboration Collaboration, G. Aad et al., *Search for new phenomena in final states with large jet multiplicities and missing transverse momentum using sqrt(s)=7 TeV pp collisions with the ATLAS detector*, JHEP **1111** (2011) 099, arXiv:1110.2299 [hep-ex].

[27] Atlas Collaboration Collaboration, G. Aad et al., *Performance of the ATLAS Trigger System in 2010*, Eur.Phys.J. **C72** (2012) 1849, arXiv:1110.1530 [hep-ex].

[28] ATLAS Collaboration Collaboration, G. Aad et al., *Measurement of the inclusive and dijet cross-sections of b-jets in pp collisions at sqrt(s) = 7 TeV with the ATLAS detector*, Eur.Phys.J. **C71** (2011) 1846, arXiv:1109.6833 [hep-ex].

[29] ATLAS Collaboration Collaboration, G. Aad et al., *Search for supersymmetry in final states with jets, missing transverse momentum and one isolated lepton in sqrts = 7 TeV pp collisions using 1 fb^{-1} of ATLAS data*, Phys.Rev. **D85** (2012) 012006, arXiv:1109.6606 [hep-ex].

[30] ATLAS Collaboration Collaboration, G. Aad et al., *Search for squarks and gluinos using final states with jets and missing transverse momentum with the ATLAS detector in sqrt(s) = 7 TeV proton-proton collisions*, Phys.Lett. **B710** (2012) 67–85, arXiv:1109.6572 [hep-ex].

[31] ATLAS Collaboration Collaboration, G. Aad et al., *Search for the Standard Model Higgs boson in the decay channel $H \to ZZ(*) \to 4l$ with the ATLAS detector*, Phys.Lett. **B705** (2011) 435–451, arXiv:1109.5945 [hep-ex].

[32] ATLAS Collaboration Collaboration, G. Aad et al., *Measurement of the jet fragmentation function and transverse profile in proton-proton collisions at a center-of-mass energy of 7 TeV with the ATLAS detector*, Eur.Phys.J. **C71** (2011) 1795, arXiv:1109.5816 [hep-ex].

[33] ATLAS Collaboration Collaboration, G. Aad et al., *Search for New Phenomena in ttbar Events With Large Missing Transverse Momentum in Proton-Proton Collisions at sqrt(s) = 7 TeV with the ATLAS Detector*, Phys.Rev.Lett. **108** (2012) 041805, arXiv:1109.4725 [hep-ex].

[34] ATLAS Collaboration Collaboration, G. Aad et al., *Search for the Higgs boson in the $H \to WW \to l\nu jj$ decay channel in pp collisions at sqrts = 7 TeV with the ATLAS detector*, Phys.Rev.Lett. **107** (2011) 231801, arXiv:1109.3615 [hep-ex].

[35] ATLAS Collaboration Collaboration, G. Aad et al., *Search for a Standard Model Higgs boson in the $H \to ZZ \to l^+l^-\nu\nu^-$ decay channel with the ATLAS detector*, Phys.Rev.Lett. **107** (2011) 221802, arXiv:1109.3357 [hep-ex].

[36] ATLAS Collaboration Collaboration, G. Aad et al., *Search for displaced vertices arising from decays of new heavy particles in 7 TeV pp collisions at ATLAS*, Phys.Lett. **B707** (2012) 478–496, arXiv:1109.2242 [hep-ex].

[37] ATLAS Collaboration Collaboration, G. Aad et al., *Measurement of the cross-section for b-jets produced in association with a Z boson at sqrt(s)=7 TeV with the ATLAS detector*, Phys.Lett. **B706** (2012) 295–313, arXiv:1109.1403 [hep-ex].

[38] ATLAS Collaboration Collaboration, G. Aad et al., *Measurement of the cross section for the production of a W boson in association with b-jets in pp collisions at sqrt(s) = 7 TeV with the ATLAS detector*, Phys.Lett. **B707** (2012) 418–437, arXiv:1109.1470 [hep-ex].

[39] ATLAS Collaboration Collaboration, G. Aad et al., *Measurements of the electron and muon inclusive cross-sections in proton-proton collisions at sqrt(s) = 7 TeV with the ATLAS detector*, Phys.Lett. **B707** (2012) 438–458, arXiv:1109.0525 [hep-ex].

[40] ATLAS Collaboration Collaboration, G. Aad et al., *Measurement of the Transverse Momentum Distribution of W Bosons in pp Collisions at sqrt(s) = 7 TeV with the ATLAS Detector*, Phys.Rev. **D85** (2012) 012005, arXiv:1108.6308 [hep-ex].

[41] ATLAS Collaboration Collaboration, G. Aad et al., *Measurement of the centrality dependence of the charged particle pseudorapidity distribution in lead-lead collisions at*

$\sqrt{s_{NN}} = 2.76$ *TeV with the ATLAS detector*, Phys.Lett. **B710** (2012) 363–382, arXiv:1108.6027 [hep-ex].

[42] ATLAS Collaboration Collaboration, G. Aad et al., *Measurement of the pseudorapidity and transverse momentum dependence of the elliptic flow of charged particles in lead-lead collisions at* $\sqrt{s_{NN}} = 2.76$ *TeV with the ATLAS detector*, Phys.Lett. **B707** (2012) 330–348, arXiv:1108.6018 [hep-ex].

[43] ATLAS Collaboration Collaboration, G. Aad et al., *Performance of Missing Transverse Momentum Reconstruction in Proton-Proton Collisions at 7 TeV with ATLAS*, Eur.Phys.J. **C72** (2012) 1844, arXiv:1108.5602 [hep-ex].

[44] ATLAS Collaboration Collaboration, G. Aad et al., *Search for a heavy Standard Model Higgs boson in the channel* $H \to ZZ \to llqq$ *using the ATLAS detector*, Phys.Lett. **B707** (2012) 27–45, arXiv:1108.5064 [hep-ex].

[45] ATLAS Collaboration Collaboration, G. Aad et al., *A measurement of the ratio of the W and Z cross sections with exactly one associated jet in pp collisions at sqrt(s) = 7 TeV with ATLAS*, Phys.Lett. **B708** (2012) 221–240, arXiv:1108.4908 [hep-ex].

[46] ATLAS Collaboration Collaboration, G. Aad et al., *Measurement of the W to tau nu Cross Section in pp Collisions at sqrt(s) = 7 TeV with the ATLAS experiment*, Phys.Lett. **B706** (2012) 276–294, arXiv:1108.4101 [hep-ex].

[47] ATLAS Collaboration Collaboration, G. Aad et al., *Measurement of the top quark pair production cross section in pp collisions at sqrt(s) = 7 TeV in dilepton final states with ATLAS*, Phys.Lett. **B707** (2012) 459–477, arXiv:1108.3699 [hep-ex].

[48] ATLAS Collaboration Collaboration, G. Aad et al., *Measurement of the Z to tau tau Cross Section with the ATLAS Detector*, Phys.Rev. **D84** (2011) 112006, arXiv:1108.2016 [hep-ex].

[49] ATLAS Collaboration Collaboration, G. Aad et al., *Search for dilepton resonances in pp collisions at sqrt(s) = 7 TeV with the ATLAS detector*, Phys.Rev.Lett. **107** (2011) 272002, arXiv:1108.1582 [hep-ex].

[50] ATLAS Collaboration Collaboration, G. Aad et al., *Search for a heavy gauge boson decaying to a charged lepton and a neutrino in 1 fb-1 of pp collisions at sqrt(s) = 7 TeV using the ATLAS detector*, Phys.Lett. **B705** (2011) 28–46, arXiv:1108.1316 [hep-ex].

[51] ATLAS Collaboration Collaboration, G. Aad et al., *Inclusive search for same-sign dilepton signatures in pp collisions at sqrt(s) = 7 TeV with the ATLAS detector*, JHEP **1110** (2011) 107, arXiv:1108.0366 [hep-ex].

[52] ATLAS Collaboration Collaboration, G. Aad et al., *Measurement of the inclusive isolated prompt photon cross-section in pp collisions at sqrt(s)= 7 TeV using 35 pb-1 of ATLAS data*, Phys.Lett. **B706** (2011) 150–167, arXiv:1108.0253 [hep-ex].

[53] ATLAS Collaboration Collaboration, G. Aad et al., *Search for neutral MSSM Higgs bosons decaying to tau$^+$tau$^-$ pairs in proton-proton collisions at sqrt(s) = 7 TeV with the ATLAS detector*, Phys.Lett. **B705** (2011) 174–192, arXiv:1107.5003 [hep-ex].

[54] ATLAS Collaboration Collaboration, G. Aad et al., *Properties of jets measured from tracks in proton-proton collisions at center-of-mass energy sqrt(s) = 7 TeV with the ATLAS detector*, Phys.Rev. **D84** (2011) 054001, arXiv:1107.3311 [hep-ex].

[55] ATLAS Collaboration Collaboration, G. Aad et al., *Measurement of the transverse momentum distribution of Z/gamma* bosons in proton-proton collisions at sqrt(s)=7 TeV with the ATLAS detector*, Phys.Lett. **B705** (2011) 415–434, arXiv:1107.2381 [hep-ex].

[56] ATLAS Collaboration Collaboration, G. Aad et al., *Measurement of multi-jet cross sections in proton-proton collisions at a 7 TeV center-of-mass energy*, Eur.Phys.J. **C71** (2011) 1763, arXiv:1107.2092 [hep-ex].

[57] ATLAS Collaboration Collaboration, G. Aad et al., *Measurement of dijet production with a veto on additional central jet activity in pp collisions at sqrt(s)=7 TeV using the ATLAS detector*, JHEP **1109** (2011) 053, arXiv:1107.1641 [hep-ex].

[58] ATLAS Collaboration Collaboration, G. Aad et al., *Search for Diphoton Events with Large Missing Transverse Energy with 36 $pb^{-}1$ of 7 TeV Proton-Proton Collision Data with the ATLAS Detector*, Eur.Phys.J. **C71** (2011) 1744, arXiv:1107.0561 [hep-ex].

[59] ATLAS Collaboration Collaboration, G. Aad et al., *Measurement of the isolated di-photon cross-section in pp collisions at sqrt(s) = 7 TeV with the ATLAS detector*, Phys.Rev. **D85** (2012) 012003, arXiv:1107.0581 [hep-ex].

[60] ATLAS Collaboration Collaboration, G. Aad et al., *Measurement of the Upsilon(1S) Production Cross-Section in pp Collisions at sqrt(s) = 7 TeV in ATLAS*, Phys.Lett. **B705** (2011) 9–27, arXiv:1106.5325 [hep-ex].

[61] ATLAS Collaboration Collaboration, G. Aad et al., *Search for new phenomena with the monojet and missing transverse momentum signature using the ATLAS detector in sqrt(s) = 7 TeV proton-proton collisions*, Phys.Lett. **B705** (2011) 294–312, arXiv:1106.5327 [hep-ex].

[62] ATLAS Collaboration Collaboration, G. Aad et al., *Search for Heavy Long-Lived Charged Particles with the ATLAS detector in pp collisions at sqrt(s) = 7 TeV*, Phys.Lett. **B703** (2011) 428–446, arXiv:1106.4495 [hep-ex].

[63] ATLAS Collaboration Collaboration, G. Aad et al., *Limits on the production of the Standard Model Higgs Boson in pp collisions at sqrt(s) =7 TeV with the ATLAS detector*, Eur.Phys.J. **C71** (2011) 1728, arXiv:1106.2748 [hep-ex].

[64] ATLAS Collaboration Collaboration, G. Aad et al., *Measurement of Wgamma and Zgamma production in proton-proton collisions at sqrt(s)=7 TeV with the ATLAS Detector*, JHEP **1109** (2011) 072, arXiv:1106.1592 [hep-ex].

[65] ATLAS Collaboration Collaboration, G. Aad et al., *Measurement of the WW cross section in sqrt(s) = 7 TeV pp collisions with ATLAS*, Phys.Rev.Lett. **107** (2011) 041802, arXiv:1104.5225 [hep-ex].

[66] ATLAS Collaboration Collaboration, G. Aad et al., *Search for Contact Interactions in Dimuon Events from pp Collisions at sqrt(s) = 7 TeV with the ATLAS Detector*, Phys.Rev. **D84** (2011) 011101, arXiv:1104.4398 [hep-ex].

[67] ATLAS Collaboration Collaboration, G. Aad et al., *Search for pair production of first or second generation leptoquarks in proton-proton collisions at sqrt(s)=7 TeV using the ATLAS detector at the LHC*, Phys.Rev. **D83** (2011) 112006, arXiv:1104.4481 [hep-ex].

[68] ATLAS Collaboration Collaboration, G. Aad et al., *Measurement of the differential cross-sections of inclusive, prompt and non-prompt J/psi production in proton-proton collisions at sqrt(s) = 7 TeV*, Nucl.Phys. **B850** (2011) 387–444, arXiv:1104.3038 [hep-ex].

[69] ATLAS Collaboration Collaboration, G. Aad et al., *Measurement of the Inelastic Proton-Proton Cross-Section at $\sqrt{s} = 7$ TeV with the ATLAS Detector*, Nature Commun. **2** (2011) 463, arXiv:1104.0326 [hep-ex].

[70] ATLAS Collaboration Collaboration, G. Aad et al., *Search for an excess of events with an identical flavour lepton pair and significant missing transverse momentum in sqrts = 7 TeV proton-proton collisions with the ATLAS detector*, Eur.Phys.J. **C71** (2011) 1647, arXiv:1103.6208 [hep-ex].

[71] ATLAS Collaboration Collaboration, G. Aad et al., *Search for supersymmetric particles in events with lepton pairs and large missing transverse momentum in $\sqrt{s} = 7$ TeV proton-proton collisions with the ATLAS experiment*, Eur.Phys.J. **C71** (2011) 1682, arXiv:1103.6214 [hep-ex].

[72] ATLAS Collaboration Collaboration, G. Aad et al., *Search for high mass dilepton resonances in pp collisions at $\sqrt{s} = 7$ TeV with the ATLAS experiment*, Phys.Lett. **B700** (2011) 163–180, arXiv:1103.6218 [hep-ex].

[73] ATLAS Collaboration Collaboration, G. Aad et al., *Search for a heavy particle decaying into an electron and a muon with the ATLAS detector in $\sqrt{s} = 7$ TeV pp collisions at the LHC*, Phys.Rev.Lett. **106** (2011) 251801, arXiv:1103.5559 [hep-ex].

[74] ATLAS Collaboration Collaboration, G. Aad et al., *Search for supersymmetry in pp collisions at sqrts = 7TeV in final states with missing transverse momentum and b-jets*, Phys.Lett. **B701** (2011) 398–416, arXiv:1103.4344 [hep-ex].

[75] ATLAS Collaboration Collaboration, G. Aad et al., *Measurement of the Muon Charge Asymmetry from W Bosons Produced in pp Collisions at $\sqrt{s} = 7$ TeV with the ATLAS detector*, Phys.Lett. **B701** (2011) 31–49, arXiv:1103.2929 [hep-ex].

[76] ATLAS Collaboration Collaboration, G. Aad et al., *Search for stable hadronising squarks and gluinos with the ATLAS experiment at the LHC*, Phys.Lett. **B701** (2011) 1–19, arXiv:1103.1984 [hep-ex].

[77] ATLAS Collaboration Collaboration, G. Aad et al., *Measurements of underlying-event properties using neutral and charged particles in pp collisions at 900 GeV and 7 TeV with the ATLAS detector at the LHC*, Eur.Phys.J. **C71** (2011) 1636, arXiv:1103.1816 [hep-ex].

[78] ATLAS Collaboration Collaboration, G. Aad et al., *Search for high-mass states with one lepton plus missing transverse momentum in proton-proton collisions at* $\sqrt{s} = 7$ *TeV with the ATLAS detector*, Phys.Lett. **B701** (2011) 50–69, arXiv:1103.1391 [hep-ex].

[79] Atlas Collaboration Collaboration, G. Aad et al., *Search for squarks and gluinos using final states with jets and missing transverse momentum with the ATLAS detector in sqrt(s) = 7 TeV proton-proton collisions*, Phys.Lett. **B701** (2011) 186–203, arXiv:1102.5290 [hep-ex].

[80] ATLAS Collaboration Collaboration, G. Aad et al., *Measurement of Dijet Azimuthal Decorrelations in pp Collisions at sqrt(s)=7 TeV*, Phys.Rev.Lett. **106** (2011) 172002, arXiv:1102.2696 [hep-ex].

[81] Atlas Collaboration Collaboration, G. Aad et al., *Search for supersymmetry using final states with one lepton, jets, and missing transverse momentum with the ATLAS detector in sqrts = 7 TeV pp*, Phys.Rev.Lett. **106** (2011) 131802, arXiv:1102.2357 [hep-ex].

[82] ATLAS Collaboration Collaboration, G. Aad et al., *Search for Massive Long-lived Highly Ionising Particles with the ATLAS Detector at the LHC*, Phys.Lett. **B698** (2011) 353–370, arXiv:1102.0459 [hep-ex].

[83] ATLAS Collaboration Collaboration, G. Aad et al., *Luminosity Determination in pp Collisions at sqrt(s)=7 TeV Using the ATLAS Detector at the LHC*, Eur.Phys.J. **C71** (2011) 1630, arXiv:1101.2185 [hep-ex].

[84] Atlas Collaboration Collaboration, G. Aad et al., *Study of Jet Shapes in Inclusive Jet Production in pp Collisions at sqrt(s) = 7 TeV using the ATLAS Detector*, Phys.Rev. **D83** (2011) 052003, arXiv:1101.0070 [hep-ex].

[85] ATLAS Collaboration Collaboration, G. Aad et al., *Measurement of the production cross section for W-bosons in association with jets in pp collisions at sqrt(s) = 7 TeV with the ATLAS detector*, Phys.Lett. **B698** (2011) 325–345, arXiv:1012.5382 [hep-ex].

[86] Atlas Collaboration Collaboration, G. Aad et al., *Measurement of the centrality dependence of J/ψ yields and observation of Z production in lead-lead collisions with the ATLAS detector at the LHC*, Phys.Lett. **B697** (2011) 294–312, arXiv:1012.5419 [hep-ex].

[87] Atlas Collaboration Collaboration, G. Aad et al., *Measurement of the inclusive isolated prompt photon cross section in pp collisions at sqrt(s) = 7 TeV with the ATLAS detector*, Phys.Rev. **D83** (2011) 052005, arXiv:1012.4389 [hep-ex].

[88] ATLAS Collaboration Collaboration, G. Aad et al., *Charged-particle multiplicities in pp interactions measured with the ATLAS detector at the LHC*, New J.Phys. **13** (2011) 053033, arXiv:1012.5104 [hep-ex].

[89] ATLAS Collaboration Collaboration, G. Aad et al., *Search for Diphoton Events with Large Missing Transverse Energy in 7 TeV Proton-Proton Collisions with the ATLAS Detector*, Phys.Rev.Lett. **106** (2011) 121803, arXiv:1012.4272 [hep-ex].

[90] Atlas Collaboration Collaboration, G. Aad et al., *Measurement of the top quark-pair production cross section with ATLAS in pp collisions at* $\sqrt{s} = 7$ *TeV*, Eur.Phys.J. **C71** (2011) 1577, arXiv:1012.1792 [hep-ex].

[91] Atlas Collaboration Collaboration, G. Aad et al., *Measurement of underlying event characteristics using charged particles in pp collisions at* $\sqrt{s} = 900 GeV$ *and 7 TeV with the ATLAS detector*, Phys.Rev. **D83** (2011) 112001, arXiv:1012.0791 [hep-ex].

[92] Atlas Collaboration Collaboration, G. Aad et al., *Observation of a Centrality-Dependent Dijet Asymmetry in Lead-Lead Collisions at sqrt(S(NN))= 2.76 TeV with the ATLAS Detector at the LHC*, Phys.Rev.Lett. **105** (2010) 252303, arXiv:1011.6182 [hep-ex].

[93] The ATLAS Collaboration Collaboration, G. Aad et al., *Studies of the performance of the ATLAS detector using cosmic-ray muons*, Eur.Phys.J. **C71** (2011) 1593, arXiv:1011.6665 [physics.ins-det].

[94] Atlas Collaboration Collaboration, G. Aad et al., *Measurement of the* $W \rightarrow l\nu$ *and* $Z/\gamma* \rightarrow ll$ *production cross sections in proton-proton collisions at sqrt(s) = 7 TeV with the ATLAS detector*, JHEP **1012** (2010) 060, arXiv:1010.2130 [hep-ex].

[95] ATLAS Collaboration Collaboration, G. Aad et al., *Search for Quark Contact Interactions in Dijet Angular Distributions in pp Collisions at sqrt(s) = 7 TeV Measured with the ATLAS Detector*, Phys.Lett. **B694** (2011) 327–345, arXiv:1009.5069 [hep-ex].

[96] ATLAS Collaboration Collaboration, G. Aad et al., *Readiness of the ATLAS Tile Calorimeter for LHC collisions*, Eur.Phys.J. **C70** (2010) 1193–1236, arXiv:1007.5423 [physics.ins-det].

[97] ATLAS Collaboration Collaboration, G. Aad et al., *Commissioning of the ATLAS Muon Spectrometer with Cosmic Rays*, Eur.Phys.J. **C70** (2010) 875–916, `arXiv:1006.4384 [physics.ins-det]`.

[98] Atlas Collaboration Collaboration, G. Aad et al., *Performance of the ATLAS Detector using First Collision Data*, JHEP **1009** (2010) 056, `arXiv:1005.5254 [hep-ex]`.

[99] ATLAS Collaboration Collaboration, G. Aad et al., *Charged-particle multiplicities in pp interactions at sqrt(s) = 900 GeV measured with the ATLAS detector at the LHC*, Phys.Lett. **B688** (2010) 21–42, `arXiv:1003.3124 [hep-ex]`.